BASIC THEORY
OF PHOTOACOUSTIC SPECTROSCOPY FOR LIQUIDS
AND ITS APPLICATION
TO ANALYTICAL CHEMISTRY AND SPECTROSCOPY

by

Takehiko KITAMORI

January 1989

ABSTRACT

The basic theory of photoacoustic spectroscopy (PAS) for the liquid phase was established. The photoacoustic (PA) effect was described with a generalized linear transform equation and wave equation of thermally forced motion which represented the energy conversion process from optical energy to thermal energy and acoustic signal generation and propagation, respectively. This coupling equation was solved using linear response theory and Green's functions. The properties of the PA signal and the characteristics of PAS such as sensitivity were clarified by the theory. The basic theory was applied to development of various analytical chemical and spectroscopic applications. An optimization method for PAS instrumentation including an ultrasensitive PA cell design method was developed theoretically, and an ultrasensitive PAS system in which the lower detection limit absorption coefficient reached to 10^{-8} cm^{-1} was realized. The theory of ultratrace PA determination was developed, and in its experimental verification, determination of sub-ppt amounts of cobalt was demonstrated. Using the phase shift of the PA signal, a unique sizing and thermal characterization method of turbid particles such as measurement of the heat transfer coefficient were proposed on the basis of the general theory, as well as the ultratrace determination. The proposed method was proved using polystyrene turbid solutions experimentally. As a further development of the theoretical and experimental methodology, novel methods for ultrasensitive PA immunoassay in which the determination limit was at least two to three orders lower than conventional methods, and a counting method of ultrafine particles in liquids using laser breakdown acoustic effect, which could count particles smaller than 0.1 μm, were proposed and demonstrated experimentally, and a characterization method for nonradiative relaxation phenomena was theoretically examined.

SYMBOLS, NOMENCLATURE AND ABBREVIATIONS

$A_m(a, f)$	:	Frequency characteristics of PA signal defined by Eq. (2.35)
a	:	Cell radius
$\arg\{x\}$	:	Argument of x
α	:	Absorption coefficient
α_b	:	Absorption coefficient of solvent
β	:	Isothermal bulk modulus
C	:	Weight concentration
C_{det}	:	Lower determination limit concentration
C_e	:	Count expectation of breakdown acoustic pulse
C_m	:	Molar concentration
C_p	:	Specific heat
Ξ	:	Linear transformation operator
ξ	:	Energy conversion ratio defined by Eq. (2.32)
D_{op}	:	Beam diameter
D_{th}	:	Thermal diffusion coefficient
$D(t)$	:	Impulse response of the thermal process
$D^f(\omega_0)$	:	Transfer function defined as Fourier image of $D(t)$
$D^f_{total}(\omega_0)$	:	Total transfer function of nonradiative relaxation system
$D^f_j(\omega_0)$	:	Transfer function of j-th nonradiative relaxation process
$D^f_{ij}(\omega_0)$	:	Transfer function of j-th nonradiative relaxation process of i-th component
d	:	Particle radius (in Chapter V)

		Particle diameter (in Chapters VI and VII)
$\delta(t)$	:	δ-Function
E_b	:	Electric field intensity in beam waist
$\mathrm{Erf}(x)$	:	Error function
ε	:	Relative dielectric constant
ε_m	:	Molar absoptivity
ε_n	:	Neumann factor
F	:	Focal length
F_p	:	Total shot number of excitation beam pulse
f	:	Modulation frequency
f_p	:	Pulse repetition number
$f_{0,j}$	:	Modulation frequency at j-th phase zero point
ϕ	:	Phase of photoacoustic signal
ϕ_D	:	Phase of photoacoustic signal due to thermal process
ϕ_Q	:	Phase of photoacoustic signal due to acoustic process
$G_w(\mathbf{r}\|\mathbf{r}')$	:	Propagator (Green's function)
g	:	g-Value of piezoelectric constant
Γ	:	Ratio of quantum yield defined by Eq. (8.17)
γ	:	Beam expansion coefficient due to thermal lens effect defined by Eq. (3.7)
$H(\mathbf{r}, t)$	:	Heat distribution
$H_{total}(\mathbf{r}, t)$	:	Distribution of total heat quantity released from microparticles
$\mathrm{H}^{(1)}_m(x)$	:	m-th Order Hankel function of the first kind
$\mathrm{Hev}(x)$	:	Heaviside function
h	:	Heat transfer coefficient

$\eta=\beta/C_p$	:	Thermal expansion coefficient defined by Eq. (2.9)
η_c	:	Count efficiency defined by Eq. (7.4)
η_N	:	Quantum yield of nonradiative relaxation process
$\eta_{N,j}$	:	Quantum yield of j-th nonradiative relaxation process
$\eta_{N,ij}$	:	Quantum yield of j-th nonradiative relaxation process of i-th component
$I(\mathbf{r}, t)$	:	Distribution of excitation beam
$\triangle I$	:	Absorbed optical energy
I_0	:	Peak intensity of the excitation beam
$\mathrm{I}_j(x)$	:	j-th Order modified Bessel function
$\mathrm{Im}\{x\}$	:	Imaginary part of x
J	:	Heat flux (in Chapter V) or Optical energy of excitation beam pulse (in Chapter VII)
$\mathrm{J}_m(x)$	:	m-th Order Bessel function
$K_j(x)$	:	j-th Order modified Hankel function
k	:	Normalizing factor, where k/f means the number of pulses and is non-dimensional
κ	:	Thermal conductivity
κ_e	:	Modulus of elasticity
L	:	Cell length
l_s	:	Sample length
λ	:	Wavelength
λ_j	:	Decay constant of j-th excited state
λ_{jk}	:	Eigenvalue of structual natural frequency f_{jk}, where subscripts j and k are the number of the

		circumferential wave and the number of the longitudinal half-wave in the mode shape, respectively
M_j^f	:	j-th Fourier coefficient
$M(t)$	:	Intensity modulation function
N	:	Number density of particles
N_j	:	Population of j-th excited state
N_s	:	Sampling time of boxcar integration
$N(t)$	:	Noise
n_e	:	Expectation of particle number in beam waist
$<P>$	:	Photoacoustic signal magnitude
$P(\mathbf{r}, t)$	:	Photoacoustic signal
$Q^f(\mathbf{r}, \omega)$	:	Propagation function defined by Eq. (2.6)
$q_n^f(\mathbf{r}, \omega)$	:	n-th Fourier component of $Q^f(\mathbf{r}, \omega)$
θ	:	Phase of lock-in amplifier
$R(\mathbf{r})$	:	Spatial distribution of the excitation beam
$\mathrm{Re}\{x\}$	:	Real part of x
$R_p(a)$	:	Magnitude distribution of photoacoustic signal defined by Eq. (2.34)
$R_s(\mathbf{r})$	:	Spatial response of the piezoelectric transducer
r_0	:	Beam radius
r_b	:	Spot size of beam waist
$ref(t)$	:	Reference signal
ρ_m	:	Mass density
S, $S(\mathbf{r})$, $S(\tau)$	:	Photoacoustic signal magnitude
$\mathbf{S}$	:	Surface area of particle
S_b	:	Blank or background signal magnitude

S_L	:	In-phase signal magnitude of lock-in amplifier
$S_r(t)$	:	Recovered photoacoustic signal
$S(\mathbf{r}, t)$	:	Detected photoacoustic signal
$\&(\mathbf{r})$	:	Normalized signal distribution function defined by Eq. (3.11)
σ	:	Standard deviation
σ_m	:	Mass density
σ_p	:	Poisson's ratio
T	:	Ambient temperature
$T(\rho, t)$	:	Temperature field
τ	:	Time delay
$\tau_D = \sigma_s C_{ps} V/Sh$	:	Heat release time from a microparticle
τ_f	:	Modulation period
τ_N	:	Nonradiative relaxation time
τ_p	:	Pulse dulation
$\tau_{p,j}$	:	Time giving the peak of decay curve of j-th excited state
$\triangle\tau_{p,j}$	:	Full width of half maximum of Lorentzian
$\mathbf{V}$	:	Internal domain of a particle
V_{op}	:	Volume of beam waist
v	:	Sound velocity
ω_J	:	Power density of excitation beam pulse
ω_0	:	Modulation angular frequency
$\omega_{0,j}$	:	Modulation angular frequency at j-th phase zero point
ζ	:	Ratio between excitation beam radius and cell radius

$[x]$	:	Gaussion notation representing the maximum integer less than x
Superscript f	:	Fourier image
Subscript s	:	Material constant of particles
AO	:	Acousto-optic
CW	:	Continuous wave
CW PAS	:	Continuous wave excitation PAS
PA	:	Photoacoustic
PAS	:	Photoacoustic spectroscopy
PAM	:	Photoacoustic microscopy
PIA	:	Photoacoustic immunoassay
RF	:	Rheumatoid factor
SEM	:	Scanning electron microscope
S/N	:	Signal to noise ratio

TABLE OF CONTENTS

CHAPTER I INTRODUCTION

1.1 Historical Background

The heat induced by nonradiative atomic and molecular relaxation processes causes thermal expansion of a sample medium. When the sample excitation is intermittent, the periodic thermal expansion of the medium emits an acoustic or thermoelastic wave which can be measured by photoacoustic spectroscopy (PAS). As the proportionality of signal magnitude to the absorption coefficient is one of the most fundamental characteristics of PAS, PAS has been applied to various fields, including spectrochemistry, solid state physics, chemical physics, and analytical chemistry, as a quite sensitive spectroscopic tool.

The principle of PAS, i.e. the photoacoustic (PA) effect, was found in 1880 by Alexander Graham Bell, the inventor of the telephone (Bell, 1880). He discovered acoustic signals were generated in a closed vessel when it was irradiated by chopped solar rays. His samples were solid materials, and a relation between the signal magnitude and absorption coefficient was becoming apparent. Tyndall (1881) and Röntgen (1881) also found PA effects in gas samples. However, the PA signals detected in these experiments were weak and obscure, and no spectroscopical or analytical applications of the effect were shown.

About sixty years after these first discoveries, Viengerov (1938) applied the PA effect to measure gaseous concentration using the proportionality of signal magnitude to sample absorbancy. The gas analyzers using this method were called "spectrophones", and they became a popular analysis tool. Luft (1943) developed a differential type spectrophone, and it became the basis for current non-dispersive

differential infrared gas analyzers. Development of the spectrophones was deeply indebted to the progress of microphones which served as the PA signal detectors.

Until 1970, the PA effect was only utilized in gas analysis by spectrophones. However, after that rapid progress was made owing to the advanced electronics for sensitive microphones, signal recovering methods such as lock-in amplification, and high intensity light sources such as xenon lamps. In particular, the adaptation of lasers as powerful excitation beam sources gave the spectrophones ultrasensitivity. Aoki et al. (1970) applied a spectrophone to detect weak emissions of a CO_2 laser. However, they used the PA effect to detect only optical radiation, but not to detect trace gases or to obtain weak absorption spectra. In 1971, Kreuzer (1971) showed theoretically that a laser made a spectrophone 10^4 times more sensitive, and he demonstrated the determination of trace hydrocarbon gases on the ppb order, by using an He-Ne laser operating at the 3.39 μm lasing line. On the other hand, Harshbarger and Robin (1973), and Rosencwaig (1973a) tried to use the PA effect for spectroscopical measurement of solid samples. They showed that their method could obtain the absorption spectrum from various forms of solid samples, such as bulk, powder and biological samples, notwithstanding that the materials were optically transparent or opaque. From these pioneering works, the spectrophone was reborn as "optacoustic spectroscopy", which was applied to various fields of science and engineering (Pao, 1977). Rosencwaig proposed a second change in the name, "photoacoustic spectroscopy", to avoid confusing the "optacoustic effect" and the "acousto-optic effect". The name "photoacoustic spectroscopy" (PAS) has now been accepted worldwide. Thus, the basis for the present ultrasensitive and multi-functional PAS was laid.

For gas phase samples, PAS was mainly applied to trace analyses and measurement of weak absorption spectra. Kreuzer et al. (1972) and Patel (1978) detected trace air pollutants, such as NOx, on ppb order. Cox (1978) obtained weak absorption spectra based on a multi-photon absorption process of SF_6-Ar gas mixtures. Marinero et al. (1979) used PAS as a detector in doppler free laser spectroscopy, and they obtained a weak doppler free spectrum of iodine. The residual phonons after Raman scattering, which is inelastic light scattering, are changed into heat, and generate a PA signal. Barret et al. (1979) measured PA signals originating in stimulated Raman scattering, and clearly obtained the rotational spectrum of CO_2.

On the other hand, the theory of PAS in the gas phase was mainly developed by Kreuzer (1971). He described a PA signal as an acoustic wave in a cavity using a wave equation in which the source term was the elastic thermal expansion of the gas medium. The basic properties of PA signal in gas, such as frequency characteristies, were discussed, and cell characteristics were also described. Even a design method for cells using resonant conditions was briefly commented in the report. The methodological and theoretical studies of PAS in the gas phase were, thus, established rather early in the history of PAS studies, during the 1970's.

Rosencwaig was substantially the first to show that PAS was an effective and multi-functional method to obtain spectroscopical and analytical information from solid samples. He enclosed solid samples in a closed PA cell which was connected with a microphone through a coupling gas, and obtained PA spectra of various materials using a xenon lamp as an excitation beam source (Rosencwaig, 1973a). The absorption spectra of powders, biological materials, bulk and optically opaque samples were clearly presented (Rosencwaig, 1973b, 1975a, 1975b, 1977), though

absorption spectra of most of these samples could not be easily obtained by conventional spectroscopical methods.

After these studies, PAS was applied in various fields. For example, measurements of reactivity on catalytic materials (Low et al., 1978) and electrodes (Matsuda et al., 1980), determination of energy gaps in semiconductors (Wasa et al., 1980), tracing electron migrations in photosynthesis (Cahen et al., 1978), and detection of vague spots in monolayer levels for thin layer chromatgraphy (Rosencwaig and Hall, 1975), were reported. From among the many interesting, and sometimes unique applications which have been shown, a number of review articles have been written (Pao, 1977; Rosencwaig, 1980a; Sawada, 1982). In particular, the development of microscopy using PAS has been one of the most important applications. Wong et al. (1978) showed that the microscopic image of a solid surface and sub-surface could be obtained by measuring the PA signal by scanning the beam irradiated spot on the observed region. As the source of the PA signal originates in the variation of the heat generated in the beam irradiated region, the signal source can be beneath the surface, because heat diffuses three-dimensionally in the sample. Hence photoacoustic microscopy (PAM) can image sub-surface materials and defects (Sawada et al., 1981). Further, PAM can obtain not only an optical image, but also an image based on thermal properties such as heat conductivity, thermal bulk modulus, and specific heat (Rosencwaig, 1980b). Cargill (1980) produced microscopic imagings of the distributions of Al alloy in an invar rod based on the difference in thermal bulk modulus between the Al alloy and invar, by using an electron beam and piezoelectric transducer instead of an optical beam and microphone.

With these interesting applications as background, basic research on methodological and theoretical aspect of solid PAS has been steadily

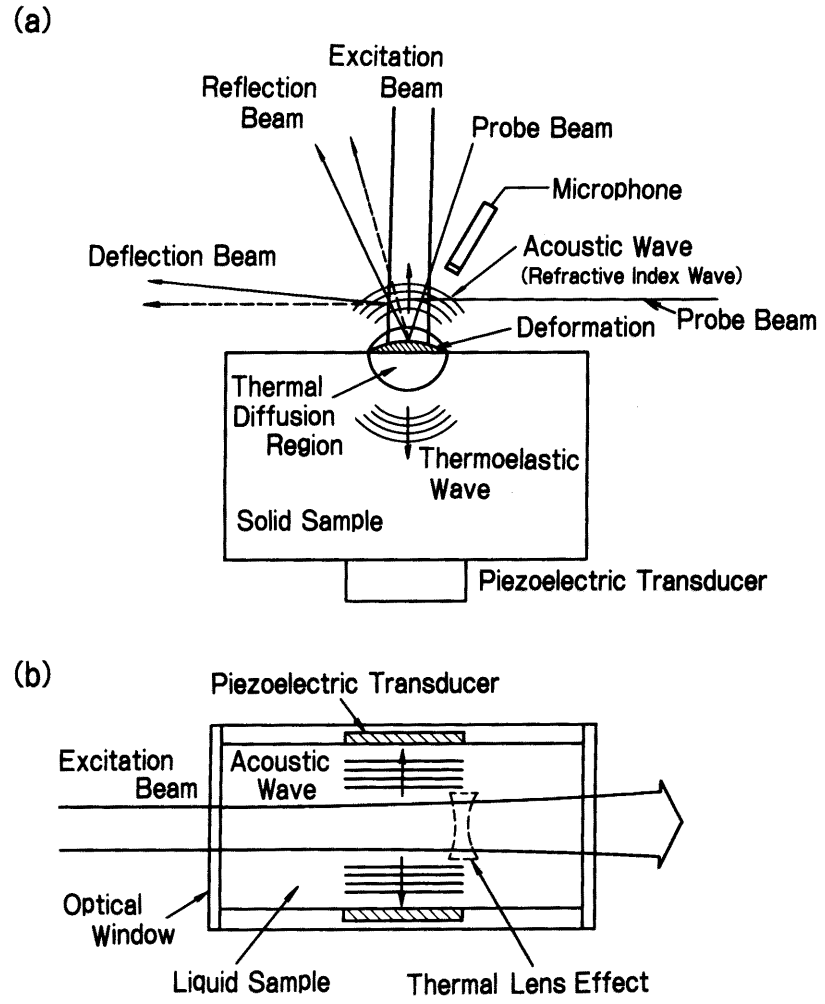

Fig. 1.1 Photoacoustic effect (a) in/on solid and (b) liquid.

advancing. Several different detection methods of the PA effect were proposed. As shown in Fig. 1.1(a), variation of the temperature field around the beam irradiated region generates not only acoustic and thermal waves in the coupling gas, but also an thermoelastic wave in the sample, a refractive index wave which accompanies the acoustic wave in the coupling gas, and surface deformation. In the drawing a microphone is used to detect the acoustic wave in the coupling gas, and a piezoelectric transducer such as PZT detects the thermoelastic wave propagating in the solid sample.

Fournier et al.(1980) proposed an optical beam deflection method to detect the refractive index wave. In this method, a probe laser beam, which passes horizontally through the neighborhood of the excitation beam-irradiated surface, was deflected due to the diffraction by the refractive index wave, and the PA effect is measured by the deflection angle (Fournier et al., 1980; Boccara et al., 1980). The surface deformation also deflects the reflected probe beam on the irradiated spot, and this deflection angle is also measured to detect the PA effect (Opsal et al., 1983). With the proposals of these detection methods, their theoretical basis in solid has been developed. Rosencwaig and Gersho (1976) first showed that the PA signal in a coupling gas could be described by the adiabatic expansion of the gas due to the thermal wave generated on the beam-irradiated region. This so called RG theory clarified the dependence of the signal on the absorption coefficient and thermal properties of the solid, thereby giving the theoretical foundation to PAS using a gas-microphone cell. Later, the PA signal in the gas-microphone cell was analyzed more rigorously using coupling equations of thermal and wave equations (McDonald and Wetsel, 1978). These theories well explained PAS characteristics in gas-microphone cells.

Jackson and Amer (1980) introduced the theory of piezoelectric PAS which detected the thermoelastic wave in solid samples. They treated the samples as an elastic layer, and solved quasistatic thermoelastic equations. This theory was effective for the cases in which the dominant factor in signal generation was a bending motion caused by the thermal stress induced by optical irradiation. For the beam deflection methods, Jackson et al. (1981) and Murphy and Aamodt (1980) explained the probe beam deflection by analyzing the temperature field just above the excitation beam-irradiated spot.

As described above, PAS has been developed and studied primarily for gas and solid samples. There has been a delay in the application of PAS to liquid phase samples. One of the principal reasons was that the gas coupled microphone cell was unsuited to liquid samples. As shown by McDonald and Wetzel (1978), when gas coupled microphone cells were applied to optically transparent samples, the detected PA signals could be dominated by thermoelastic vibrations of the samples themselves rather than the ordinary PA signal caused by time variation of the temperature field in the coupling gas. In one case, these authors found that, the magnitude of the thermoelastic wave in the liquid was twice that of the PA signals which was predicted by the RG theory, for an absorption coefficient of $\alpha = 10^{-1}$ cm^{-1} and modulation frequency of 200 Hz. However, gas coupled microphone cells were unsuitable for detection of the thermoelastic wave, because the coupling gas between the liquid sample and the microphone caused an impedance mismatch resulting in signal attenuation of 10^{-5} (McDonald and Wetzel, 1978). As volatile organic solvents were used, additional prolems included, corrosion of the microphone, deteriorating its performance, and solvent loss, causing concentration changes.

Consequently, a more efficient direct coupling method was developed to measure the thermoelastic vibration or waves generated in liquid samples, in which the piezoelectric transducer was in direct contact with the sample as shown in Fig. 1.1(b). In this case, signal attenuation caused by acoustic mismatching of the coupling gas is eliminated, making the direct coupling method quite sensitive to the absorption coefficient. Lahman et al. (1977) and Oda et al. (1978) demonstrated that using PAS, trace determinations could be achieved which were about two orders more sensitive than conventional colorimetric analysis. These works found a lower determination limit at ppt (parts per trillion) levels for β-carotene in

chloroform and Cd as Cd-dithizonate chelate, also in the same solvent, respectively. Voigtman et al. (1981) also obtained similar results for porphyrin derivatives. Weak absorption spectra, such as spectra of optical transparent samples and of forbidden transitions, could be obtained with PAS. Absorption spectrum of water in the visible region was obtained by Patel and Tam (1979). The absorption coefficient of the measured spectral region was on the order of 10^{-3} - 10^{-5} cm^{-1}. Sawada et al. (1979) saw fine structures of the Nd^{3+} ion in aqueous solutions in the spectral regions from 560 to 600 nm and from 610 to 650 nm. They clarified that these fine structures were from forbidden f-f transitions. The less sensitive absorption spectrophotometer did not observe these features.

Although the ultrasensitivity of liquid PAS with the direct coupling method has been shown in various experimental reports, basic studies on methodological and theoretical aspects have not been well developed. Methodologically, two categories of signal excitation have been reported, continuous wave (CW) excitation in which the intensity of the CW laser beam is modulated sinusoidally or rectangularly, and pulsed excitation which uses a pulse laser beam as excitation source. The theories have also been developed mainly along these two lines. Kohanzadeh et al. (1975), Atalar (1980), Kitamori and Sawada (1982), and Liu (1982) have independently proposed analytical models for CW excitation. Kohanzadeh et al. (1975) described the thermoelastic properties of a liquid by using a wave equation, and obtained a numerical solution for a cylindrical cell giving rigorous boundary conditions. However, as their model was analyzed numerically, little general description of PA signals as a function of parameters was given. In the analytical models of Kitamori and Sawada, and Liu, the integral representations of the solutions of the wave equations using Green's function described more general properties of PA signals such

as frequency characteristics. On the other hand, Patel and Tam (1981) and later Tam alone (1985) reviewed the theoretical treatment of acoustic signal generation in liquids as related to pulsed PA signal excitation.

However, these theoretical treatments were lacking in comparison with the more developed work for gas and solid phase samples, since the former treated only acoustic properties related to signal propagation (e.g. frequency characteristics of PA signals), and little spectroscopical, analytical or chemical information could be obtained from them. For example, no physical meaning of the phase was given, which considered the process of PA signal generation as having multistage energy conversion processes: i.e. optical energy of excitation beam is converted to thermal energy by a nonradiative relaxation process; thermal energy is converted to mechanical energy of the PA signal by vibrational themal expansion of the medium; and mechanical energy is converted to electrical energy by a piezoelectric effect of the detector. As well as this lack of physical meanings of the phase, these have proposed no applications, except as an ultrasensitive weak absorption detector. Even in applications as a weak absorption detector, an optimization method for measurement conditions, such as cell geometries, has not been given. In addition, the relationship between the PA signal magnitude and the absorption coefficient of the sample in which the above complicated energy conversions are taken into consideration is not clear.

As outlined above, PAS for liquid samples is still at an early stage of study in comparison with PAS for gas and solid samples, although its remarkable and promising ultrasensitivity has been demonstrated.

1.2 Objectives

In recent years, water and reagents used in technical fields, such as semiconductor, biochemical, and nuclear engineering fields, are highly purified, with some kinds of impurities demanding ppt (pg/mL) to sub-ppt level analyses. For this reason, ultrasensitive analytical methods which have a generality to various chemical species are required, not only for quality control of water and solvents, but for carrying out the basic research in these fields. Conventional ultrasensitive analytical methods, such as laser induced fluorometry, have not satisfied the above requirement from the viewpoint of sufficient generality for chemical species, though they have demonstrated some ppt levels determination (Voightman and Winefordner, 1982; Yamada et al., 1984). On the other hand, PAS is one of the most sensitive analytical methods, and it is expected to be a good general method as well, because nonradiative relaxation processes have a large quantum yield for almost all chemical species.

However as mentioned in the previous section on historical background, the methodology and theory of PAS for liquid samples has not been established, and its applications have not been well developed either, although its potentiality for ultratrace determinations has been shown experimentally. Then, the first objective of this study is to establish the theory of PAS for liquids, and to give a theoretical basis to the methodology for analytical chemistry and spectroscopic applications. Secondly, on the basis of the theory, instrumentation for ultrasensitive PAS and its application to sub-ppt levels ultratrace determination are developed. Subsequently, novel applications of PAS for characterization of microparticles in liquids, detection of ultrafine particles in liquids, immunological analysis, and evaluation of nonradiative relaxation time are proposed on the basis of the general theory, and these applications are

verified or demonstrated experimentally. Finally, future developments of PAS are discussed on the basis of the knowledge obtained.

CHAPTER II BASIC THEORY

As briefly mentioned in the first chapter, a theory of PAS for the liquid phase has not been established, nor have the physical properties of PA signals been clarified, although the potential possibility of ultrasensitive measurements has been shown experimentally. Then, in this chapter, the PA signal in liquids is analyzed theoretically, along with its properties and those of PAS.

First, an analytical model of a PA signal in liquids is proposed on the basis of energy conversion and migration from optical energy of the excitation beam to acoustic energy of the PA signal, and the PA signal is described with a coupling equation of a wave equation of forced motion and a generalized linear transformation equation (Kitamori et al., 1985c). A general solution of the PA signal is obtained using the method of Green's function and linear response theory. From the general solution, the relationship between the PA signal and energy conversion and migration processes from optical energy to thermal energy due to such processes as nonradiative relaxation, thermal diffusion, photochemical reaction, etc., is clarified. Propagation characteristics of the acoustic wave are also described. This general solution is applied to the development of various applications of PAS in the later chapters.

In the next step, a detection theory of the PA signal, including signal recovery from noise field, is developed based on the general solution (Kitamori and Sawada, 1988). The characteristics of the signal excitation and detection using CW, pulse and correlation methods are discussed using the detection theory. The detection theory is used to optimize the PAS system in the next chapter. Further, the physical

meanings of the PA signal detected with CW PAS, which is mainly used in the applications of later chapters, are clarified.

Finally, the theory developed in this chapter is verified from measurement of the frequency characteristics of PA signals (Kitamori et al., 1984).

2.1 General Description of PA Effect

A PA signal is induced by thermoelastic vibration of the sample, which originates in the periodical heat generation caused by intermittent optical excitation and relaxation. In the present theory, PA signal generation is phenomenologically classified into two processes as shown in Fig. 2.1. The first process is microscopic energy conversion and migration from optical energy to thermal energy. This microscopic energy conversion is achieved mainly through optical excitation and nonradiative relaxation. Other energy conversion processes such as a photochemical reaction, photosynthesis, and phase transition are also able to provide thermal energy to the source term of the PA signal. The generated thermal energy macroscopically migrates in the medium by thermal diffusion, leading to formation of a heat distribution. This process, in which the optical energy is converted into thermal energy and the heat distribution is formed, is named as the thermal process herein.

When the excitation beam irradiation is intermittent, the heat distribution fluctuates periodically. This fluctuation causes a fluctuation of the temperature field in the medium, accompanied by a periodical thermal expansion of the medium. In turn this periodical thermal expansion causes the acoustic or thermoelastic wave, that is the PA signal. This second process, in which the PA signal is generated by

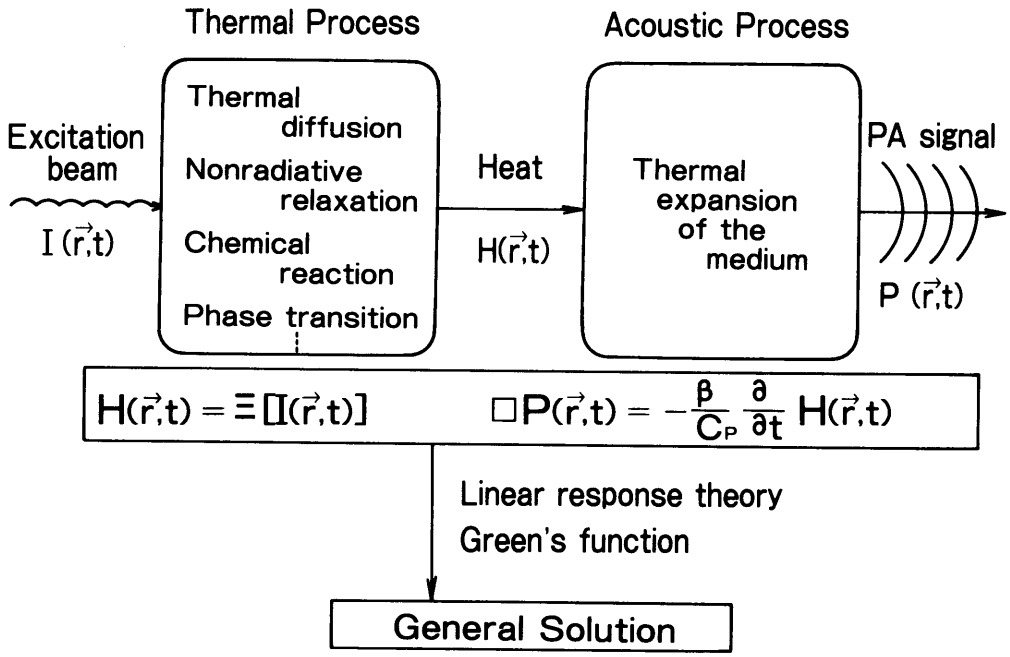

Fig. 2.1 Analytical model of PA signal in liquids.

the fluctuation of the heat distribution, is named as the acoustic process.

Mathematically, conversion from the excitation beam $I(\mathbf{r}, t)$ to heat distribution $H(\mathbf{r}, t)$ in the thermal process is described with a generallized linear transformation operator Ξ as follows,

$$H(\mathbf{r}, t) = \Xi(I(\mathbf{r}, t)). \tag{2.1}$$

In Eq. (2.1), the linearity of the operator Ξ is postulated on time t and space $\mathbf{r}$, but not on the optical properties of the samples. On the other hand, the PA signal $P(\mathbf{r}, t)$ generated in the acoustic process is described

by the following wave equation for which the source term is the fluctuation of the heat distribution,

$$(\nabla^2 - \frac{1}{v^2}\frac{\partial^2}{\partial t^2}) P(\mathbf{r}, t) = -\frac{\beta}{C_p}\frac{\partial}{\partial t} H(\mathbf{r}, t) \qquad (2.2)$$

where v is the sound velocity; C_p, the specific heat; and β, the isothermal bulk modulus. The effect of the interaction between both processes is obtained from coupling between Eqs. (2.1) and (2.2). Thus, a general description of the PA signal $P(\mathbf{r}, t)$ is obtained.

In most conventional theories of PAS for solid and liquid phase samples, the thermal process is described using only thermal diffusion equations (e.g., McDonald and Wetsel, 1978; Kohanzadeh et al., 1975). In these theories, the other effects of energy migration, such as microscopic energy migration in nonradiative relaxation, cannot be included exactly. Furthermore, as is mentioned later, thermal diffusion is not the dominant factor in determining the heat distribution in liquid samples, because the thermal diffusion length in liquids is somewhat shorter than that in solids. Therefore, the general description of the thermal process, using the linear operator, is appropriate. In addition, this analytical model is useful to obtain spectroscopical and analytical information, because the microsopic energy conversion and migration in the thermal process is taken in account with the generalized form.

2.2 General Solution

The general solution of the coupling equations (2.1) and (2.2) is obtained using linear response theory and Green's function as shown in

Fig. 2.1 (Kitamori et al., 1985c). First, linear response theory is introduced to analyze the thermal process. Generally, the transformation from $I(\mathbf{r}, t)$ to $H(\mathbf{r}, t)$ in the linear system is described by the following integral expression,

$$H(\mathbf{r}, t) = \Xi(I(\mathbf{r}, t))$$

$$= \int D(\tau) I(\mathbf{r}, t-\tau)\, d\tau, \qquad (2.3)$$

where $D(t)$ is the impulse response of the system. Physically, $D(t)$ is interpreted as the heat distribution for the impulse input of excitation energy.

The intensity of the excitation beam which is modulated in various ways, or the pulsed beam is used as an excitation source in PAS. In either case, the modulation is performed in the time domain, and the spatial distribution of optical energy is not varied time dependently. Hence the distribution of the excitation beam $I(\mathbf{r}, t)$ is represented as

$$I(\mathbf{r}, t) = M(t) R(\mathbf{r}), \qquad (2.4)$$

where $M(t)$ and $R(\mathbf{r})$ are the intensity modulation function and the spatial distribution of the excitation beam in the medium, respectively.

As is discussed later, the thermal diffusion length of the medium is less than 10^0 - 10^1 μm for beam modulation frequencies above 10^1 Hz, and considering that modulation frequencies of less than 10^1 Hz are seldom applied in liquid PAS, the thermal diffusion length is negligibly shorter than the domain of $R(\mathbf{r})$. Therefore, the heat distribution is obtained from Eqs. (2.3) and (2.4), and is

$$H(\mathbf{r}, t) = R(\mathbf{r}) \int D(\tau) M(t-\tau)\, d\tau. \tag{2.5}$$

Secondly, the solution of the wave equation Eq. (2.2) is given with an appropriate propagator $G_\omega(\mathbf{r} \mid \mathbf{r}')$,

$$P^f(\mathbf{r}, \omega) = -\frac{\beta}{C_p} i\omega \int_{\mathbf{r}'} H^f(\mathbf{r}', \omega)\, G_\omega(\mathbf{r} \mid \mathbf{r}')\, d\mathbf{r}', \tag{2.6}$$

where the notation of $P^f(\mathbf{r}, \omega)$ means the Fourier image of $P(\mathbf{r}, t)$. The propagator $G_\omega(\mathbf{r} \mid \mathbf{r}')$ is a Green's function which is uniquely determined with the boundary conditions (Morse and Ingard, 1968), and the boundary conditions are given by the cell geometry and its acoustic properties.

The Fourier image of $H(\mathbf{r}, t)$ is obtained from Eq. (2.5) as follows,

$$H^f(\mathbf{r}, \omega) = R(\mathbf{r})\, D^f(\omega)\, M^f(\omega). \tag{2.7}$$

Then the Fourier image of the general solution $P^f(\mathbf{r}, \omega)$ is obtained by substituting Eq. (2.7) into Eq. (2.6), and is

$$P^f(\mathbf{r}, \omega) = \frac{\beta}{C_p} D^f(\omega) M^f(\omega) \left(-i\omega \int_{\mathbf{r}'} R(\mathbf{r}') G_\omega(\mathbf{r} \mid \mathbf{r}')\, d\mathbf{r}'\right)$$

$$= \eta D^f(\omega) M^f(\omega) Q^f(\mathbf{r}, \omega), \tag{2.8}$$

$$\eta = \frac{\beta}{C_p}, \tag{2.9}$$

$$Q^f(\mathbf{r}, \omega) = -i\omega \int_{\mathbf{r}'} R(\mathbf{r}') G_\omega(\mathbf{r} \mid \mathbf{r}')\, d\mathbf{r}.' \tag{2.10}$$

In the general solution of Eq. (2.8), $M^f(\omega)$ and $Q^f(r, \omega)$ are given functions determined by the beam modulation and cell structure, respectively, and $D^f(\omega)$ is a known function. Therefore, PA signals generated in arbitrary samples and PA cells can be analyzed with Eq. (2.8). In Eq. (2.9), η means the mechanical expansion ratio of the medium per unit of thermal energy given in the thermal process. Hence, η express the thermal characteristic of the medium, which affects the PA signal magnitude.

The most characteristic and useful point of the present theoretical model is separation of the PA signal generation into thermal and acoustic processes, with formation of both process explicitly as $D^f(\omega)$ and $Q^f(r, \omega)$, respectively. In particular, spectroscopic and analytical information based on the optical absorption, energy conversion and migration from optical energy to thermal energy in the thermal process can be obtained by investigating the transfer function $D^f(\omega)$, i.e. the Fourier image of the impulse response $D(t)$. On the other hand, various properties of the PA signal which relate to acoustic wave propagation, such as frequency characteristics and magnitude distribution in the cell, can be analyzed with $Q^f(r, \omega)$. For example, $Q^f(r, \omega)$ is applied to instrumentation of the system and to optimization of the cell geometry in the next chapter. However, in conventional theories for liquids, only the acousic process has been investigated extensively (e.g., Kohanzadeh et al., 1975; Patel and Tam, 1981). Similarly, elastic properties and thermal wave propagation have been the main themes in theories for solids (e.g., Jackson and Amer, 1980; McDonald and Wetsel 1978). In addition, although the idea of impulse response was introduced in correlation PAS (Sugitani et al., 1982), it was applied to the total conversion process from optical energy to the detected PA signal, and separation into thermal and acoustic processes was not done. These theories are quite useful in analysis of the mechanical and acoustic properties of PA signals and they have helped

to clarify the basic characteristics of PAS. However little spectroscopic and analytical information is provided by them. Therefore one of the most important intentions of the present theory is its ability to clarify the physical meaning of the PA signal and to derive the spectroscopic and analytical information included in $D'(\omega)$. In subsequent chapters, concrete examples of spectroscopic and analytical applications of the theory, including the instrumentation, are shown.

2.3 Signal Recovery

In the direct coupling method, a piezoelectric transducer is applied to detect the PA signals. Though the piezoelectric transducer is a sensitive detection device for acoustic waves, the piezoelectric signal induced by the PA signal is quite weak because the PA signal itself is a weak acoustic wave. The detected PA signal output is ordinarily in the range of 10^{-1} - 10^{2} μV, and it is buried in the noise field. Therefore various signal recovering methods are used in PAS. For example, a lock-in amplifier is applied in CW PAS (Fig. 2.2), and a boxcar integrator is used in pulse excitation PAS (Fig. 2.3). Random beam modulation combined in a correlator, which is applied in correlation PAS, can also be used for a direct coupling method. In some reviews (e.g., Patel and Tam, 1981), PAS has been methodologically classified according to these signal recovery methods. However, they are all essentially identical and systematically understood. In this section, a general theory for signal recovery in PAS is developed, and the theoretical conclusions which are useful to explain the physical meanings of experimental data in the subsequent chapters are obtained.

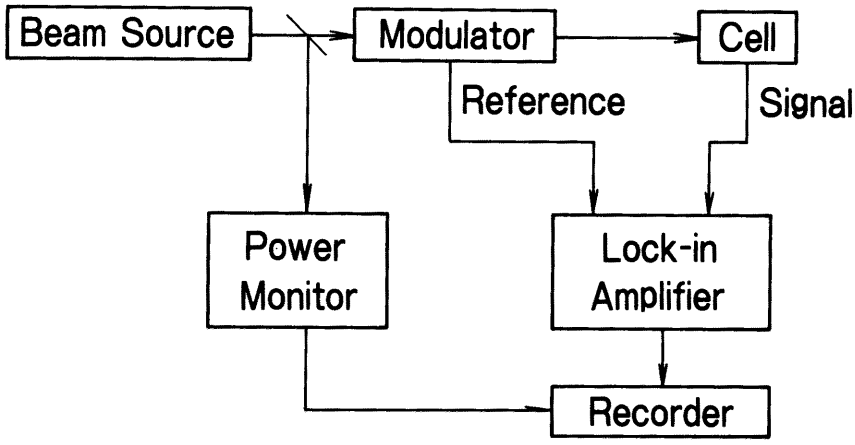

Fig. 2.2 Basic scheme of CW PAS.

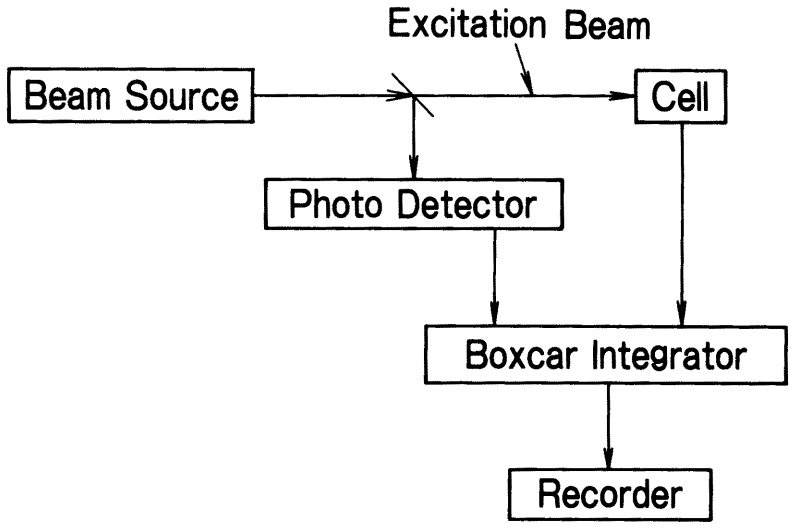

Fig. 2.3 Basic scheme of pulse PAS.

A generallized scheme of signal recovery is shown in Fig. 2.4 and the mathematical explanations of input and output for each structure are noted there. The PA signal generated in the PA cell is detected by the piezoelectric transducer and converted to an electric signal $S(\mathbf{r}, t)$ by the piezoelectric effect. When the spatial response of the piezoelectric transducer is given as $R_s(\mathbf{r})$, the detected PA signal $S(\mathbf{r}, t)$ is written as

$$S(\mathbf{r}, t) = P(\mathbf{r}, t) R_s(\mathbf{r}). \tag{2.11}$$

Generally, in the signal processor of the PAS system, a PA signal is considered to be recovered from noise field $N(t)$ by taking the correlation between the input signal $S(\mathbf{r}, t) + N(t)$ and the reference signal $ref(t-\tau)$, and it can be described as

$$S_r(\tau) = \int ref(t-\tau)\,\{S(\mathbf{r}, t) + N(t)\}\,dt, \tag{2.12}$$

where $S_r(\tau)$ is the recovered signal. The reference functions $ref(t-\tau)$ are sinusoidal, delta, and pseudo random functions for CW, pulse and correlation PAS, respectively, and they correspond to the reference of the lock-in amplifier, the trigger of the boxcar integrator and the reference of the correlator. In all cases, the convolution between the reference $ref(t)$ and the noise $N(t)$ converges to zero, and the convolution between the reference and the signal $S(\mathbf{r}, t)$ remains as an observable physical quantity. Thus, the PA signal is recovered from the noise field.

The physical meanings of the recovered signals, τ, and the reference in each PAS method are summarized in Table 2.1. In CW PAS, the reference function is a sinusoidal function synchronized with the beam intensity modulation; because of the nomalized orthogonalism, only this synchronized

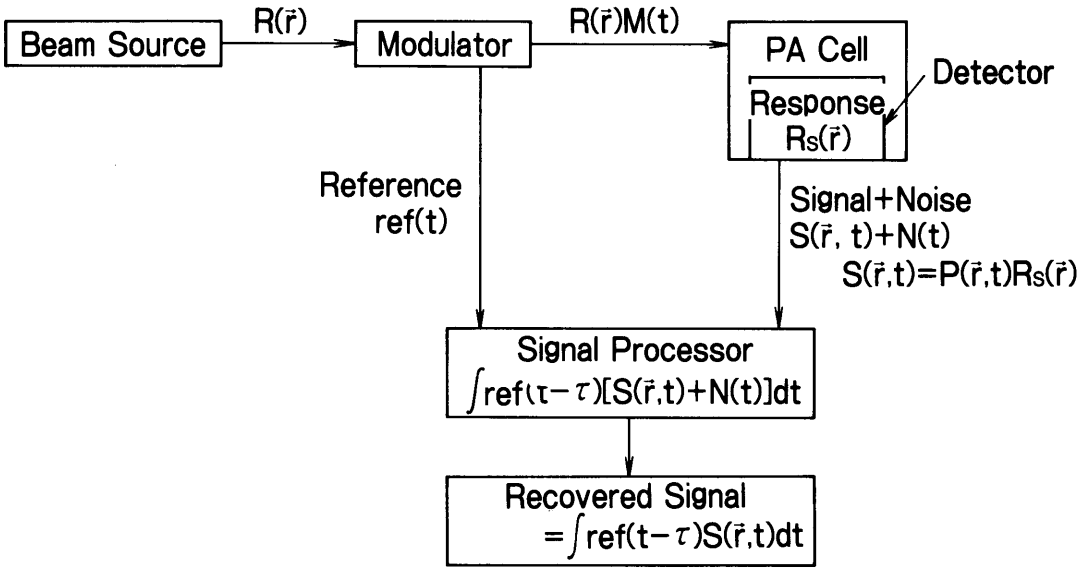

Fig. 2.4 General model for signal recovery in PAS.

Table 2.1. Methodical clasification of PAS.

Item	CW PAS	Pulse PAS	Correlation PAS
Beam Modulation $M(t)$	Rectangular Hev(t) Sinusoidal $e^{i\omega_0 t}$	Pulse $\delta(t)$	Pseudo random $m^*(t)$
Reference $ref(t-\tau)$	Filter function $e^{i\omega_0 t}(t-\tau)$	δ-Function $\delta(t-\tau)$	Pseudo random $m^*(t-\tau)$
Physical meaning of τ	Phase	Sampling timing	Delay time
Signal processor	Lock-in amplifier	Boxcar integrator	Correlator
Information	Signal magnitude Phase	Waveform	Impulse response Delay time

PA signal remains, while the asynchronous components of $S(\mathbf{r}, t)$ and $N(t)$ become zero. Therefore, physically the recovered signal is the signal magnitude of the first Fourier component of the PA signal, and τ is the phase shift of the PA signal from the reference signal. Details are described in the next section under phase sensitive detection, because CW PAS is the main technique employed in the present study.

In pulse PAS, the reference $ref(t)$ is the trigger signal synchronized with a shot of the excitation beam pulse, and it is noted as,

$$ref(t) = \sum_{n=0}^{[tf_p]} \delta(t - \frac{n}{f_p}), \tag{2.13}$$

where f_p is the pulse repetition ratio and the Gaussian notation represented by the bracketed $[x]$ means the maximum integer which does not exceed the value x. From Eqs. (2.12) and (2.13), the signal recovered by the boxcar integrator becomes

$$S_r(\tau) = \int \sum_{n=0}^{[tf_p]} \delta(t - \frac{n}{f_p} - \tau)\{S(\mathbf{r}, t) + N(t)\}\, dt$$

$$= \sum_{n=0}^{[tf_p]} S(\mathbf{r}, \frac{n}{f_p} + \tau) + \sum_{n=0}^{[tf_p]} N(\frac{n}{f_p} + \tau) \tag{2.14}$$

As is statistically evident, the sum of the random noises converges to zero, and the second term of Eq. (2.14) becomes zero for sufficient averaging times $[tf_p]$. On the other hand, ideally, $S(\mathbf{r}, n/f_p + \tau)$ takes the same value for arbitrary n. Hence Eq. (2.14) is rewritten as,

$$S_r(\tau) = [tf_p]\, S(\mathbf{r}, \tau)$$

$$= [tf_p]\, R_s(\mathbf{r})\, P(\mathbf{r}, \tau)$$

$$= N_s R_s(\mathbf{r}) P(\mathbf{r}, \tau) \qquad (2.15)$$

where N_s is the averaging times of the boxcar integrator corresponding to $[tf_p]$. Furthermore, $R_s(\mathbf{r})$ becomes a constant for a well localized detector. Therefore, τ in the basic expression in Eq. (2.12) stands for sampling time in pulse PAS, and Eq. (2.15) which is theoretically derived from the basic equation shows that pulse PAS can obtain the waveform of the PA signal by scanning the sampling time τ.

In correlation PAS, the reference function *ref(t)* is the signal synchronized with the pseudo random beam modulation. Hence the first term of Eq. (2.12) represents the cross-correlation function itself (Uejima et al., 1985; Kirkbright et al., 1984). It is statistically clear that the well correlated component, that is the cross-correlation function, remains in the convolution of Eq.(2.12) while the second term vanishes. Physically τ in correlation PAS is the delay time (Uejima et al., 1985).

As described in this section, the various signal recovery methods in PAS can be systematically understood with the basic expression of Eq. (2.12), and they are all essentially identical. That is, the recovered PA signal is

$$S_r(\tau) = \int ref(t - \tau)\, S(\mathbf{r}, \tau)\, dt. \qquad (2.16)$$

Therefore, a simple comparison of sensitivity and background reduction between these PAS methods, as seen in some reviews (Patel and Tam, 1981; Tam, 1986), has little meaning. The selection of PAS methods must be performed from the viewpoint of the physical quantity to be measured, according to the classification in Table 2.1.

2.4. Signal Magnitude and Phase in CW PAS

In the subsequent chapters on applications, mainly CW PAS is applied in the experiments, and signal recovery in CW PAS, that is the phase sensitive detection with a lock-in amplifier, is intensively discussed with the present theory in order to understand the physical meanings of the obtained signals.

In phase sensitive detection, the reference function *ref(t)* is the filter function,

$$ref(t-\tau) = e^{i\omega_0(t-\tau)}$$

$$= e^{i(\omega_0 t-\theta)}, \qquad (2.17)$$

where $\theta = \omega_0\tau$ is the phase and ω_0 is the beam modulation angular frequency. When the Fourier image of the beam modulation function $M^f(\omega_0)$ is expanded in the following Fourier series

$$M^f(\omega) = \sum_n M_n^f \delta(\omega - n\omega_0), \qquad (2.18)$$

the Fourier image of the detected PA signal is rewritten with Eqs. (2.8) and (2.11) as follows,

$$S^f(\mathbf{r}, \omega_0) = \eta \sum_n M_n^f \delta(\omega - n\omega_0)\, D^f(n\omega_0) Q^f(\mathbf{r}, n\omega_0)\, R_s(\mathbf{r}). \qquad (2.19)$$

where M_n^f is the Fourier coefficient. Hence $S(\mathbf{r}, t)$ can be obtained as the inverse Fourier image of Eq. (2.19), and

$$S(\mathbf{r}, t) = \eta I_0 \sum_n M_n^f \exp(i\omega_0 t) D^f(n\omega_0) Q^f(\mathbf{r}, n\omega_0) R_s(\mathbf{r}). \tag{2.20}$$

From Eqs. (2.17) and (2.20), the convolution of Eq. (2.12) is calculated as

$$S_r(\theta) = \eta M_1^f \exp(i\omega_0 t) D^f(\omega_0) Q^f(\mathbf{r}, \omega_0) R_s(\mathbf{r}), \tag{2.21}$$

because of the normalized orthogonalism of the sinusoidal functions, where the synchronized component of $N(t)$ is assumed to be small in comparison with the first Fourier coefficient M_1^f. Therefore, Eq. (2.21) shows that the recovered PA signal in phase sensitive detection is the first Fourier component of the PA signal.

Using polar coordinates to express in the complex space, Eq. (2.21) is represented as

$$S = | S_r(\theta) | \sin(\theta - \phi) \tag{2.22a}$$

$$= \eta M_1^f | D^f(\omega_0) Q^f(\mathbf{r}, \omega_0) | R_s(\mathbf{r}) \sin(\theta - \phi), \tag{2.22b}$$

$$\phi = \arg D^f(\omega_0) + \arg Q^f(\mathbf{r}, \omega_0), \tag{2.23}$$

where S and ϕ are the magnitude and phase of the PA signal. In the lock-in amplification, S and θ are the in-phase output and the phase of the lock-in amplifier.

As mentioned in section 2.2, one of the most useful points of the present theory is its ability to separate the thermal process from the acoustic process, and to be describe them mathematically with $D^f(\omega_0)$ and

$Q^f(r, \omega_0)$. In addition, information about $D^f(\omega_0)$ and $Q^f(r, \omega_0)$ is contained in the recovered signal in CW PAS, and these terms can be analyzed with Eqs. (2.22) and (2.23). Various spectroscopic and analytical applications and instrumentation will be developed in the subsequent chapters on the basis of these theoretical conclusions.

2.5 Verification of Theory

To verify the general theory developed in the former sections, frequency characteristics of PA signals generated in a cylindrical direct coupling cell are analyzed, and the theoretical results are investigated experimentally. The excitation beam is treated as a Gaussian beam in rectangular modulation, in which the laser beam modulation with a light chopper or an acousto-optic modulator in the experiments is taken into consideration.

First, a mathematical expression of the frequency characteristics of the PA signal magnitude in a cylindrical direct coupling cell is obtained from the general theory in sub-section (a). To verify the analytical results, the dependence of PA signal magnitude on light modulation frequency is measured in experiment A of sub-section (b). The frequency characteristics of PA signals include not only the thermoelastic wave induced by the laser beam, but frequency characteristics of the PZT detector and structural vibration properties of the cell. Experiments B and C in sub-sections (c) and (d) are performed to separate these last two properties which are not of immediate concern in the theoretical section.

(a) Analytical results of frequency characteristics

The analytical model is shown in Fig. 2.5. The PZT cylinder is treated as a sound absorber, occupying $a \leqq r \leqq b$. The laser beam passing through the region $0 \leqq r \leqq r_0$ has a Gaussian distribution, where r_0 is the e^{-2} point of the peak intensity of the laser beam, and it is modulated in a rectangular function. In this model, two assumptions are used: the model is axially symmetric and the thermal diffusion length is negligibly shorter than the radius of the laser beam as is discussed in sections 2.1 and 2.2. Under these assumptions, the heat generated by the incident laser beam is not accompanied by thermal diffusion, and thermal energy is instantaneously converted into the mechanical energy of the thermoelastic wave. Therefore, the impulse response of the thermal process $D(t)$ of Eq. (2.3) becomes the following δ-function for weak absorption materials,

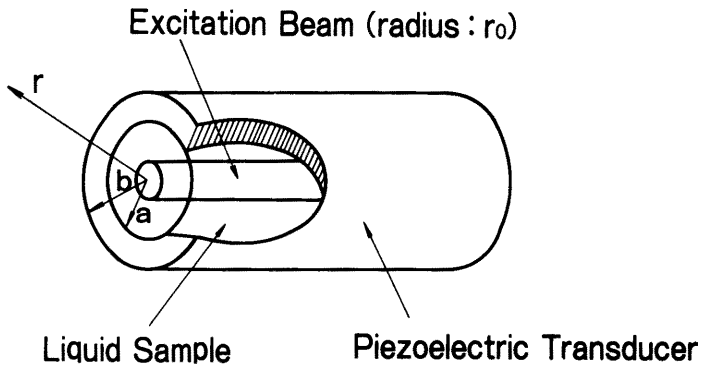

Fig. 2.5 Analytical model of cylindrical PA cell for liquids based on the direct coupling method.

$$D(t) = \alpha I_0 \delta(t)$$

and its Fourier image becomes

$$D^f(\omega) = \alpha I_0. \tag{2.24}$$

Details of the physical meanings of Eq. (2.24) are discussed in Chapter IV.

The functions of $R(r)$ and $M(t)$ for Gaussian beam profile and rectangular modulation are given as follows:

$$R(r) = \sqrt{\frac{\pi}{2}}\,\frac{\gamma}{r_0}\exp\left(-\frac{2\gamma^2}{r_0^2}r^2\right) \tag{2.25}$$

$$M(t) = \frac{k}{f}\sum_{n=o}^{[tf]}\left(\mathrm{Hev}\,(t-\frac{n}{f}) - \mathrm{Hev}\,(t-\frac{n}{f}-\tau)\right) \tag{2.26}$$

where α is the light absorption coefficient; γ, a beam expansion coefficient; f, the modulation frequency; τ, the pulse dulation, and $[x]$ and $\mathrm{Hev}(x)$ denote a Gaussion notation and Heaviside function. The coefficients $(\pi/2)^{1/2}\gamma/r_0$ and k/f are introduced as nomalizing factors of the distribution functions $R(r)$ and $M(t)$. In particular, k/f is a non-dimensional proportionality constant which means that the number of photons in one light pulse is inversely proportional to the light modulation frequency (Appendix A). In high frequency modulation ($f \to \infty$), the rectangular modulation of Eq. (2.26) is considered as a series of pulses ($\tau \to 0$) and its time derivative becomes a series of δ-functions using the definition of the δ-function,

$$\frac{d}{dt}M(t) = \lim_{\tau \to 0} \frac{k}{f} \sum_{n=o}^{[tf]} \left(\mathrm{Hev}\,(t - \frac{n}{f}) - \mathrm{Hev}\,(t - \frac{n}{f} - \tau) \right)$$

$$= \frac{k}{f} \sum_{n=o}^{[tf]} \delta\,(t - \frac{n}{f}). \tag{2.27}$$

Hence the Fourier image of Eq. (2.27) is given as,

$$i\omega M^f(\omega) = \frac{k}{f} \sum_{n=o}^{[tf]} e^{-i\omega \frac{n}{f}}$$

$$M^f(\omega) = \frac{1}{i\omega} \frac{k}{f} \sum_{n=o}^{[tf]} e^{-i\omega \frac{n}{f}}. \tag{2.28}$$

The boundary conditions of this model are that the wave function is smoothly continuous at $r = a$ and convergent in the region $a \leqq r \leqq b$. Therefore Green's function can be expressed as,

$$G_\omega(\mathbf{r}, \psi \,|\, r', \psi') \tag{2.29}$$

$$= -\frac{i}{4} \sum_{m=0}^{\infty} \varepsilon_n \cos m(\psi - \psi')\, \mathrm{H}_m^{(1)}(\frac{r}{v}\omega)\, \mathrm{J}_m(\frac{r'}{v}\omega),$$

where $\mathrm{H}^{(1)}_m(x)$ is a Hankel function of the first kind; $\mathrm{J}_m(x)$, the Bessel function; ε_n, the Neumann factor; ψ and ψ' are the arguments of r and r', respectively.

From the above discussion, all the functions $D^f(\omega)$, $M^f(\omega)$, $R(\mathbf{r})$ and $G_\omega(\mathbf{r}\,|\,\mathbf{r}')$ in Eq. (2.8) are given concretely, hence the Fourier image of the PA signal $P^f(\mathbf{r}, \omega)$ is then given and the PA signal $P(\mathbf{r}, t)$ can be obtained as

an inverse Fourier image of it. On the other hand, the piezoelectric signal is proportional to the magnitude of the pressure wave $<P>$, and the response function $R_s(r)$ is

$$R_s(r) = rg \tag{2.30}$$

where g is the g value of the piezoelectric constant. Consequently, the detected PA signal magnitude S at $r = a$ is given as follows:

$$S = ag <P>$$

$$= ag \left(P(a,t) \cdot P^*(a,t)\right)^{\frac{1}{2}}$$

$$= \sum_{m=0}^{l+1} \xi \frac{k}{f} a I_0 \frac{\gamma}{r_0} a R_p(a) A_m(a,f) \tag{2.31}$$

$$\xi = \frac{\pi^2}{\sqrt{2}} v \frac{\beta}{C_p} g \tag{2.32}$$

$$l = [\frac{r_0 t}{2\gamma v}] \tag{2.33}$$

$$R_p(a) = \exp(-2\gamma^2 \frac{a^2}{r_0^2}) \left(I_0^2 (\frac{2\gamma^2 a^2}{r_0^2}) + \frac{1}{\pi^2} K_0^2 (\frac{2\gamma^2 a^2}{r_0^2}) \right)^{\frac{1}{2}} \tag{2.34}$$

$$A_m(a,f) = e^{-(4\gamma^2 v^2 m^2 / r_0^2 f^2)} I_0(\frac{8\gamma^2 a v}{r_0^2 f} m) \tag{2.35}$$

where $I_0(x)$ and $K_0(x)$ are modified Bessel and Hankel functions, respectively.

From the analytical result of Eqs. (2.31) - (2.35), the frequency characteristics of the PA signal are obtained as $f^{-1}A_m(a,f)$. The calculated frequency characteristics of the PA signal $f^{-1}A_m(a, f)$ is plotted in Fig. 2.7(a).

(b) Frequency characteristics of PA signal: Experiment A

The dependence of the PA signal on light modulation frequency is measured using an aqueous sample of Sunset Yellow dye. The experimental setup is the same as Fig. 2.2, and the PA cell is shown in Fig. 2.6. The experimental parameters are listed in Table 2.2. The PA signal detected by the piezoelectric transducer based on the compound PZT ($Pb_{x-2}(Zr, Ti)_xO_2$) is amplified with the use of the lock-in amplifier referenced to the signal from the beam modulator. Results of this experiment are shown in Fig. 2.7(b). Six peaks appear in the figure. These peaks include some which are properties of the PZT and the cell structure.

(c) Natural frequency of the PA cell: Experiment B

Since the PA signal is a pressure wave, it causes not only the PZT detector, but the entire cell body to vibrate. Resonances for the structural eigen vibration of the cell may be seen in Fig. 2.7(b). Experiment B aims at separating these resonances from the peaks observed.

The cell is filled with only water which hardly absorbs the 488 nm beam or generates a promising thermoelastic pressure wave in comparison with the sample dye solutions. The laser beam is directed at an angle with respect to the cell axis, so as to illuminate the PZT detector directly through the water.

Table 2.2. Parameters for experiments and analytical solutions.

Symbol	Parameter	Value
a	Cell inner radius	1.1 cm
b	Cell outer radius	1.3 cm
r_0	Laser beam radius	6.0 x 10^{-2} cm
v	Sound wave velocity	
	in water at 27 °C	1.6 x 10^5cm/s
I_0	Excitation beam power	50 mW
-	Excitation beam wavelength	488 nm (Ar - Laser)
-	Sample concentration	5.0 x 10^{-6} mol/cm3
L	Cell length	9.0 cm
-	PZT length	5.0 cm

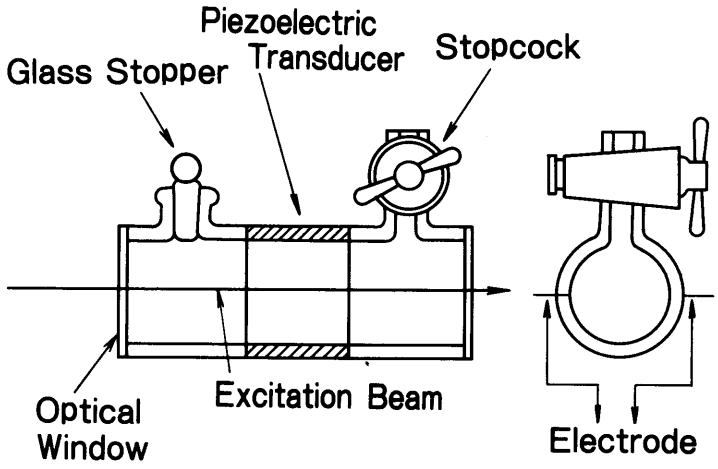

Fig. 2.6 Structure of the cylindrical PA cell for liquids.

The results obtained are plotted in Fig. 2.7(c) in which five peaks are shown. These peaks may still include electrical resonances of the PZT detector.

(d) Electrical resonances of the PZT detector: Experiment C

The piezoelectric signal induced by external mechanical vibration, such as PA signals, corresponds to the electrical resonance frequencies. Experiment C identifies some peaks appearing in Figs. 2.7(b) and 2.7(c) as being electrical resonances of the PZT detector.

The same PA cell is used as previously, but this time it is empty, and the inlet and the outlet are left open to maintain atmospheric pressure inside. The excitation beam is directly exposed on the inner surface of the cylindrical PZT as in experiment B.

The piezoelectric signal measured from 0.2 to 200 kHz is plotted in Fig. 2.7(d). Resonance points of the PZT detector appear at 20.0 and 40.8 kHz.

To confirm that these are the PZT electrical resonances, impedance between the two poles of the detector is measured from 0.2 to 200 kHz. The impedance of the PZT changes from 10^0 to 10^4 Ω at each electrical resonance point. These measured resonance points are indicated by solid vertical lines in Fig. 2.7(d). There is a one-to-one correspondence for the vertical lines and resonance peaks of the curve at 20.0 and 40.8 kHz. Furthermore, these peaks have spurious signals on the higher frequency side of the peaks which are peculiar to PZT (Onoe et al., 1963), and which also correspond to measured resonance peaks.

(e) Results and discussion

An inverse relationship is seen for frequencies below 1 kHz, both in the theoretical results of Fig. 2.7(a) and the experimental results of Fig.

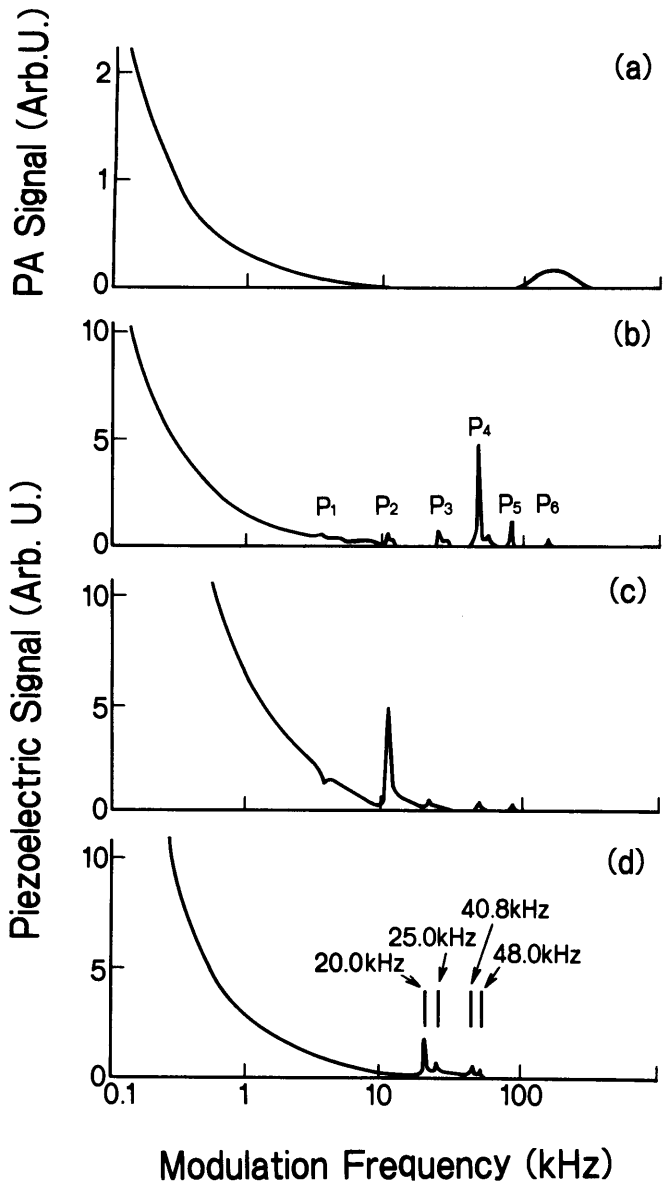

Fig. 2.7 (a) Frequency characteristics of PA signal: analytical solution obtained using Eqs.(2.31) and (2.35) (sample: Sunset Yellow dye). (b) Frequency characteristics of PA signal; experimental results (sample: Sunset Yellow dye). (c) and (d) Frequency characteristics of the piezoelectric signal induced by thermoelastic vibration at the point directly illuminated by the laser beam on the inner surface of the cylindrical PZT detector. The peaks shown in (c) are structual resonances of the water-filled cell and electrical resonances of the PZT detector. The peaks shown in (d) are electrical resonances of the PZT detector as determined using an empty cell, left open to atmospheric pressure. Electrical resonances measured by an impedance meter are indicated by the solid vertical lines in (d).

2.7(b). The f^{-1} dependence is due to the I_0/f term in Eq. (2.31) which represents the decrease of incident photoenergy per light pulse. Neither theoretical nor experimental analysis show f^{-1} dependence above 1 kHz due to the contribution of the $A_m(a, f)$ term in Eq. (2.35). In this region $A_m(a, f)$ is no longer 1 for $m = 1$. The relationship between l and f in Eq. (2.33) shows that the summation of Eq. (2.31) must take values of $m = 0$ and $m = 1$ in the region of 1 kHz $\leqq f \leqq$ 10 kHz. The physical meaning of this exponential attenuation is that the contribution of the thermoelastic wave for mode $m = 1$ to the PA signal magnitude is not negligible in comparison with that of the basic thermoelastic wave for mode $m = 0$.

The peaks at 153 kHz which appear in both Figs. 2.7(a) and 2.7(b) are the acoustic resonance peaks. The resonant conditions are obtained from Eq. (2.31), and are

$$f = \frac{v}{a} m. \tag{2.36}$$

Equation (2.36) means that these peaks are resonances of the thermoelastic wave, which do not depend on the incident laser beam profile, but only on the cell geometry. The experimental resonance P_6 which appears at 153 kHz corresponds to $m = 1$. The sound velocity calculated from Eq. (2.36) is 1.68×10^5 cm/s, and this agrees well with the sound velocity in water at 27 °C. Peak P_6 shown in the experimental curve is sharper than that of the theoretical result. This seems to be influenced by two-dimensional beam extension and by other factors which have not been considered, for example the energy damping factor on the beam - medium and PZT - liquid boundaries.

The present analysis is concerned only with the acoustic wave generated by the excitation beam, and does not consider the characteristics of the PZT detector. Therefore peaks P_1 to P_5 in Fig. 2.7(b) do not appear

in the theoretical results in Fig. 2.7(a). The physical meanings of peaks P_1 to P_5 are explained by the results of experiments B and C. As mentioned in sub-section (c), the peaks shown in Fig. 2.7(d) are electrical resonances of the PZT detector. Peaks P_3 and P_4 in Fig. 2.7(b) correspond closely to these peaks, as well as having spurious signals on the higher frequency side (Onoe et al., 1963). Therefore peaks P_3 and P_4 are electrical resonances of the PZT detector. When the physical meanings of peaks P_3, P_4 and P_6 are known, the remaining ones, P_1, P_2 and P_5 can be explained as structural resonances of the entire cell body, based on the results of experiment B. The three peaks at 3.0, 10.8 and 86.0 kHz in Fig. 2.7(b) agree with the peaks in Fig. 2.7(c) which represent structural resonances of the water-filled cell. Theoretical calculations (Appendix B) confirm that these peaks correspond to the following modes: peak P_1 is the bending mode; peak P_2 is the torsional mode; and peak P_5 is the longitudinal mode resonance of the second harmonic.

As seen in the above discussion, the f^{-1} characteristics of the PA signal and the acoustic resonance point which are obtained in the theoretical analysis agree well with the experimental results, and the physical meanings of these frequency characteristics are clearly explained by the theory. Therefore the propriety of the present theory is confirmed. The superimpositions of the modes and resonances are the characteristics of the acoustic wave, and the wave equation of Eq.(2.2) is necessary to analyze these characteristics of PA signals. Therefore the simple adiabatic expansion model presented by Patel and Tam (1981) does not describe these acoustic properties of PA signals in high repetition pulse excitation. Futhermore wave generation, propagation, and attenuation in a closed cell strongly depend on the profile of the wave source and the boundary conditions in general. Equation (2.8) shows the effect of the source profile explicitly. From this viewpoint, the δ-functional treatment

of the excitation beam by Kohanzadeh et al. (1975) and Atalar (1980) do not correctly express the acoustic source term, and their theories do not explain exactly these frequency characteristics of PA signals generated in a cylindrical cell. Consequently the wave equation (2.2) is need to describe the acoustic properties of PA signals in liquids. As a general solution of Eq. (2.8) gives the PA signal amplitude, phase, and wave profile, the characteristics of PA signals for any detection method and cell are described by it, with the suitable Green's functions.

In this section, the characteristics of PA signal concerned with wave propagation were examined both theoretically and experimentally for the verification of the theory. In subsequent chapters for applications, various properties of PA signals which are related to energy migration and are represented as $D'(\omega)$ of general solution of Eq. (2.8) are applied to spectroscopic and analytical applications, as well as the acoustic properties discussed here.

2.6 Conclusion

The PA effect was described with a generalized linear transform equation and wave equation of thermally forced motion which represented the energy conversion process from optical energy to thermal energy (thermal process) and acoustic signal generation and propagation (acoustic process), respectively. This coupling equation was solved using linear response theory and Green's functions. The theoretical results showed that the thermal process was described mathematically by the transfer function $D'(\omega_0)$ which was a Fourier image of the impulse response function $D(t)$ for energy conversion, and the acoustic process was expressed by $Q(\mathbf{r}, t)$ which was a convolution between the source profile and the propagator given as the

Green's functions. The properties of the PA signal related to the thermal process, which included energy conversion and migration such as nonradiative relaxation and thermal diffusion, could be analyzed from $D^{\prime}(\omega_0)$, and are applied to the analytical chemistry and spectroscopic applications in later chapters. On the other hand, the acoustic properties of the PA signal could be analyzed with $Q(r,t)$, and they were used for instrumentation. The signal detection and recovery method in PAS was also discussed based on the theory, and the physical meanings of the detected PA signals were clarified. The methodological difference between CW, pulse and correlation PAS was discussed theoretically, and it was shown that these methods were substantially identical. Finally, the propriety of the general theory was confirmed by comparisons between theoretical and measured results of frequency characteristics of PA signals.

CHAPTER III INSTRUMENTATION

As mentioned in the first chapter, various analytical and spectroscopical application of PAS have been successfully shown experimentally. Especially in analytical chemistry the direct coupling method for liquid phase samples has been applied effectively as a weak absorbance detector, including as a detector for liquid chromatography (Oda and Sawada, 1981) or double beam colorimetry (Sawada and Oda, 1981), and its potential as a hypersensitive tool has been noted. However the parameters of the PAS system have not been optimized, because properties of the PA signals in liquids have not been clarified nor has the design method of PAS equipment been established.

Providing good instrumentation for PAS can be summarized into a few simple problems: how to excite the PA signal effectively; how to detect it ultrasensitively and dynamically; and how to recover it from a high level background noise field. In Chapter III, the excited, detected and recovered PA signal is described using the generallized theory. These problems can be analyzed with the modulation function of the excitation beam $M(t)$, detected PA signal $S(\mathbf{r}, t)$ and the recovered signal $S_r(\mathbf{r}, t)$, respectively. Then, in the first two sections, distribution of PA signal magnitude and optimal geometrical conditions for PA signal detection are discussed on the basis of the theory and experimental results (Kitamori et al., 1985a). The influence of the thermal lens effect on PA signal generation and detection is also clarified. Following that, some important conditions of beam modulation which is related to the signal excitation, and the lock-in amplification for signal recovery are discussed (Kitamori and Sawada, 1988c). Finally, a hypersensitive PAS system is designed and the design method is proved experimentally

(Kitamori et al., 1985d). The integrated system efficiency, including the minimum detectable absorption coefficient of the PAS system, is discussed.

3.1 Dependence of Signal Magnitude on Geometrical Conditions of Cylindrical PA Cell

In this section, dependence of signal magnitude on the geometrical conditions of the excitation beam and the cylindrical PA cell are analyzed theoretically. The theoretical results are confirmed experimentally. The physical meaning of the beam expansion coefficient γ is clarified to be the thermal lens effect, based on the consequent discussions.

(a) Theoretical

Photoacoustic signals generated and detected in a cylindrical PA cell with a Gaussion beam profile and rectangular beam modulation were analyzed in Chapter II, and a concrete form of the detected PA signal S was given with Eqs. (2.31) - (2.35). Under typical experimental conditions for PAS applications in analytical fields, the beam modulation frequency f is on the order of 10^1 - 10^2 Hz, and the beam radius r_0 is on the order of 10^{-1} - 10^0 mm. (Lahman et al., 1977; Oda et al., 1978 and 1980; Oda and Sawada, 1980). With these experimental conditions, as shown in Eq. (2.33), the main contributing mode m to the PA signal is m = 0 because v is on the order of 10^3 m/s, and the $A_m(a, f)$ term becomes $1/f$. Therefore, the detected PA signal magnitude of Eq. (2.31) is given as

$$S(a)=\xi\frac{aI_0}{f}\frac{\gamma a}{r_0}R_p(a) \tag{3.1}$$

The nondimensional parameter ζ, which expresses the ratio of the cell radius to the beam radius in the liquid sample is introduced as

$$\zeta=\gamma\frac{a}{r_0} \tag{3.2}$$

where it should be noted that r_0 is the beam radius in air and r_0/γ is the beam radius in the liquid samples. Hence ζ means the ratio of the cell radius and the beam radius in the sample. Using Eq. (3.2), Eqs. (3.1) and (2.34) are simplified as follows,

$$S(\zeta)=\xi\frac{aI_0}{f}\zeta R_p(\zeta), \tag{3.3}$$

$$R_p(\zeta)=e^{-2\zeta^2}\left(I_0^2(2\zeta^2)+\frac{1}{\pi^2}K_0^2(2\zeta^2)\right)^{\frac{1}{2}}, \tag{3.4}$$

and Eq. (2.30) is rewritten as

$$R_s(\zeta)=\frac{g}{\gamma}\zeta. \tag{3.5}$$

It is apparent from the derivation of Eq. (2.31) that the ζ term in Eq. (3.3) originates in the ζ term of Eq. (3.5), because the detected PA signal $S(a)$ is obtained by the product of the PA signal magnitude $<P(a)>$ and the spatial response of the PZT detector $R_s(a)$ as shown in Eq. (2.11). The function $R_p(\zeta)$ of Eq. (3.4) originates in the convolution between the Gaussion source profile of Eq. (2.25) and the propagator $G_\omega(r|r')$ of Eq. (2.29) represented in Eq. (2.10), hence the physical meaning of $R_p(\zeta)$ is given as the radial dependence of the PA signal magnitude.

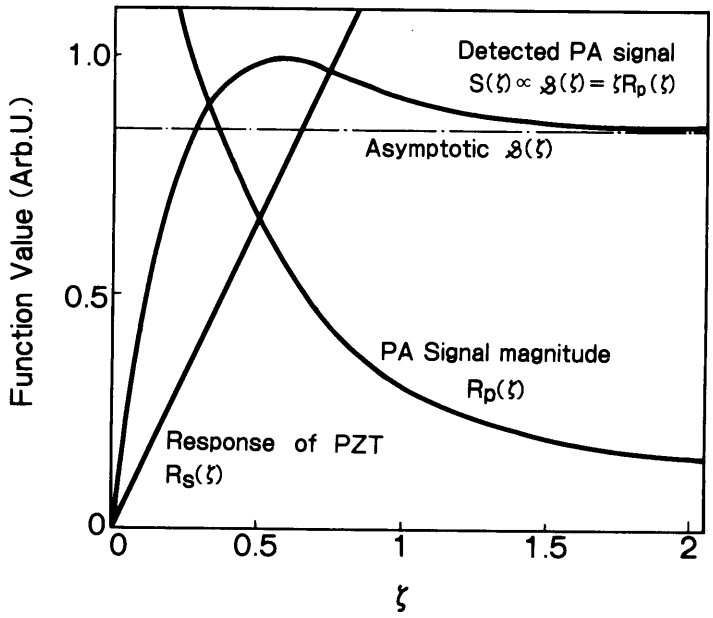

Fig. 3.1 The calculated values of $S(\zeta)$, $\mathcal{S}(\zeta)$, $R_p(\zeta)$ and the PZT response $R_s(\zeta)$.

Thus, the dependence of the PA signal magnitude $R_p(\zeta)$ and the detected one $S(\zeta)$ on the geometrical condition ζ is obtained theoretically as shown in Eqs. (3.3) and (3.4). The results of numerical calculation for $S(\zeta)$ and $R_p(\zeta)$ are plotted in Fig. 3.1.

(b) Measurement of PA signal magnitude on cell radius

To verify the analytical results, the dependence of PA signal magnitude on the cell radius is measured using *m*-xylene as the liquid sample. Equation (3.3) shows that $S(\zeta)$ and the sensitivity which is defined as the derivative of $S(\zeta)$ with respect to a is a proportional relationship. Therefore, the dependence of the sensitivity on the cell radius can be obtained by measuring the dependence of the PA signal magnitude on the cell radius. Details of sensitivity, with its strict definition are given in section 3.2.

A schematic of the PA cell used in these experiments is shown in Fig. 3.2. A cylindrical PZT is mounted in the center of the quartz glass

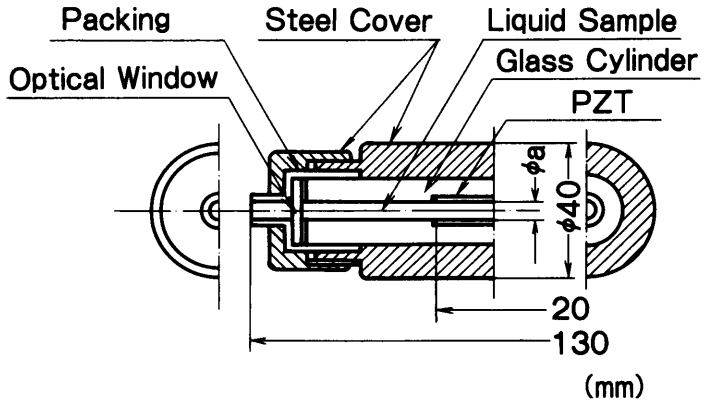

Fig. 3.2 Schematic of cylindrical PA cell for liquid samples. Four cells with different radii (a = 3.5, 4.5, 5.5 and 6.5 mm) are used. The optical windows and the glass cylinder are made of quartz.

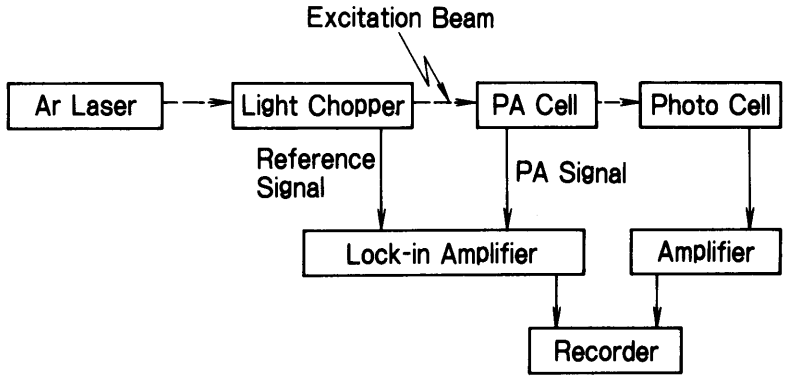

Fig. 3.3 Experimental set up of PAS for liquid samples.

cylinder. The liquid sample is poured into the cylinder by removing the quartz optical window. The whole cell is covered with a stainless steel cover to eliminate outside electro-magnetic and mechanical noise. Four cells with radii varying from 3.5 to 6.5 mm are used.

The experimental set up for liquid samples is shown in Fig. 3.3. The excitation beam is the 488 nm emission line of an Ar laser, and the emission mode is TEM_{00} which has a Gaussian profile. The beam is modulated as a series of rectangular pulses. The PA signal detected by the cylindrical PZT is amplified by the lock-in amplifier in syncronization with a reference signal from the driver of the light modulator.

The excitation beam profile in air of this spectrometer is measured for rectangular and circular slits by the following procedure. The rectangular slit (width: 0.5 mm) and the circular slit (radius d: variable) are set in that order at the PA cell center (Fig. 3.3). The power of the beam passing through the slit is measured with a light power meter. The Gaussian beam power $W(d)$ passing through the slit of radius d is described as

$$W(d) = \int_0^d I_0 e^{-(2r^2/r_0^2)} dr$$

$$= \frac{1}{\sqrt{2\pi}} I_0 \mathrm{Erf}(\frac{2d}{r_0}), \qquad (3.6)$$

where $\mathrm{Erf}(x)$ is an error function. The measured beam power is plotted in Fig. 3.4 along with calculated results of Eq. (3.6) for r_0 = 1.0, 2.0 and 3.0 mm. The calculated values are normalized using the beam power of $d \rightarrow \infty$, while the experimental values are normalized using the value obtained

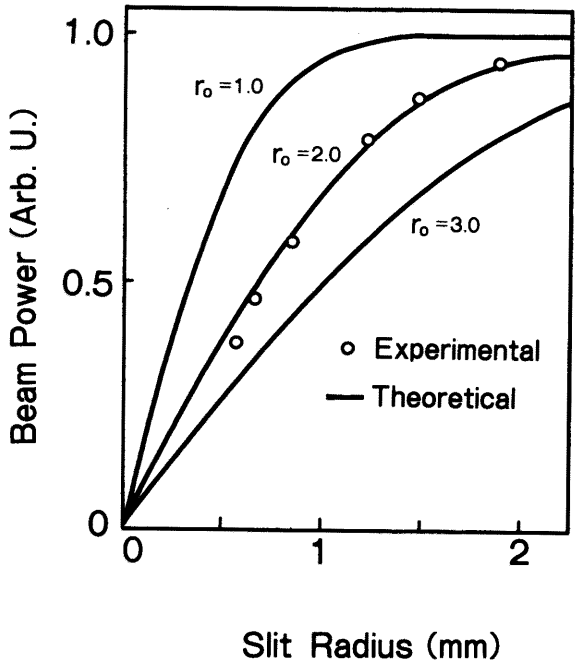

Fig. 3.4
Dependence of detected beam power on the radius of the slit. The theoretical curves are calculated with Eq. (3.6) and normalized using the beam power of $d \rightarrow \infty$.

when the circular slit is left open. From comparison of the experimental and calculated values, the beam radius of the excitation beam is obtained as 2.0 mm.

The PA signal magnitudes for *m*-xylene are measured in four different sized cells. The parameters used are listed in Table 3.1. The results obtained are plotted in Fig. 3.5, along with the calculated value of $S(\zeta)$ for γ = 0.23, 0.25 and 0.27.

(c) Results and discussion (1): Analytical model

In Fig. 3.1, the calculated value of $R_p(\zeta)$ which expresses the radial dependence of the PA signal magnitude shows monotonic decreasing properties, while $S(\zeta)$ has a maximum value and is nearly constant for large ζ values. From the definition of ζ in Eq. (3.1), it can be used to express the ratio of the cell radius to the beam radius in liquid. Therefore, large ζ values mean a far field condition where the beam profile can be neglected in comparison with the cell radius, and small ζ values mean a near field condition. In the far field, $R_p(\zeta)$ attenuates to nearly $1/\zeta$, while it strongly depends on the excitation beam profile in

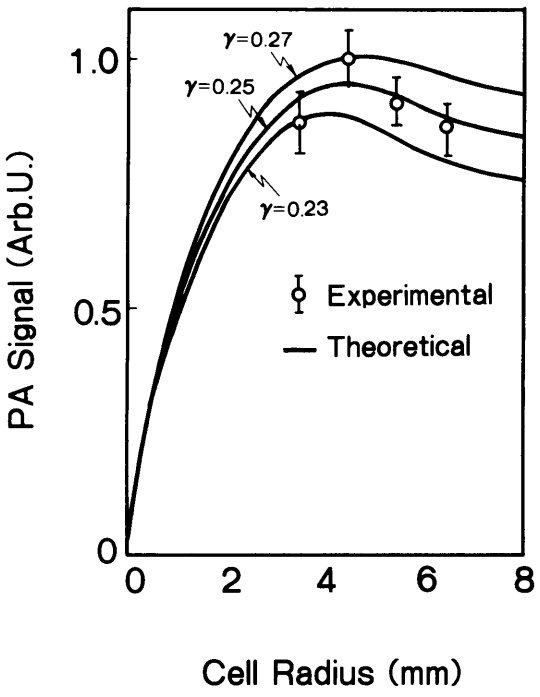

Fig. 3.5
Dependence of detected PA signal on cell radius. The theoretical curves for γ = 0.23, 0.25 and 0.27 are calculated with Eq. (3.7). The parameters used are listed in Table 3.1.

Table 3.1. Experimental parameters.

Symbol	Parameter	Value
a	Cell radius	3.5, 4.5, 5.5 and 6.5 mm
L	Cell length	100 mm
r_0	Beam radius	2.0 mm
I_0	Beam power	1.6 W
f	Beam modulation frequency	80 Hz

the near field as shown in Eq. (3.4). On the other hand, as the sensitivity of the PZT detector is proportional to the cell radius a, i.e, proportional to ζ, the magnitude of the detected PA signal $S(\zeta)$, expressed as the product of ζ and $R_p(\zeta)$ becomes constant in the far field and has its maximum in the near field.

To verify these theoretical results for PA signal detection, the dependence of PA signals on cell radius is measured, and the results are shown in Fig. 3.5. The experimental values fall between the theoretical curves for γ = 0.23 and γ = 0.27, and they correspond to the theoretical curve for γ = 0.25 within an experimental error of 6%. The error can be attributed to purity of the sample, or power instability of the beam source.

Consequently the experimental results verify the theoretically obtained dependence of the PA signal magnitude on the cell radius, except for verification of the propriety of the γ value which is obtained only by parametric calculations. The physical meaning and the value of γ are discussed in the next sub-section.

(d) Results and discussion (2): Thermal lens effect in PAS

In Eqs. (3.2) - (3.4), and in the experimental verification of the former sub-section, γ is shown to be the parameter which determines the function value of $S(\zeta)$ and $R_p(\zeta)$. The parameter r_0 is the radius of the excitation beam in air, and its spatial distribution in the liquid sample is rewritten as

$$\exp\left(-\frac{2\gamma^2}{r_0^2}r^2\right) = \exp\left(-2r^2/(\frac{r_0}{\gamma})^2\right).$$

Therefore r_0/γ means the excitation beam radius in the liquid sample and $1/\gamma$ expresses its beam enlargement factor. The enlargement effect of the Gaussian beam by the liquid sample is known as the thermal lens effect (Fang and Swofford, 1983). The Gaussian beam causes a Gaussian distribution of temperature in the liquid sample, which gives the Gaussian profile of the sample refractive index. This refractive index field acts as a concave lens. The beam enlargement factor $1/\gamma$ due to the thermal lens effect is given as follows (Swofford and Morrel, 1978; Twarowski and Kliger, 1977),

$$\gamma^{-2} = 1 + \frac{\alpha I_0 l_s}{\kappa}\left(-\frac{1}{\lambda}\left(\frac{dn}{dT}\right)\right), \tag{3.7}$$

where κ is the thermal conductivity; l_s, the sample length; λ, the wavelength of the excitation beam; and n, the refractive index. For an transparent organic solvent such as benzene or xylene, Eq. (3.7) is approximated as (Twarowski and Kliger, 1977):

$$\gamma^{-1} = (1 + 2.3 I_0 l_s)^{1/2}, \tag{3.8}$$

where I_0 and l_s are the beam power in watts, and sample length in cm, respectively.

The excitation beam is ascertained to be the Gaussian beam with r_0 = 2.0 mm from the results shown in Fig. 3.4. The value of γ is calculated as 0.23 by Eq. (3.8), because l_s = 5.0 cm, which is half the cell length, and also the sample length from the optical window to the PZT detector.

From the results in Fig. 3.5, the value of γ is obtained as $\gamma = 0.25 \pm 0.02$ with the parametric calculations. The theoretical value of $\gamma = 0.23$ obtained with Eq. (3.8) corresponds well with the experimental value of $\gamma = 0.25 \pm 0.02$. Therefore the physical meaning of γ is confirmed to be the beam enlargement coefficient due to the thermal lens effect.

Generally the dominant factor which determines the geometrical configuration of an acoustic source term of PA signals is thermal diffusion in solid and gas samples. However, the thermal diffusion length in xylene is on the order of 10^0 to 10^1 μm for the beam modulation frequency region of 10^1 to 10^2 Hz, on the other hand the beam is expanded several times by the thermal lens effect under the present experimental conditions. Therefore, in this case, the acoustic source term of the PA signal is hardly affected by thermal diffusion, and the thermal lens effect is the dominant factor for determining geometrical configuration of the acoustic source term in the wave equation. Equation (3.7) shows that when a high intensity beam is used for PA signal generation in liquids for which the temperature coefficient of the refractive index is high, the thermal lens effect becomes one of the main factors for determination of the acoustic source profile.

3.2 Sensitivity Characteristics and Optimal Design Method for Cylindrical PA Cell

The physical meanings of the geometrical dependence and the effect of thermal lens effect on PA signal were outlined in section 3.1. Now, the sensitivity characteristics can be analyzed and the conditions of PA signal detection for samples of various absorbances can be optimized.

The sensitivity of PAS means the slope of the calibration curve, that is the ratio of the signal increase to the variation of the absorbance, and it is obtained from Eq. (3.3) as

$$\frac{d}{da}S(\zeta)=\xi\frac{I_0}{f}\zeta S(\zeta)+\xi\frac{aI_0}{f}\frac{d}{da}(\zeta S(\zeta)). \tag{3.9}$$

When the term $\zeta S(\zeta)$ is rewritten as $\&(\zeta)$, Eqs. (3.9) and (3.3) are rewritten as

$$\frac{d}{da}S(\zeta)=\xi\frac{I_0}{f}\&(\zeta)+\xi\frac{aI_0}{f}\frac{d}{da}\&(\zeta), \tag{3.10}$$

$$S(\zeta)=\xi\frac{aI_0}{f}\&(\zeta). \tag{3.11}$$

In analytical and spectroscopic applications, the sensitivity must be kept constant for variations of a to ensure linearity of the detected PA signal $S(\zeta)$ versus absorbance a. However, as shown in Eqs. (3.2) and (3.7), ζ changes with absorbance a because of the thermal lens effect of γ, hence the functions $S(\zeta)$ and $\&(\zeta)$ include a implicitly, and sensitivity depends on a. Therefore, $\&(\zeta)$ must be nearly constant for variations of a, that is the variations of ζ, because in this case the second term of Eq. (3.10) becomes zero and the sensitivity $dS(\zeta)/da$ does not depends on ζ. From the definition of $\&(\zeta)$ shown in Eq. (3.11), $\&(\zeta)$ is proportional to $S(\zeta)$ and the functional behavior of $\&(\zeta)$ is the same as $S(\zeta)$. In Fig. 3.1, $\&(\zeta)$ has nearly a constant value in two regions; around the peak near $\zeta = 0.5$ and where the function approaches the asymptotic line. As discussed in subsection 3.1(c), the former region satisfied the near field condition, and

the latter satisfied the far field conditions. Apparently, the sensitivity becomes a maximum in the former region, and the dynamic range becomes widest in the latter region, because the sensitivity is independent over wide range of absorbances a.

In the near field, the ζ value where the maximum of $S(\zeta)$ is given is easily obtained by setting the first derivative of $S(\zeta)$ with respect to ζ equal to zero, and it is approximately

$$\zeta = \frac{\gamma a}{r_0} = \frac{1}{2}, \quad i.e, \quad a = \frac{r_0}{2\gamma}. \tag{3.12}$$

Equation (3.12) gives the design conditions for the most sensitive PA cells. If the sample absorbance is on the same order as the solvent, the value of γ is approximately independent of the sample absorbance as shown in Eq. (3.8). In this case, the cell can be designed as highly sensitive, with the design conditions given by Eqs. (3.12), (3.7) and (3.8) and as follows,

$$a = \frac{r_0}{2}\left(1 + \frac{aI_0 l_s}{\kappa}\left(-\frac{1}{\lambda}\left(\frac{dn}{dt}\right)\right)\right)^{\frac{1}{2}} \tag{3.13a}$$

$$= \frac{r_0}{2}\left(1 + 2.3 I_0 l_s\right)^{1/2}$$

$$= \frac{r_0}{2}\left(1 + 2.3 I_0 \frac{L}{2}\right)^{\frac{1}{2}}, \tag{3.13b}$$

where L is the cell length in cm. The optimal cell radius for the highly sensitive PA cell can be given by the beam radius r_0, beam power I_0, and

cell length L, as shown in Eq. (3.13). On the other hand, in the case when the cell radius is selected as

$$\zeta = \frac{ra}{r_0} > 2, \quad i.e., \quad a > \frac{2r_0}{r}, \tag{3.14}$$

the asymptotic curve in Fig. 3.1 shows that the detection conditions of the PA signal satisfy the far field condition and the sensitivity of the PAS is not significantly affected by the parameters r, r_0 and a. Namely, a stable and wide dynamic range PA cell can be designed with Eq. (3.14).

Both ultra high sensitivity and wide dynamic range have been expected of PAS as a weak absorbance detector, and they have been partially demonstrated in experiments (Oda et al., 1978). Especially in analytical applications such as ultratrace analysis, the sensitivity of PAS must be kept high and constant to ensure linearity of $S(\zeta)$ versus a. The theoretical conclusions shown in Eqs. (3.12) and (3.13) provide basic and significant information about the sensitivity of PAS from the viewpoint of analytical applications. When the value of a is small and does not change widely, for example, in the ultratrace analysis of the next chapter, the background absorption coefficient is on the order of 10^{-4} cm^{-1} and varying 10^{-6} - 10^{-7} cm^{-1} at most, the variation of $dS(\zeta)/da$ is small. This is because the variation of ζ due to such variations of a is estimated as less than 1% using Eq. (3.7), and the change of $S(\zeta)$ in its peak region in Fig. 3.1 is negligible for such a small variation of ζ. In physical terms, the slight change in the beam radius due to the thermal lens effect does not effect the geometrical conditions of the PA signal detection, and the sensitivity is kept constant. In this case, the most sensitive PA cell can be designed with Eq. (3.13).

However, when the sample absorbance changes widely, the change of the beam radius in the sample caused by the thermal lens effect is not negligible, and the sensitivity depends on the sample absorbance, as easily seen in Fig. 3.1 and Eq. (3.10). Therefore, when the sample absorbance changes widely, as in the application of PAS as the detector for liquid chromatography, the cell radius must be designed to satisfy the far field condition for which design criteria are shown in Eq. (3.14). Because the value of $S(\zeta)$ is constant in the far field as shown in Fig. 3.1, and the second term of Eq. (3.10) becomes zero, hence the sensitivity of PAS is kept constant. From this viewpoint, a large size PA cell for which the radius is about 10^0 cm is suitable for analytical applications, because it can easily satisfy the far field condition for a beam radius of 10^0 mm, and maintain constant sensitivity for various liquids samples. However, as PAS becomes more refined, the cell size can be made smaller, for example the cell volume for liquid chromatography is 20 μL and its radius is only a few mm (Oda and Sawada, 1981). In this case when a small PA cell is applied to measure various absorbance samples, countermeasures such as beam focusing with a lens to satisfy the condition of Eq. (3.14) should be employed to ensure constant sensitivity.

Finally it should be pointed out that the present theoretical methods for optimization of PA signal detection can be applied to various types of PA cells by giving a suitable response function $R_s(a)$ of the detectors, Green's function $G_\omega(\mathbf{r}|\mathbf{r}')$ of the cell geometry, beam profile $R(\mathbf{r})$ and beam modulating function $M(t)$. These functions are uniquely given for each cell and PAS system.

3.3 Beam Modulator and Lock-in Amplifier

As shown in Eq. (2.20), the detected PA signal $S(\mathbf{r}, t)$ with the pressure transducer in CW PAS was developed into a Fourier series. It can be written more concretely as follows;

$$S(\mathbf{r}, t) = \sum_{n=-\infty}^{\infty} \mathrm{M}_n^f \, q_n(\mathbf{r}, t) \, R_S(\mathbf{r}) \tag{3.15}$$

$$q_n(\mathbf{r}, t) = \eta\alpha I_0 \left(inw_0 e^{inw_0 t} \int_{\mathbf{r}'} R(\mathbf{r}') \, G_{n\omega_0}(\mathbf{r} \mid \mathbf{r}') \, d\mathbf{r}' \right), \tag{3.16}$$

$$\mathrm{M}_n = \frac{w_0}{2\pi} \int_{-\pi/w_0}^{\pi/w_0} M(t) e^{-inw_0 t} dt. \tag{3.17}$$

where $q_n(\mathbf{r}, t)$ and M_n^f are the n-th Fourier components of $Q(\mathbf{r}, t)$ and its Fourier coefficients, i.e., $M_n^f q_n(\mathbf{r}, t)$ is the n-th harmonic of the PA signal. Phase sensitive detection using a lock-in amplifier detects only the first Fourier component as discussed in section 2.4, hence the contributing term to the CW PAS is the term $n = 1$ in Eq. (3.15). Furthermore, Eqs. (3.15) and (3.16) show that the DC component of the excitation beam corresponding to $n = 0$ does not contribute to the generation of the PA signal. In physical terms, steady heating of the sample by laser irradiation increases the pressure in the heating region, however it does not induce pressure fluctuation which is the origin of the acoustic signal.

From the above discussion, a suitable beam modulation method can be specified. The desired modulator must have a high modulation depth and efficiency, because the DC component of the excitation beam does not contribute to signal generation and the signal magnitude is proportional to the sinusoidal fluctuating component of the total absorbed photoenergy.

Equation (3.17) shows that the shape of the modulation function does not make an important contribution, although sinusoidal modulation is effective for avoiding the generation of harmonics. Thus the most suitable beam modulator to obtain a strong PA signal is a beam chopper of the rotating blade type which has a 100% modulation depth and efficiency. An acousto-optic (AO) modulator can produce various kinds of modulation functions including a sinusoidal function and it can provide high modulation frequencies up to 1 MHz, hence it is suitable to generate mono frequency sinusoidal PA signals or high frequency ones which are needed in some spectroscopical applications introduced later. However, the AO modulator is not always suitable in ultrasensitive PAS systems for trace analysis and weak absorption detection, because its modulation depth and efficiency are not so high and a high modulation frequency is not always necessary in these applications.

From the measured frequency characteristics of the PA signal shown in Fig. 2.7(b), the PA signal magnitude monotonously decreased with increasing modulation frequency and some acoustic, structual and electric resonance peaks appeared in the high frequency region. It is better to obtain a stronger PA signal magnitude for improving the signal-to-noise (S/N) ratio. However, using the modulation frequency near the resonant point should be avoided for stability of PAS systems, because the signal magnitude varies sharply with the change of the modulation frequency around the resonance points. Therefore, chose of modulation frequency is recommended as a relatively low frequency, 10^1 - 10^2 Hz.

The first Fourier component of the detected PA signal which is amplified by the lock-in amplifier was given by Eqs. (2.21) and (2.22) in polar coordinates. The in-phase PA signal of Eq. (2.22) showed that the amplified PA signal S is linear with respect to the generated PA signal magnitude only when the phase of the internal oscillator θ is equal to the

phase of the PA signal ϕ. In the two components of ϕ explained in Eq. (2.23), ϕ_D originates in the energy migration in the thermal process, (e.g. nonradiative relaxation), and ϕ_Q is caused by propagation of the PA signal. In analytical uses, although the value of ϕ_D is negligible because the energy migration time is small in comparison with the beam modulation period, ϕ_Q cannot be ignored, because ϕ_Q is written as

$$\phi_Q = \arg\, q_1(\mathrm{r}, t) = \tan^{-1} \frac{-\mathrm{Im}\{q_1(\mathrm{r}, t)\}}{\mathrm{Re}\{q_1(\mathrm{r}, t)\}}, \tag{3.18}$$

where Im{x} and Re{x} are imaginary and real parts of x, and the value depends on the sample absorbance due to the thermal lens effect on $q_1(\mathrm{r}, t)$ through $R(\mathrm{r})$ as shown in Eq. (3.16). This dependence can be explained in physical terms as follows: When the PA signal is detected at high sensitivity, the detection condition is in the near field condition of Eq. (3.12). In the near field condition, the geometrical profile of the acoustic source term is not neglected as a point source and the waveform strongly depends on the source profile $R(\mathrm{r})$, hence the phase of the PA signal are also dependent on the source profile as shown in Eq. (3.18). It is difficult to obtain ϕ_Q from numerical calculations with Eq. (3.18), hence, it is better to use an autophase lock-in amplifier which has the ability to track the signal phase. With this type of lock-in amplifier, the PA signal is amplified linearly without justifying θ and ϕ.

3.4 Ultrasensitive PAS System

In this section, an ultrasensitive PAS system for colorimetric uses is designed applying the optimization theory, and the design method is successfully proved experimentally, using cobalt 1-nitroso-2-naphthol

chelate xylene solutions. Finally, the minimum detectable absorption coefficient and its relation to the lower determination limit are discussed.

(a) System design and apparatus

The ultrasensitive PA cell is designed using the optimal design conditions represented in Eq. (3.13). The optimal cell radius for use of *m*-xylene as solvent with cobalt 1-nitroso-2-naphthol chelate is calculated as 4.4 mm for the parameters of system A listed in Table 3.2. Therefore a cylindrical PZT with radius 4.5 mm is selected. System A is the present optimized system and system B is an earlier one employed in previous ultratrace determinations of cadmium (Oda, et al., 1978). The longitudinal section of the optimized cell is shown in Fig. 3.6. This cell is the same as that shown in Fig. 3.2, and it was proved to be the most sensitive cell for *m*-xylene in sub-sections 3.1 (b) and (c). This cell is also mounted in a cell holder made of stainless steel to provide electromagnetic and mechanical noise shielding.

The lock-in amplifier used for system A is a two-phase type, and the phase θ is automatically adjusted to the phase of the PA signal ϕ to maintain the linearity between the signal amplitude and the sample absorption coefficient, as was discussed in section 3.3. As also explained there, the beam is modulated by a beam chopper of the rotating blade type, and the modulation is rectangular with a duty cycle of 50%.

The parameters of system B are listed in Table 3.2. This system is not optimized. The cell radius is 5.2 mm, while the optimal cell radius for this system is 2.6 mm, and the phase of the lock-in amplifier is fixed at 4.0 deg which give the maximum output for *m*-xylene.

Equation (2.31) shows that the detected PA signal is proportional to the g value of the piezoelectric constant of the PZT detector, hence the

Table 3.2 Parameters of the PA spectrophotometer systems.

Symbol/Parameters	Values	
	Optimized system (System A)	Earlier system (System B)
Cell		
a Cell Radius	4.5* mm	5.2 mm
L Cell length	100**mm	50 mm
g g Value of the PZT detector	12.0 cmV/dyn	8.0 cmV/dyn
Excitation beam		
I_0 Beam power	1.6** W	1.0 W
r_0 Beam radius	2.0** mm	2.0 mm
λ Wavelength	488** nm	488 nm
f Modulation frequency	181 Hz	181 Hz
Lock-in amplifier		
Phase	Phase of PA signal* (Auto phase)	4.0 deg

* Optimized parameters

** Parameters used for optimization

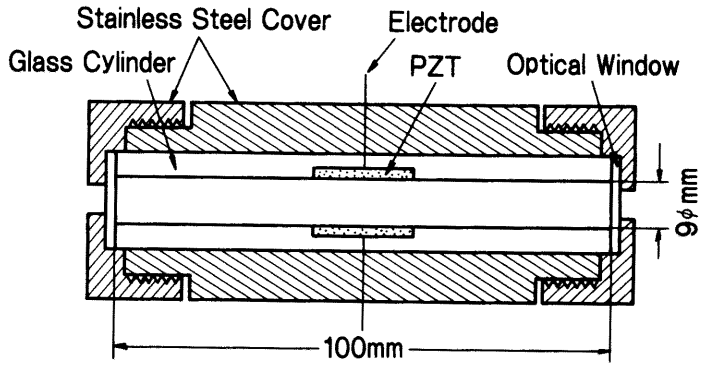

Fig. 3.6 A longitudinal section of an optimized cylindrical photoacoustic cell. The radius is optimized using Eqs. (3.12) and (3.13b) with the parameters listed in Table 3.2. This cell is mounted in a cylindrical cell holder made of stainless steel to provide electromagnetic and mechanical noise shielding. Filling with liquid sample is done by removing the quartz optical window.

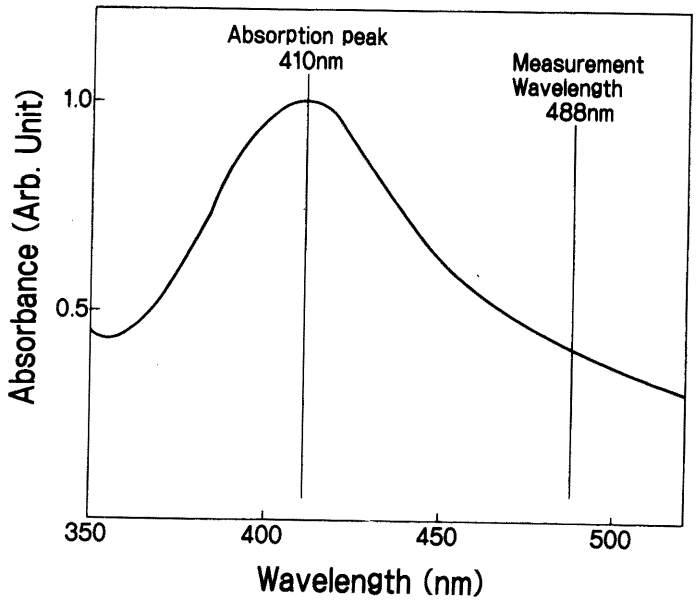

Fig. 3.7 Absorption spectrum of cobalt 1-nitroso-2-naphthol chelate in *m*-xylene obtained with a conventional spectrophotometer: concentration, 10 ppb of cobalt.

sensitivity of the cell is also proportional to the g value as shown in Eqs. (2.32) and (3.10). The sensitivity of the PAS system, of course, is proportional to the beam power as shown in Eq. (3.9). Therefore, improvements of the g value of the detector and the beam power contribute to increased total sensitivity of the PAS system; their contributions are estimated to be factors of 1.5 and 1.6, respectively.

(b) System efficiency test

m-Xylene solutions of cobalt-1-nitroso-2-naphthol (Co-1-nitroso N) chelate are used to obtain calibration curves. This chelate is stable to light and its molar absorptivity value is well known. Furthermore, pure solutions can be easily prepared by the solvent extraction method (Motojima, 1985), making it a suitable standard for calibration curve measurements.

A freshly prepared Co-1-nitroso N *m*-xylene solution (10 ppb of cobalt) is diluted with *m*-xylene, and five samples, 0.2, 0.5, 1.0, 2.0 and 5.0 ppb, are prepared. An absorption spectrum of Co-1-nitroso N obtained with the 10 ppb sample is shown in Fig. 3.7. The absorption peak seen at 410 nm has a molar absorption coefficient of 3.5×10^4 $mol^{-1}cm^{-1}L$. From this absorption spectrum of Co-1-nitroso N, the molar absorption coefficient at 488 nm is then obtained as 1.4×10^4 $mol^{-1}cm^{-1}L$.

The magnitudes of the PA signals for each sample are measured with systems A and B, and these values are plotted in Fig. 3.8. Calibration curves for each system are obtained to confirm the sensitivity improvement by the present optimal design. These calibration curves are obtained with a least squares method.

Photoacoustic signals of *m*-xylene from five bottles having different lot numbers, namely, background absorptions of commercial *m*-xylene, are measured with system A, and these results are shown in Fig. 3.9.

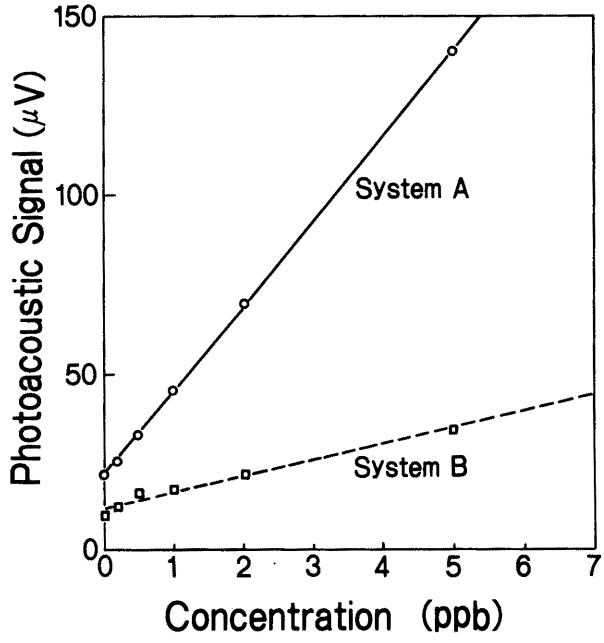

Fig. 3.8 Calibration curves of cobalt 1-nitroso-2-naphthol chelate in *m*-xylene for the PAS system A (solid line) and B (dashed line).

Table 3.3 Parameters of calibration curves.

Apparatus	k (μV/ppb)	σ (μV)	S_b (μV)
System A	23.9	0.46	21.5
System B	4.7	1.00	11.4

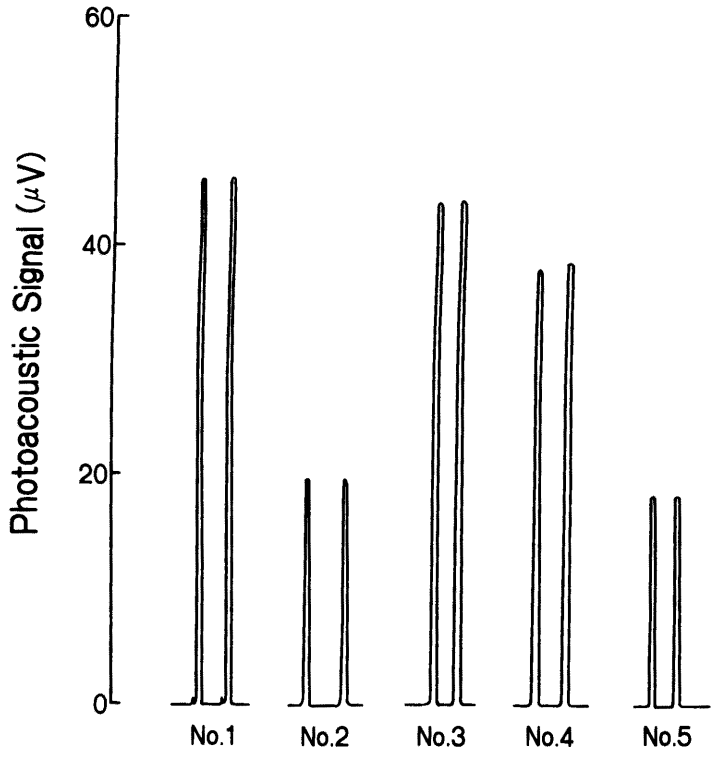

Fig. 3.9 Photoacoustic signal magnitude of *m*-xylene in five bottles of different lot numbers. Measurements are repeated twice for each bottle.

(c) Results and discussion

The performance of the PAS system, such as sensitivity and linearity, is discussed using the parameters of the calibration curves. The calibration curves shown in Fig. 3.8 are represented as

$$S = kC + S_b, \tag{3.19}$$

where C is the concentration of the sample, and S_b is the *m*-xylene blank level, that is, the PA signal of *m*-xylene. The sensitivity of the PAS system is defined as the rate of the PA signal increase for the concentration, and is the proportionality coefficient k in Eq. (3.19). The

linearity of the PAS system has an effect on the scatter of the measured values from the calibration curves, and it is evaluated with the standard deviation σ of the measured values from the calibration curves.

The parameters of the calibration curves shown in Fig. 3.8 are summarized in Table 3.3. The sensitivity of system A is 5.1 times better than that of system B. The increase in g value of the detector and beam power improve the sensitivity by factors of 1.5 and 1.6, respectively, then an improvement factor of 2.1 times is due to the optimal cell design. Sensitivity of the PA cell itself is improved by a factor of 3.2, including the PZT material selection. An increase of absorbance by extending the cell length does not contribute to sensitization of the PA cell, because the radial mode of the PA signal is mainly excited in a cylindrical cell (Chen and Shirk, 1984). Therefore the design method of the PA cell, arising from optimization by Eqs. (3.13a) and (3.13b) and PZT material selection, is confirmed to be effective. From an economical viewpoint, this design method is useful, because the 3.2 factor improvement of sensitivity due to increasing laser power would cost more than rebuilding the PA cells.

The standard deviation σ of the optimized system A is 0.46 relative to system B, as shown in Table 3.3. Matching the phase of the lock-in amplifier with the phase of the PA signals effectively contributes to a decrease in scatter of the measured values. As a result of the sensitivity improvement and the decrease in the standard deviation, the determination limit of Co-1-nitroso N in xylene, defined as $2\sigma/k$, is lowered to 0.038 ppb (system A) from 0.46 ppb (system B). From the obtained value of the molar absorptivity at 488 nm, this means absorption coefficients of 8.7×10^{-6} and 1.1×10^{-4} cm^{-1}, respectively.

Generally, the absorption coefficient α for weak absorption is expressed on the basis of Lambert-Beer law as,

$$\alpha = \varepsilon_m C_m, \tag{3.20}$$

where ε_m is the molar absorptivity and C_m is the molar concentration. Equation (3.20) is valid when the absorption coefficient of the solvent α_b can be neglected. However, the blank levels of the PA signals for *m*-xylene S_b shown in Table 3.3 are not zero, hence PAS is too sensitive for application of Eq. (3.20). Instead, the following relationship is used:

$$\alpha = \alpha_b + \varepsilon_m C_m, \tag{3.21}$$

where α_b is the background absorption coefficient. As a linear relationship between the absorption coefficient and the PA signal magnitude is established in the optical weak absorption region, the following equation holds

$$\alpha_b = \frac{S_b}{S_1 - S_b} \varepsilon_m C_{m,1}, \tag{3.22}$$

where S_1 is the PA signal magnitude for the concentration $C_{m,1}$. The molar absorptivity ε_m at 488 nm is obtained as 1.4×10^4 $mol^{-1}cm^{-1}L$ from Fig. 3.7, and the values of background absorption coefficient $\alpha_{b,A}$ and $\alpha_{b,B}$ for respective PAS systems A and B are calculated with Eq. (3.22) and measured values at 1 ppb as,

$$\alpha_{b,A} = 2.1 \times 10^{-4}\ cm^{-1},$$
$$\alpha_{b,B} = 5.6 \times 10^{-4}\ cm^{-1}.$$

The difference between the values $a_{b,A}$ and $a_{b,B}$ cannot be clearly explained presently. However, it probably originates from the difference between absorption coefficients of the *m*-xylene used for the dilution which has some impurities. This is seen in the variation of PA signal magnitude for five bottles of *m*-xylene from different lots (Fig. 3.9) which scattered widely, although the reproducibility of the measured values for the same bottle is within 1 %. Thus, the background for solvents used in colorimetric analysis with PAS should be checked or the solvents carefully purified.

The noise level of system A is about 4 nV, hence the minimum detectable absorption coefficient of this photoacoustic spectrophotometer (S/N=2) is calculated as 3.8×10^{-8} cm^{-1}. This value is three to four orders of magnitude lower than the detection limit of conventional absorption spectrophotometers. In general, the absorption coefficients of solvents are about three to four orders of magnitude higher than the detection limit as shown in the present work and others (Fang and Swofford, 1983; Patel and Tam, 1981), hence the absolute value of the detection limit of PAS is low enough for analytical applications. From this viewpoint, quality control of solvents, based on measurements of absorption coefficients as shown in Fig. 3.9 may be one of the most important applications of PAS. Futhermore, it must be pointed out that the high sensitivity, linearity and stability are more important than the detection limit for colorimetric analytical applications of PAS, because the determination limit using the calibration curve is defined as $2\sigma/k$, and the detection limit of the PAS equipment has little meaning for high background samples. There are some cases in which background subtraction by a double-beam technique has been effective in improving the lower determination limit (Sawada and Oda, 1981). Details about the lower determination limit

in relation to the background are discussed in the next chapter, along with a sub-ppt (fg/ml) experimental determination.

3.5 Conclusion

Instrumentation of the PAS system was discussed from analyzing $Q(\mathbf{r}, t)$ obtained in Chapter II. First, dependence of the PA signal magnitude on geometrical conditions of a cylindrical direct coupling cell was analyzed, and the theoretical result was experimentally confirmed. In this theoretical and experimental study, the dominant factor which determined the acoustic source profile was clarified to be the thermal lens effect, not thermal diffusion which is the dominant factor in solid and gaseous PAS. From the results of the signal magnitude analysis, the optimal design method for an ultrasensitive and wide dynamic range PA cell was deduced, and appropriate conditions of beam modulation and phase sensitive detection were obtained. With this optimization method, an ultrasensitive PAS system was designed. From the results of the system efficiency test, the sensitivity was improved more than one order in comparison with the ordinary PAS system, and the lower detection limit of the absorption coefficient reached 10^{-8} cm^{-1}, hence the availability of the present design method was verified.

CHAPTER IV ULTRATRACE ANALYSIS

In Chapter III, the optimal design method for an ultrasensitive PAS system was deduced from the basic theory, and the system, having a lower detection limit absorption coefficient on the order of 10^{-8} cm^{-1}, was developed. Now, in this chapter, the developed ultrasensitive PAS is applied to ultratrace determination.

In recent years, water and reagents used in technical fields, such as semiconductor, biochemical, and nuclear engineering fields, are being highly purified, and some kinds of impurities are necessitating ppt (pg/mL) level analyses. For example, the amounts of cobalt that are neutron activated in nuclear power reactor coolant and cause an increase in radiation dose rate around the coolant system have been reduced to extremely low levels and are estimated to be on the order of ppt (Kitamura, et al., 1985). Hence a determination method for ultratrace cobalt is required to clarify the species behavior in the coolant.

Ultrasensitive determinations with PAS near the 10 ppt level were first achieved by Lahman et al. (1977) and Oda et al. (1978). These groups demonstrated determination limits in chloroform of 12 ppt for β-carotene and 14 ppt for cadmium dithizonate, respectively. Voigtman et al. (1981) also achieved similar levels for porphyrin derivatives. In these experiments, the dynamic range of PAS as one kind of colorimetry was shown to be more than three orders of magnitude, and the determination limit was improved by about two orders in comparison with conventional spectrophotometers.

However, the PAS systems used in these experiments, which were performed as relatively early PA determination studies, were not optimized, nor were theoretical discussions on the characteristics of PA

determination including sensitivity, dynamic range and determination limit made. Then, in the first section, the theory of PA determination is developed based on the general theory in Chapter II, and the characteristics of PA determination are investigated (Kitamori et al., 1986c). Special consideration is given to the background due to solvent, and it is shown that the determination limit closely reaches the basical limitation of colorimetric analysis. The system stability is seen to be one of the most dominating factors for PA determination limits. Following the theoretical section, sub-ppt amounts of cobalt in aqueous solutions are determined using the ultrasensitive system and solvent extraction (Kitamori et al., 1986a). Suitable analytical conditions including background reduction and stabilization of the extracted phase are examined experimentally, and good ultratrace PA determinations at sub-ppt levels are confirmed.

4.1 Theory of PA Determination

In Chapter III, the PA signal which was generated in a cylindrical direct coupling cell and measured with CW PAS was analyzed on the basis of the assumption that the thermal energy was linearly converted from optical energy in the thermal process, and the linear relationship between the signal magnitude and absorption coefficient was quasi-qualitatively obtained as shown in Eq. (2.24) for a weak absorption sample. This linearity of the PA signal magnitude for the absorption coefficient was proved in section 3.4 where the efficiency of the ultrasensitive PAS system was examined using cobalt 1-nitroso-2-naphthol chelate.

First, in this section, the linear conversion from optical energy to thermal energy in the thermal process and the linear relationship between

the PA signal magnitude and absorption coefficient are rigorously derived from the basic theory developed in Chapter II. Then, the characteristics of PA determination are discussed.

(a) Basis of colorimetry with PAS

As mentioned in section 3.4, the beam modulation frequency is usually set at 10^1 - 10^2 Hz in analytical applications from the viewpoints of sensitivity and system stability to modulation frequency. At these beam modulation frequencies, the modulation periods are sufficiently longer than the nonradiative relaxation times, hence the impulse response $D(t)$ in the thermal process is expressed by a δ-function. The thermal energy converted from optical energy is the product of absorbed optical energy and quantum yield of nonradiative relaxation. Therefore, the impulse response of the thermal process $D(t)$ becomes

$$D(t) = \eta_N I_0 (1 - e^{-a}) \delta(t) \tag{4.1}$$

where η_N is the quantum yield of nonradiative relaxation. Thermal energy, giving the source term of $H(\mathrm{r}, t)$ in Eqs. (2.1) and (2.2), is defined as the heat quantity per unit volume and unit time. Hence, Eq. (4.1) means the absorbed optical energy by unit length, because the PA signal generation and detection in a cylindrical PA cell are analyzed using cylindrical coordinates and the axially symmetric model shown in Fig. 2.4. The Fourier image of Eq. (4.1) is obtained as

$$D^f(w_0) = \eta_N I_0 (1 - e^{-a}), \tag{4.2}$$

and is developed for small α as

$$D^f(w_0) = \alpha \eta_N I_0 \tag{4.3}$$

Therefore, the in-phase PA signal magnitude ($\theta = \phi$) in CW PAS is obtained from Eqs. (4.3) and (2.22b) as follows

$$S = \eta \eta_N \alpha I_0 M_1^f |Q^f(r, w_0)| R_s(r). \tag{4.4}$$

Equation (4.4) shows that the linear relationship between the magnitude of the detected PA signal S and the absorption coefficient α holds in CW PAS system, while many energy conversion processes from optical energy to electric energy are included in the generation process of the PA signal. Furthermore, from Eqs. (2.19) and (4.3), it is ensured that the detected PA signal with any PAS systems is proportional to α.

Equation (4.4) lays the basis for colorimetry with PAS. In the following subsections, the characteristics of PA determination are investigated based on this basis.

(b) Sensitivity

Sensitivity characteristics of the PAS system have already been discussed in section 3.2. In this sub-section, the sensitivity characteristics which are related to the PA determination are considered.

In the same manner as section 3.2, the sensitivity of PAS is defined as the slope of the calibration curves, and it is obtained from Eq. (4.4) as follows,

$$\frac{d}{da}S=\eta\eta_N I_0 M_1^f|Q^f(\mathbf{r},\ w_0)|R_s(\mathbf{r}). \tag{4.5}$$

This equation shows that the sensitivity depends on the cell geometry and material $Q^f(\mathbf{r}, \omega_0)$, detector response $R_s(\mathbf{r})$, beam modulation M^f_1, beam power I_0, quantum yield of nonradiative relaxation η_N, and thermal property of the solvent η. The first four factors are sensitivity factors related to the PAS system, and their specifics have already been dealt with in sections 3.2 and 3.3. Here, it is noted that the sensitivity is proportional to the beam power I_0, because the magnitude of the PA signal is proportional to the absorbed optical energy. Hence, the sensitivity of PAS can be remarkably improved by using a high intensity beam source such as lasers, although increased beam power is not effective for sensitivity improvement of ordinary absorption spectrophotometers which measure the ratio of incident beam intensity to the transmitted one.

The inherent sensitivity characteristics of PA determination are the factors related to the sample material properties. The quantum yield of the nonradiative process η_N usually has a large value for many substances, while even fluorescent substances have over a 0.9 value of η_N in lots of cases. Hence the PA determination can be applied to many samples. Additionally, the sensitivity of the PA determination depends on the thermal property of the solvent η. The coefficient η is the ratio of isothermal bulk modulus β to the specific heat C_p as shown in Eq. (2.9). This term expresses the spatial expansion ratio for added thermal energy; i.e., it may be interpreted as one of the energy conversion ratios of the solvent from thermal energy to mechanical energy of the PA signal. In many cases, the solvents used in colorimetry are selected from the viewpoints of analytical chemistry techniques such as extraction, procedures and handling of reagents. However, considering Eq. (4.5), it

is desirable to select the solvent for which β is large and C_p is small. It has been reported that chloroform provides six times greater sensitivity than does water (Sawada et al., 1978).

(c) Dynamic range

The premise of the linear relationship between the PA signal S and absorption coefficient α in Eq. (4.4) is that the following approximation of the Lambert-Beer law in the weak absorption, which is introduced in Eq. (4.3), is valid:

$$\Delta I=(1-e^{-\alpha})I_0=\alpha I_0, \tag{4.6}$$

where ΔI is the absorbed optical energy. Therefore, colorimetric determination with PAS is applicable only to weak absorption samples. In addition to this limitation due to optical saturation, as discussed in sections 3.1 and 3.2 the thermal lens effect which changes the acoustic source profile is another factor that may cause nonlinearity of the PA signal magnitude to the absorption coefficient in strong absorption region.

Using a measurement precision with three significant figures, the approximation of Eq. (4.6) is valid for the region of absorption coefficients less than or equal to 10^{-3} cm^{-1}. As shown in section 3.4, the lower detection limit absorption coefficient of the ultrasensitive PAS system reaches 10^{-8} cm^{-1}, and hence, the dynamic range of the PA determination is about six orders of magnitudes. Therefore, PA determination is an effective analytical method for ultratrace substances.

(d) Detection and determination limits

When the ultrasensitive PAS system is applied to colorimetric determination, the lower detection limit of the equipment and the determination limit of the solutes must be clearly distinguished, because the lower detection limit absorption coefficient of the PAS system which is defined as double the S/N ratio is several orders of magnitude smaller than the absorption coefficient of the solvents. The absorption coefficient of the solvent cannot be ignored in an ultrasensitive PA measurement, and the absorption coefficient of the solution is obtained as the sum of the absorption coefficients of the solvent and the solute which is given by the Lambert-Beer law, as shown in Eq. (3.21). Hence the PA signal magnitude of the solution is described with Eqs. (4.4) and (3.21), and as follows

$$S=\eta\eta_N(\varepsilon_m C_m+\alpha_b)I_0 M_1^f|Q^f(r,\ w_0)|R_s(r)$$

$$=K\varepsilon_m C_m+K\alpha_b, \tag{4.7}$$

$$K=\eta\eta_N I_0 M_1^f|Q^f(r,\ w_0)|R_s(r) \tag{4.8}$$

where K represents the sensitivity. The second term of Eq. (4.7) stands for the background signal due to the absorption of the solvent, hence the slope of the calibration curve k and the background S_b in Eq. (3.19) are obtained as

$$k=K\varepsilon_m, \tag{4.9}$$

$$S_b = K a_b \tag{4.10}$$

For example, as shown in Table 3.3, the background signal S_b of *m*-xylene used in the efficiency test performed in section 3.4 is 21.5 μV for the optimized PAS system, and the absorption coefficient a_b of *m*-xylene is obtained as 2.1×10^{-4} cm^{-1}. On the other hand, the noise level of the PAS system is 4 nV, which corresponds to an absorption coefficient of 1.9×10^{-8} cm^{-1}. Therefore, in the ultratrace region close to the determination limit, a slight change in the PA signal magnitude due to the absorption of the solute $\varepsilon_m C_m$ is not easily identified from the background absorption of the solvent a_b, and the determination limit is dominated by this background absorption.

In an ideal case where the standard deviation of the measurement values due to handling in the analytical procedures (e.g. solvent extraction) can be disregarded, and the distinguishable signal change ΔS due to the change in solute concentration from the background signal S_b is at most

$$\Delta S = S_b 10^{-(n-1)}, \tag{4.11}$$

where n is the number of significant figures of the PA measurements, but not that of the total PA determination including the chemical procedure. Hence a significant distinguishable change in the absorption coefficient $\Delta a = \Delta \varepsilon_m C_m$, is obtained by substituting Eqs. (4.7) and (4.10) into Eq. (4.11), and is,

$$\Delta a = \Delta \varepsilon_m C_m = a_b 10^{-(n-1)}. \tag{4.12}$$

The relationships in Eqs. (4.11) and (4.12) mean that the distinguishable changes in the PA signal and absorption coefficient are $10^{-(n-1)}$ of the background at most. For example, the distinguishable change in PA signal magnitude in the experiment of section 3.4 is 0.2 μV for the optimized PAS system A, because the background signal S_b is 21.5 μV and the number of significant figures of the measurement is three as shown in Table 3.3. From Eq. (4.12), the lower determination limit C_{det} can be estimated for the ideal case as,

$$C_{det}=\Delta C_m=\frac{a_b}{\varepsilon_m}10^{-(n-1)}. \tag{4.13}$$

As shown in Eq. (4.13), the main factor which dominates the determination limit is the absorption coefficient of the solvent itself, and it is no exaggeration to say that PA determination reaches the basic limitation of colorimetric analysis. In many practical determinations, the standard deviation σ of the measured value, which is due to the solvent purity and chemical techniques, exceeds the minimum distinguishable change in PAS systems as shown in Eqs. (4.11) and (4.12). In these cases, the lower determination limit should be defined by 2σ, as is generally done in analytical chemistry.

From the above discussion, the lower determination limit can be improved by reduction of the background due to the solvent or extracted phase. Hence, investigation of background reduction and stabilization by such measures as washing the extracted phase become decisive factors in achieving ultratrace analysis. In some cases, a double-beam method is considered to be a effective means of improving the determination limit by reducing the background level (Sawada and Oda, 1981). The stability of

the PAS system helps to obtain a constant background level, reducing the standard deviation of the measurement values. From this viewpoint, CW PAS is superior to pulse PAS because of beam power stability.

In the next section, ultratrace determination of cobalt using CW PAS is shown which demonstrates a background reduction by considering analytical conditions, such as washing of the extracted phase.

4.2 Determination of Sub-ppt Amounts of Cobalt

Ultratrace determination of sub-ppt amounts of cobalt in aqueous solution is demonstrated using solvent extraction and PA measurement, and the propriety of the theoretical considerations on PA determination made earlier is verified.

As mentioned before, the potential for PA determinations of ultratrace substances in the 10 - 20 ppt range has been demonstrated (Lahman et al., 1977; Oda et al., 1978). However, those measurements were done using a series of solutions prepared not by extraction, but by stepwise dilution. However, generally, solvent extraction is included in procedures for colorimetric determination, and various trace impurities, such as unreacted reagents, remain in the extracted phase. In some cases, these trace impurities cause a high background level in ultrasensitive measurements with PAS, and they are considered to obstruct the determination at ppt levels. Thus, ultratrace determinations using extraction and PAS measurements have not been done yet.

In the present section, cobalt in aqueous solution is extracted in *m*-xylene as chelate with nitroso-naphthol (nitroso-N). This reagent is

known to be specific for cobalt (Boyland, 1946; Almond, 1953; Needleman, 1966), and the chelate is not destroyed by concentrated hydrochloric acid or sodium hydroxide solutions (Motojima, 1985). Therefore, coexistent metals and excess reagent can be removed by washing the *m*-xylene phase with concentrated hydrochloric acid and sodium hydroxide solutions. Suitable washing conditions to reduce the background are proposed experimentally, and determination of sub-ppt levels of cobalt in water is shown. The effects of coexistent metals and structural isomerism of the reagent are also discussed.

(a) Estimation of lower determination limit

Absorption spectra of cobalt 1- and 2-nitroso-N chelates in *m*-xylene, obtained with a spectrophotometer, are shown in Fig. 4.1. While the chelates have absorption peaks in the spectral region from 308 nm to 410 nm, a 488 nm lasing line is chosen in the present experiments, because the sensitivity of PAS is proportional to the beam power, and the beam power at this line is several orders higher than that of other lasing lines nearer the absorption peaks. Furthermore, both chelates have about the same molar absorptivity at 488 nm, and this value is 1.4×10^4 $mol^{-1}cm^{-1}L$.

The absorption coefficient of *m*-xylene was measured as 2.1×10^{-4} cm^{-1} in section 3.4, and the three significant figures of the PA measurement are used. Hence, from Eq. (4.13), the lower determination limit of both cobalt nitroso-N chelates in *m*-xylene is estimated to be 1.7×10^{-10} mol/L, which is converted into a cobalt concentration of 1.0×10^{-11} g/mL. Therefore, when cobalt in an aqueous solution of 1 L is extracted into the 10 mL of *m*-xylene, 0.1 ppt levels of cobalt can be expected to be determined using PAS.

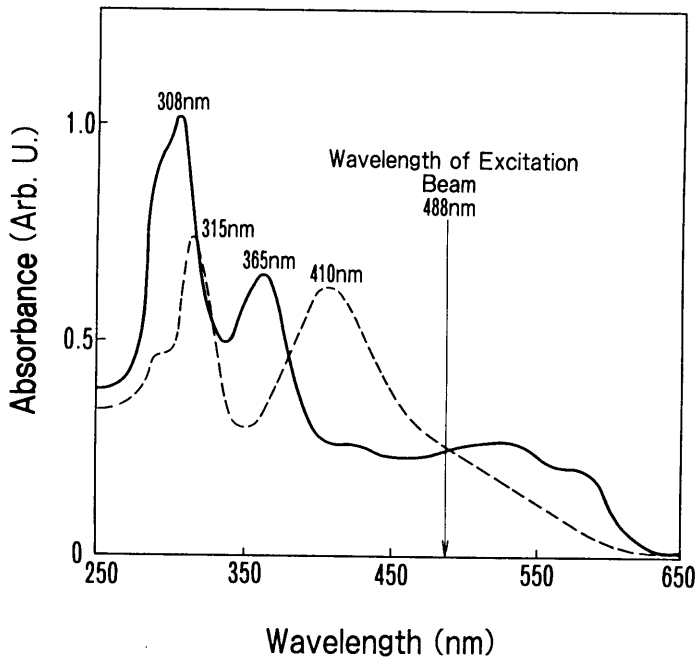

Fig. 4.1 Absorption spectra of cobalt chelates in *m*-xylene. The concentration of both chelate solutions is 1 ppm. The solid line indicates the spectrum of the chelate with 2-nitroso-1- naphthol, and the dashed line shows the spectrum of the chelate with 1-nitroso-2-naphthol.

(b) Apparatus and reagents

The apparatus used in the present experiments is the optimized PAS system developed in section 3.4, and the block diagram and the cell structure were shown in Figs. 3.3 and 3.6, respectively. The parameters of the PAS system were listed in Table 3.2 as being the optimized system.

All reagents are ultrapure grade or spectral grade. Water is subjected to the following ultrapurification measures: distillation in a glass apparatus, two demineralizations with a resin ion exchanger, and filteration with an activated carbon filter and a membrane filter. It should be noted that water distilled in a stainless steel apparatus contains 10^1 - 10^2 ppt of cobalt. The resistivity of the obtained water

is about 18 MΩ/cm, and particulate impurities above 0.2 μm are completely removed.

2-Nitroso-1-naphthol (2-nitroso-N) is purified by recrystallization from benzene, and a sodium hydroxide solution of the reagent is obtained with the following procedure. A 2.5 g sample of recrystallized 2-nitroso-N is dissolved in 250 mL of *m*-xylene by heating at about 100 °C. The solution is filtered through a paper filter, and the eluent is transferred to a separatory funnel containing 500 mL of 0.2 M sodium hydroxide solution. The reagent is extracted into the aqueous phase by shaking for about 3 min, and the 2-nitroso-N sodium hydroxide solution is drawn off. Similarly, a sodium hydroxide solution of 1-nitroso-2-naphthol (1-nitroso-N) is also obtained.

Reference cobalt aqueous solution containing 1.0 ng/mL of cobalt is prepared by stepwise dilution of the stock solution, for which concentration is 1.0 mg/mL. The stock solution is made by dissolving pure cobalt metal (99.99%) in hydrochloric acid. The reference cobalt solution is kept acidic with 0.05 M hydrochloric acid.

(c) Analytical procedure

Trace amounts of cobalt at the ppt level are extracted in 10 mL *m*-xylene as a nitroso-N chelate by the following procedure. A 1 L portion of cobalt aqueous solution is placed in a separatory funnel. Then 1 mL of 2 M citric acid solution, for masking, and 2 mL of nitroso-N solution are added. The pH is adjusted to within 4 - 5 by adding 2 mL of 2 M sodium acetate solution. Then exactly 10 mL of *m*-xylene are added by pipette. After shaking the funnel for 30 minutes with a mechanical shaker, the mixture is allowed to stand for 20 minutes, after which the aqueous phase is drawn off and discarded.

The *m*-xylene phase is washed by shaking in the separatory funnel with concentrated hydrochloric acid, 0.2 M sodium hydroxide and water, to remove the metal impulities and excess nitroso-N, respectively. The washing conditions are detailed below.

The *m*-xylene phase is collected in an Erlenmeyer flask by filteration after dehydration with 3 g of anhydrous sodium sulfate. The same procedure is carried out for the blank solution.

The PA signal magnitude for each sample is measured. Calibration curves are obtained by the least squares method.

(d) Results and discussion (1): Analytical conditions for background reduction

Nitroso-N chelates with metals other than cobalt are readily destroyed by concentrated hydrochloric acid, and the destroyed chelates can be extracted in the concentrated hydrochloric acid phase. As PAS is ultrasensitive, remaining chelates with other metals produce a background and obstruct the exact determination of trace cobalt, hence complete washing of the *m*-xylene phase with concentrated hydrochloric acid is required. First, the background PA signal is measured for the *m*-xylene phase extracted with 2-nitroso-N from a blank solution while changing the amount of concentrated hydrochloric acid used for washing from 5 to 25 mL. The results are plotted in Fig. 4.2. The background decreases on increasing the amount of concentrated hydrochloric acid, and reaches a nearly constant value at more than 15 mL. The background also depends on the number of washings, and becomes constant after more than 3 washes as shown in Fig. 4.3. Therefore, suitable washing conditions for concentrated hydrochloric acid are three 15 mL portions.

Unreacted 2-nitroso-N in the *m*-xylene phase also causes a background increase. The excess reagents are removed by 0.2 M sodium hydroxide

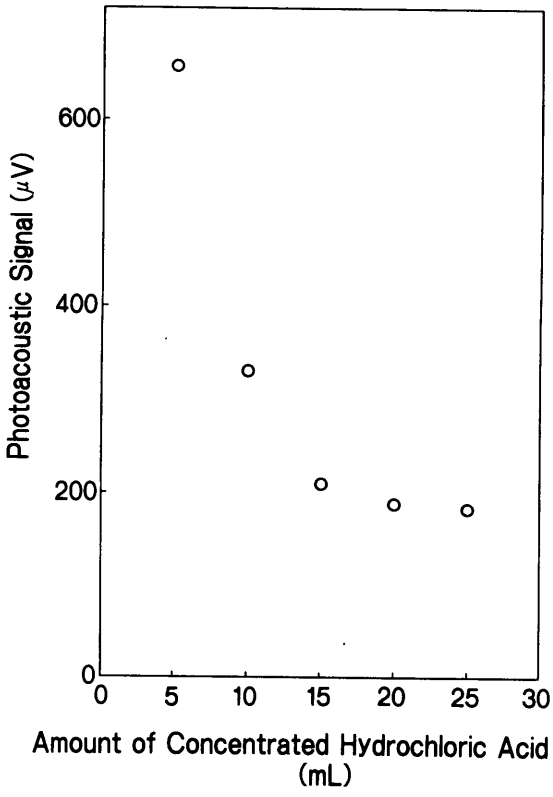

Fig. 4.2
Dependence of background level on the amount of concentrated hydrochloric acid used for washing the *m*-xylene phase. The amounts of cobalt-free water and *m*-xylene are 1 L and 10 mL, respectively, for two acidic washings.

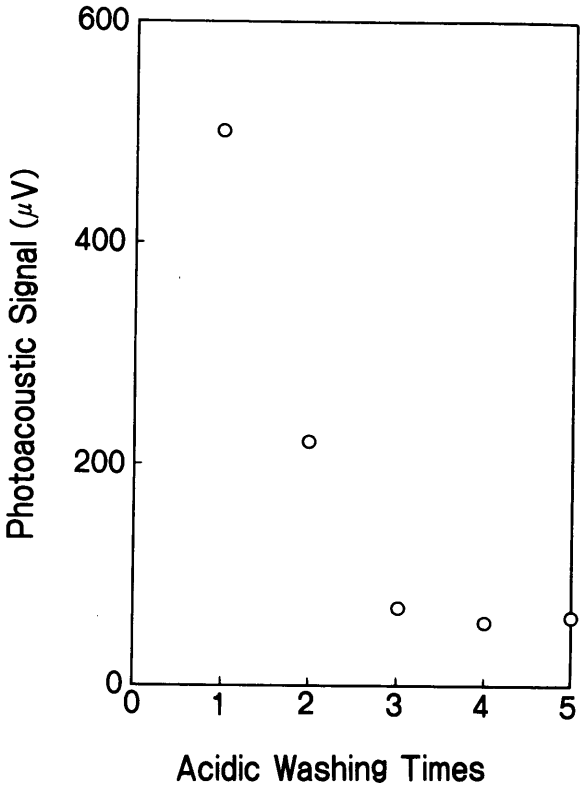

Fig. 4.3
Dependence of background level on the washing times of the *m*-xylene phase with concentrated hydrochloric acid. The amounts of cobalt-free water and concentrated hydrochloric acid are 1 L and 15 mL, respectively.

solution, and suitable washing conditions are obtained by the same procedure which determined the acidic washing conditions. Four 50 mL portions of the sodium hydroxide solutions are adequate.

As the remaining trace quantity of excess 2-nitroso-N reagent is proportional to the added quantity of the reagent, the background is also proportional to this added quantity as shown in Fig. 4.4. Hence the reagent quantity should be minimized. However, as is also shown in Fig. 4.4, quantitative extraction of 100 ng cobalt in 1 L of aqueous solution is obtained by the addition of more than 2 mL of 0.5 % 2-nitroso-N 0.2 M sodium hydroxide solution. Therefore, the optimum quantity of the reagent is 2 mL.

With these obtained conditions, the background is the lowest, and the value is about 75 μV for 1 - 100 ng cobalt extraction with the present analytical procedure. When the quantity of reagent exceeds 2 mL and the acidic and alkaline washings are insufficient in comparison with the present optimized conditions, the background varies on the order of 10^1 - 10^2 μV due to the residual impurities.

(e) Results and discussion (2): Determination limit

Ultratrace amounts of cobalt of 1, 2, 5 and 10 ng in 1 L of water are extracted in 10 mL of *m*-xylene with 2-nitroso-N, and PA signal magnitude for each *m*-xylene phase is measured. The results obtained are plotted in Fig. 4.5. This magnitude is proportional to the cobalt concentration, and the determination limit of cobalt in aqueous solution is calculated on the basis of twice the standard deviation of the measured values. This value is 0.64 ng/L, or 0.64 ppt and is at least three orders lower than conventional colorimetric analyses using spectrophotometers. In the present experiment, the standard deviation 0.32 ppt exceeds the theoretical estimation of the lower determination limit, 0.10 ppt, deduced

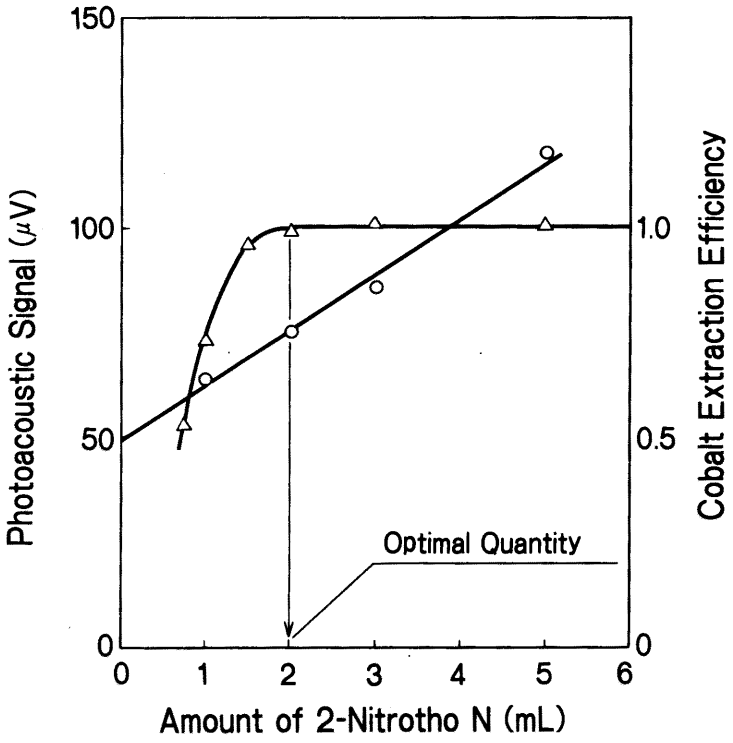

Fig. 4.4
Dependence of background level and cobalt extraction efficiency on the amount of 2-nitroso N reagent. The amounts of the cobalt aqueous solution and *m*-xylene are 1L and 10 mL, respectively, for two acidic and four alkaline washings.

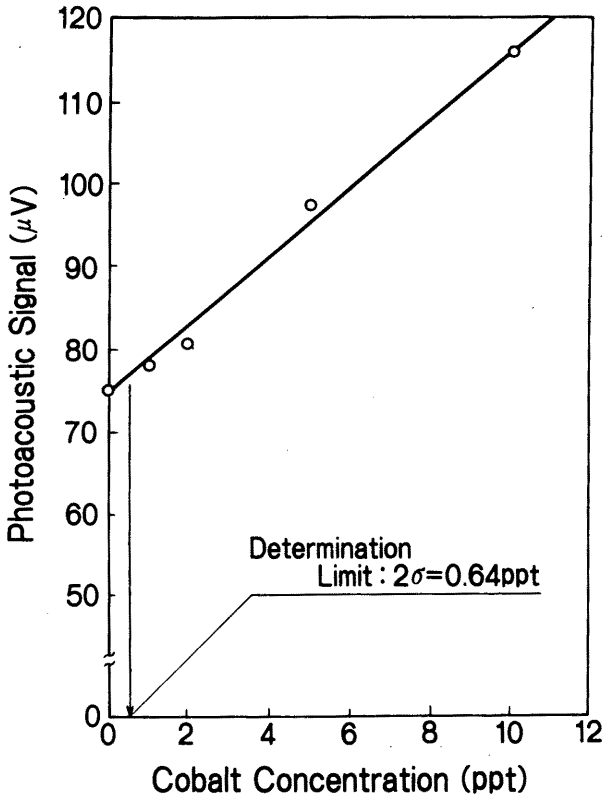

Fig. 4.5
Calibration curve of ultratrace cobalt.

from Eq. (4.13). Hence the lower determination limit is obtained as 2σ. As the experimental result is close to the theoretical estimation, the propriety of the theory for PA determination, developed in the former section, is verified.

The sensitivity of this analytical method, that is the slope of the calibration curve, is 3.80 μV/ppt. Hence a change in PA signals at the 10^{-1} - 10^{0} μV order for the determination of 10^{-1} ppt levels of cobalt would not be identified, if the background varies on the 10^{1} - 10^{2} μV order. Therefore, it is noted that careful washing of the extracted phase to obtain a sufficiently constant and low background is a prerequisite for ultrasensitive analysis with PAS.

Furthermore, the effect of excessive amounts of foreign metals, iron, nickel, chromium and copper is investigated. Except for copper, these heavy metals are constituents of stainless steel, as is cobalt. Copper has a strong chelate forming property. Each of these heavy metals (1 mg) is added to 5, 10, 15, 20 ng cobalt solutions and the blank. Four calibration curves with coexisting metals are obtained with the present analytical method, and plotted in Fig. 4.6. The parameters of the calibration curves, slope and blank level, are listed in Table 4.1. As the slope variation is within 1.3 %, no significant interference from these heavy metals at amounts 10^{5} times those of cobalt can be found. The shift of the blank level originated in the cobalt impurity included in these heavy metals, and the amounts are 11.5, 13.9, 15.1 and 24.9 ppm for iron, nickel, chromium and copper, respectively. These values are easily confirmed by atomic absorption spectrometry.

Using results of ten extractions of cobalt at 5 ppt, precision of the present analytical procedure is calculated to be within 2.8 %. Furthermore, although it is hard to obtain an exact loss of cobalt after extraction at ppt levels of concentration, no significant differences can

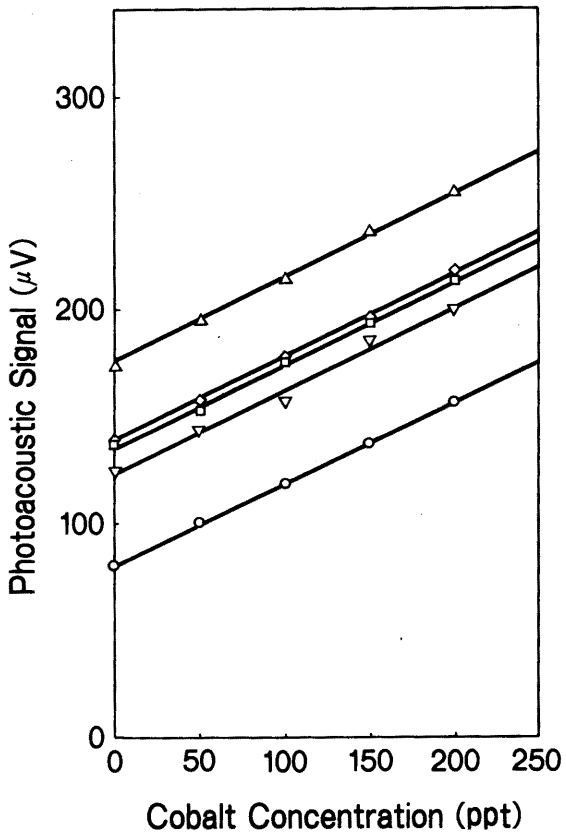

Fig. 4.6
Calibration curves of ultratrace cobalt with foreign metals: iron (▽); nickel (□); chromium (◇); copper (△); and none (○). The amount of each foreign metal is 1 ppm, 10^5 times that of cobalt.

Table 4.1. Parameters of the calibration curves.

Sample	Foreign metal	Slope (μV/ng Co)	Blank level (μV)
No. 1	-	3.75	74.8
No. 2	Iron	3.85	118.0
No. 3	Nickel	3.87	126.9
No. 4	Chromium	3.80	131.3
No. 5	Copper	3.88	168.0

be found between the slopes of the calibration curves obtained by dilution and extraction within the variation of 1.3 % for the chelate concentration range of 5 - 20 ng/(10 mL *m*-xylene), that is, 5 - 20 ppt of cobalt in aqueous solutions. Hence, loss of cobalt in the extraction procedure is negligible, being within the precision of the present analytical procedure. This seems to be due to the high stability of the cobalt chelate in *m*-xylene, although the washing procedure involves eleven steps.

Nearly the same results are obtained with 1-nitroso-N. However, pure 1-nitroso-N is difficult to obtain, and it is less stable in comparison with 2-nitroso-N. For example, using 1-nitroso-N prepared several weeks before, sometimes the *m*-xylene phases that extracted ppt levels of cobalt are colored red, although the absorption coefficients of the *m*-xylene phases for this cobalt concentration range (typically 10^{-4} cm^{-1}) should appear as colorless. Consequently, the determination of ultratrace cobalt is impossible due to the background increment and fluctuation on the 10^2 - 10^3 μV order. This instability of 1-nitroso-N is not considered further in the present study; as 2-nitroso-N does not show such instability, it is recommended for this cobalt determination method.

Ultrasensitive determination with PAS is applicable to various kinds of liquid samples. However, when PAS is combined with an extraction technique, the background due to impurities, excess reagents and instability of reagents should be low and constant, as shown in this section. When a suitable extraction method, which can reduce the background is applied, various materials should be determined at sub-ppt to ppt levels using PAS.

4.3 Conclusion

The ultrasensitivity of PAS developed in Chapter III was applied to ultratrace PA determination. First, the theory of PA determination was developed on the basis of the general theory. The characteristics of sensitivity, dynamic range, and determination limit were clarified theoretically, and it was shown that the determination limit closely reached the basic limits of colorimetric determinations, which are dominated by solvent absorbancy. In the experimental verification of the ultratrace PA determination theory, cobalt in aqueous solution was extracted into *m*-xylene solvent using nitroso-naphthol reagent, and sub-ppt level determinations were demonstrated. Coexistent metals and excessive reagents were completely eliminated by acidic and alkaline washings of the *m*-xylene phase, and the background level became constant and low enough for ultrasensitive PA determination. Concentrations of foreign heavy metals, such as iron, nickel, chromium and copper, 10^5 times more than cobalt caused no interference. The importance of background reduction and stabilization was pointed out for this ultrasensitive colorimetric determination.

CHAPTER V CHARACTERIZATION OF TURBID SOLUTIONS

Analyses of turbid solutions are required in various fields, such as for quality control of solvents used in semiconductor production and biotechnology, analysis of polymers or colloidal components in biochemistry and medicine, analysis of blood corpuscles or particulate components in medical analysis, and characterization of microparticles in engineering areas like ceramics. Quantitative measurements of turbid solutions have been carried out with a turbidimeter, which is based on the attenuation of a transmitted beam by light scattering of the particulate components. But analytical and spectroscopic information, based on the absorption, are not obtained by turbidimetry, which provides imprecise data affected by light scattering factors of the particles such as particle size, complex refractive index, and wavelength. Therefore, a spectroscopic method which can be applied to turbid solutions has been desired in various fields.

In the former three chapters, the theory of PAS and its applications were applied to true solutions. However, as the PA signal is based on the absorption of optical energy by samples, PAS can be applied to obtain spectroscopic and analytical information on turbid solutions as well as true solutions, without being seriously affected by light scattering. Oda et al. (1980) first applied CW PAS to determination of trace barium sulfate in water, and got a determination limit of 30 ppb which was at least two orders lower than that of conventional turbidimetry. For colored turbid substances such as colloidal tellurium the determination limit was 2.5 ppb (Nomura, et al., 1982). This result was three orders lower than that of turbidimetry for which the determination limit was not improved for colored sample. Oda et al. (1980) showed that the

sensitivity did not depend on the particle size distribution in the samples, although this result does not seem to apply in general; a strong sensitivity dependency for particle sizes which are close to the excitation wavelength is shown in Chapter VI. Thus, PAS was demonstrated to be a effective and precise measurement method for turbid solutions.

The theory of PA measurements of turbid solutions has not been established, nor have the physical meanings of high sensitivity and independency of sensitivity on particle size been clarified. Then, in this section the general theory developed in Chapter II is applied to turbid solutions, and the characteristics of PA signals from microparticles in liquids are analyzed (Kitamori et al., 1985b, 1985c). The physical meanings of the PA determination properties of turbid solutions are then clarified.

In addition to this, PAS can obtain information related to energy migration in the thermal process as discussed in Chapter II. The phase shift of PA signals due to thermal energy migration from microparticles to the medium is also analyzed theoretically, and a novel application of PAS to size measurement and thermal characterization for turbid particles is proposed and verified experimentally (Kitamori et al., 1985c, 1986b).

5.1 Theoretical Analysis of PA Signals from Microparticles in Liquids

Photoacoustic signals from a solid in a gas coupled microphone cell have been well described using pressure fluctuation of the coupling medium caused by variation of the temperature field and thermal expansion of the sample (Rosenswaig, 1973a; McDonald and Wetsel, 1978). The phase of the PA signal caused by the propagation of the thermal wave has also been well studied (Mandelis et al., 1979; Adams and Kirkbright, 1977; Quimby and

Yen, 1980). Especially, Monchalin et al. (1984) have analyzed the PA signal from powdered samples and discussed the effect of thermal diffusion and infrared radiation on the signal. However, these theoretical approaches based on the gas coupled microphone cell are not applicable to PA signals in liquid where the thermal diffusion length is negligible in comparison with that in coupling gas.

In the theory for PAS of liquid samples developed in section 2.4, the phase of the PA signal was caused by two processes: impulse response $D(t)$ of energy migration in thermal process, and by generation and propagation of PA signal in the acoustic process. These two components of the phase could be clearly separated as shown in Eq. (2.23). Therefore the PA signal from microparticles in liquid, which is affected by thermal energy migration from the particles to medium can be obtained by analyzing the impulse response $D(t)$ of the microparticles. In this section, the impulse response $D(t)$, which is properly obtained from analysis of the new problem of the wave equation of thermally forced motion (Kitamori et al. 1985b, 1985c), is obtained formally from the general solution described in Chapter II. On the basis of the analysis of $D(t)$, the phase of the PA signal is shown to reflect the thermal energy migration, and the relationships between the phase and the thermal and geometrical properties of the microparticles are obtained.

(a) Analytical model

The coordinate system of the model is shown in Fig. 5.1. This schematic is a cross-section of the cylindrical PA cell developed in Chapters III and IV. The particle located in the r coordinates set on the cell has the spherical ρ coordinates set. The PA signal from the turbid particles is considered to be generated by the following process: turbid particles absorb the optical energy of the excitation beam; the

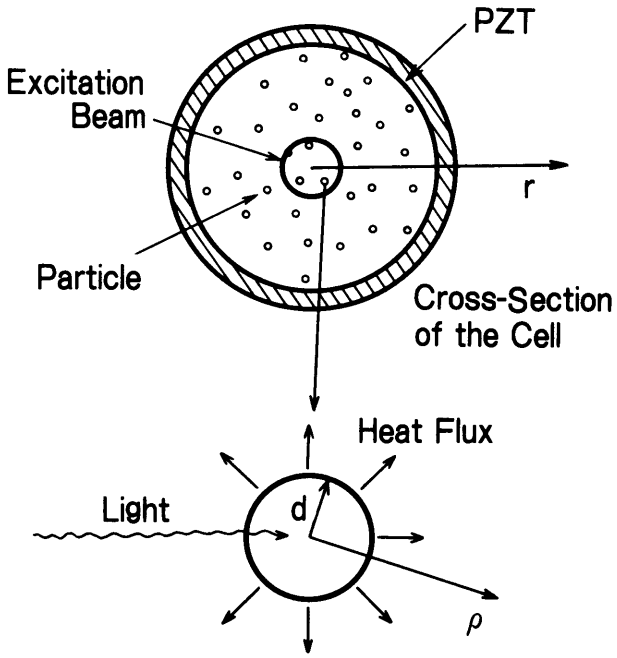

Fig. 5.1 The coordinate system of the model. This schematic is a cross section of a typical cylindrical photoacostic cell for liquid samples. The generated PA signals are detected by the cylindrical PZT. The r cordinates are set for the cell system, and the spherical ρ cordinates are set for the particles located at r.

temperature of the particles rises with the heat caused by nonradiative relaxation of the particle components; heat contained in the particles is released from them to the medium along the temperature field; the medium around the particles is expanded by the heat and an acoustic wave is induced by the repetition of these processes synchronized to the beam modulation. The first three steps of the signal generation process are included in the thermal process, and the last step is in the acoustic process. Therefore, the impulse response $D(t)$ is obtained from the analysis of the first three steps.

When the medium does not absorb the excitation beam or absorbs it only weakly, the temperature distribution in the particle located at r and the surrounding medium $T(\rho, t)$ is given by the following thermal equations

$$(\nabla_{\rho}^{2} - \frac{1}{D_{th_s}^{2}} \frac{\partial}{\partial t}) T(\rho, t) = -\frac{\alpha_s}{\kappa_s} I(r, t), \qquad (\rho \in V) \qquad (5.1)$$

$$(\nabla_{\rho}^{2} - \frac{1}{D_{th}^{2}} \frac{\partial}{\partial t}) T(\rho, t) = 0 \qquad (\rho \notin V) \qquad (5.2)$$

where $D^2_{th}(= \kappa/(\sigma_m C_p))$ is the thermal diffusion coefficient; κ is the thermal conductivity; and V is the internal domain of the particle. The subscript s represents the material constants of the particle. The excitation beam $I(\mathbf{r}, t)$ has been given as Eq. (2.4). The heat $H(\mathbf{r}, t)$ transferred from the particles to the medium is obtained by the integral of the heat flux J on the particle surface S,

$$H(\mathbf{r}, t) = \int_S J d\mathbf{S} \qquad (5.3)$$

where

$$J = -\kappa \mathbf{n} \cdot \nabla_{\rho} T(\rho, t). \qquad (5.4)$$

Considering that the particles spread in the medium uniformly, the distribution of the total heat quantity in a unit volume of the medium $H_{total}(\mathbf{r}, t)$ is described using a simple sum of the heat from each particle, and

$$H_{total}(\mathbf{r}, t) = NH(\mathbf{r}, t) \qquad (5.5)$$

where N is the number density of the particles in the sample.

The heat distribution $H_{total}(\mathbf{r}, t)$ fluctuates periodically corresponding to the beam modulation $M(t)$ in $I(\mathbf{r}, t)$ of Eq. (2.4). In turn, this heat variation in the system becomes the acoustic source term. Impulse response $D(t)$ can be obtained from analyzing the equation system, Eqs. (5.1) - (5.5).

(b) Impulse response

To obtain a concrete form of the impulse response $D(t)$, the explicit expression of $H_{total}(\mathbf{r}, t)$ is calculated. From Eqs. (5.1) and (5.3) - (5.5), $H_{total}(\mathbf{r}, t)$ is given as follows.

$$H_{total}(\mathbf{r}, t) = N \int_S -\kappa \mathbf{n} \cdot \nabla_\rho T(\rho, t) ds$$

$$= N \int_V -\kappa \nabla_\rho^2 T(\rho, t) d\rho$$

$$= N\kappa \int_V \left\{ \frac{1}{D_{th_s}^2} \frac{\partial}{\partial t} T(\rho, t) - \frac{\alpha_s}{\kappa_s} I(\mathbf{r}, t) \right\} d\rho \qquad (5.6)$$

When the heat capacity of the particles is sufficiently small in comparison with that of the medium, the particles are uniformly heated and cooled, and Eqs. (5.1) and (5.2) give the temperature of the particles by the following differential equation (Jacob, 1957),

$$\sigma_{m_s} C_{Ps} \frac{d}{dt} T_s(t) = hS(T_s(t) - T_f) + \alpha_s I_0 V R(\mathbf{r}) M(t) \qquad (5.7)$$

$$T(\rho, t) = \begin{cases} T_s(t) & (\rho \in V) \\ T_f & (\rho \notin V) \end{cases}$$

where h is the coefficient of heat transfer from the particles to the medium. The integral of Eq. (5.6) is also simplified using the same approximation, and is

$$H_{total}(\mathbf{r}, t) = -N\kappa V\left\{\frac{1}{D_{th_s}^2}\frac{\partial}{\partial t}T_s(t) - \frac{\alpha_s I_0}{\kappa_s}M(t)R(\mathbf{r})\right\} \tag{5.8}$$

With the Fourier images of Eqs. (5.7) and (5.8), $T_s(t)$ is eliminated and $H^f_{total}(\mathbf{r}, \omega_0)$ is obtained as

$$H^f_{total}(\mathbf{r}, \omega_0) = -\frac{\kappa}{\kappa_s}\frac{C_s}{\sigma_{m_s}}\frac{\frac{S}{V}h}{\sigma_s C_{Ps} i\omega_0 + \frac{S}{V}h}\alpha_s I_0 M^f(\omega_0)R(\mathbf{r}) \tag{5.9}$$

where C_s ($= NV\sigma_s$) is the concentration of the sample. Therefore, comparing Eq. (5.9) with Eqs. (2.7), the function $D^f(\omega_0)$ is obtained formally as

$$D^f(\omega_0) = \alpha_s I_0 \eta_D \frac{\frac{S}{V}h}{\sigma_{m_s} C_{Ps} i\omega_0 + \frac{S}{V}h} \tag{5.10}$$

$$\eta_D \equiv \frac{\kappa}{\kappa_s}\frac{C_s}{\sigma_{m_s}} \tag{5.11}$$

As described above, the transfer function $D'(\omega_0)$ which is the Fourier image of the impulse response $D(t)$ is obtained formally, and the PA signal from turbid particles is obtained from Eq. (2.8) without directly solving the wave equation. The PA signal detected with CW PAS is also obtained formally with Eqs. (5.10) and (2.20), and the signal magnitude and phase are given by Eqs. (2.22) and (2.23), together with Eq. (5.10).

In particular, the $D'(\omega_0)$ term clearly expresses the effect of the thermal (C_{P_s} and h) and geometrical (S/V) properties of the particles on the PA signals. From Eq. (5.10), the value of $D'(\omega_0)$ becomes $\alpha_s I_0 \eta_D$ under the limitation of $V \rightarrow 0$, and Eq. (2.22b) is reduced to the PA signal generated in the true solutions as shown in Eq. (4.4).

(c) Physical meaning of phase

The phase of the PA signal which dominates in the thermal process is obtained as the argument of the transfer function $D'(\omega_0)$ as shown in Eq. (2.23), and it is calculated from Eq. (5.10) as follows,

$$\Phi_D = \tan^{-1} \frac{\sigma_{m_s} C_{P_s} V}{Sh} w_0. \tag{5.12}$$

It is developed for spherical particles as

$$\Phi_D = \tan^{-1} \sigma_{m_s} C_{P_s} \frac{d}{3h} w_0. \tag{5.13}$$

To clarify the physical meanings of the phase shift, Eq. (5.12) is rewritten as

$$\Phi_D = \tan^{-1} \frac{\tau_D}{\tau_f} 2\pi \tag{5.14}$$

where

$$\tau_D = \frac{\sigma_{m_s} C_{P_s} V}{Sh}, \tag{5.15}$$

$$\tau_f = \frac{1}{f}, \tag{5.16}$$

and f ($\omega_0 = 2\pi f$) is modulation frequency. The denominator of Eq. (5.15) means the heat release quantity per unit time and unit temperature difference between the particles and the medium, while the numerator is the heat capacity of the particles. Hence τ_D means the time required for heat release from the particles to the medium. The phase shift means the delay angle of the PA signal generation determined by the ratio between the heat release time τ_D and the modulation period τ_f.

Using the expressions of Eqs. (5.15) and (5.16), $D^f(\omega_0)$ is rewritten as a function of τ_D,

$$D^f(\tau) = \alpha_s I_0 \eta_D \frac{1}{\frac{\tau_D}{\tau_f} i + 1}. \tag{5.17}$$

Hence, $D^f(\tau)$ is understood as the effect of the macroscopical energy migration time, that is the heat release time, on the PA signal. Thus, concrete expressions of the PA signal from microparticles in liquids are obtained and physical meanings are clarified. These theoretical results are applied to characterizations of turbid solutions such as trace

determination, size measurement and thermal characterization in the subsequent sections.

(d) Theory verification

For experimental verification of the theoretical results, the phase of the PA signals is measured with polystyrene turbid solutions to confirm the linear relationship between $\tan\phi_D$ and ω_0 in Eq. (5.13). The experimental setup is shown in Fig. 5.2. The PA cell is a cylindrical direct coupling cell for which the radius is 4.5 mm (Chapter III). The excitation beam is modulated sinusoidally with an AO modulator. The experimental parameters are listed in Table 5.1. The concentration of the turbid solutions and the output of the excitation beam are low enough to avoid noise generation by direct exposure of the scattered beam to the detector.

In Eq. (2.23), the phase of the PA signal is given as the sum of the two terms, that is, ϕ_D and ϕ_Q. However the measured phase in the experiments contains the additional phase ϕ_m due to the response of the detector and the amplification system. Hence the measured phase ψ_m for turbid solutions is written as,

$$\Psi_m = \phi_D + \phi_Q + \phi_m \tag{5.18}$$

In this experiment, the background phase ψ_B is,

$$\Psi_B = \phi_Q + \phi_m. \tag{5.19}$$

As ϕ_Q represents the phase due to generation and propagation of the PA signal in a true solution, this background phase ψ_B is measured with the

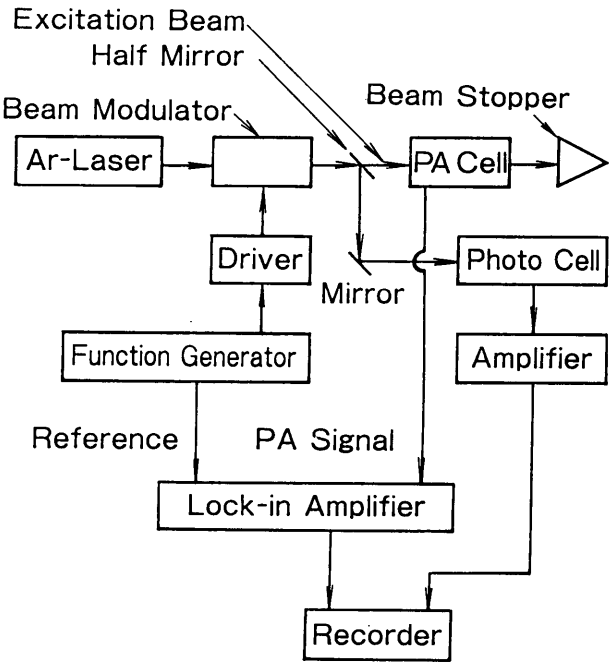

Fig. 5.2
Experimental setup for the phase measurements.

Table 5.1. Experimental parameters.

Parameter	Value
Light source	
Incident laser beam power	50 mW
Beam wavelength	488 nm
Sample	
Medium	water
Particle	polystyrene
Radius of the particle (d)	2.5 μm*

* The center radius of the particle size distribution for which the dispersion is 0.13 μm.

same PAS system for phase measurements as pure water which does not include any particulate impurities. Therefore ϕ_D is obtained as $\Psi_m - \Psi_B$.

The measured phase ϕ_D is plotted in Fig. 5.3. The theoretical values calculated with Eq. (5.13) are indicated by the solid line there.

The experimental results show the linearity between $\tan\phi_D$ and ω_0 for the slope = 1 obtained in the log-log plot of Fig. 5.3, and the absolute values of ϕ_D, both experimental and theoretical, agree with each other. Therefore, the liner relationship between $\tan\phi_D$ and ω_0 shown in Eq. (5.13) is confirmed. Futhermore, propriety of the general theory developed in the second chapter is also verified through the experimental confirmation of the theoretical results which have been obtained formally from the general theory.

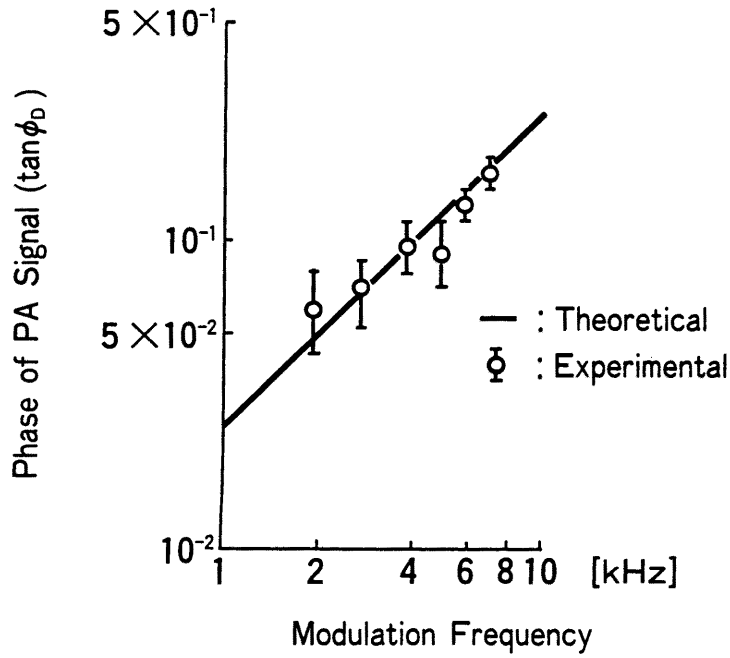

Fig. 5.3 The frequency characteristics of the PA signal phase from a 2.5 μm polystyrene turbid solution. The experimental parameters are listed in Table 5.1. The background phase Ψ_B due to ϕ_Q and the response characteristics of the detector and the amplification system ϕ_m are measured with water; the results plotted in the figure compensate for this.

5.2 Trace Determination of Turbid Component

The theory developed in the former section supports the experimental results obtained by Oda, et al. (1980), in which the calibration curves for barium sulfate turbid solutions having different size distributions (0.5 - 6.0 μm and 2.0 - 20.0 μm) overlapped each other and showed that the sensitivity did not depend on the size distribution.

As discussed in section 3.3, it was recommended that the beam modulation frequency was set in the relatively low frequency region of 10^1 - 10^2 Hz in analytical applications. In the experiments of Oda, et al. (1980), the modulation frequency was 33 Hz. When the modulation frequency is low enough and τ_f is sufficiently larger than τ_D, the value of $D'(\tau)$ becomes $\alpha_s I_0 \eta_D$, as is got from Eq. (5.17), and Eq. (2.22) shows that the magnitude of the PA signal does not depend on the particle radius. Therefore, when the modulation period τ_f is sufficiently larger than τ_D, the PA signal is proportional to the concentration as shown in Eq. (5.11), and the calibration curve does not depend on the particle size. The physical meaning of this property can be explained as follows: when the heat release time τ_D is sufficiently shorter than the modulation period τ_f, the heat generated in the particles is completely released in one cycle of the beam modulation and no heat remains in the particles; hence all the absorbed optical energy which is proportional to the concentration of the turbid components contributes to generation of the PA signal, the same as in true solutions; therefore, the sensitivity does not depend on the particle size.

Using Eq. (5.15), the parameters listed in Table 5.2, and applying the approximation of $h \simeq \kappa/d$, τ_D for these $BaSO_4$ particles of 0.5 - 20.0 μm is calculated to be 3.0 - 460.2 μs, and the value of τ_f is 3.0×10^{-2} s.

Hence, in the experiments by Oda et al., τ_D was fortutiously small enough for the approximation $D^f(\tau) \simeq \alpha_s I_0 \eta_D$ to be valid.

However, the present theoretical and experimental results based on the thermal properties of the particles cannot be applied in all PA determinations for turbid solutions. When the excitation beam wavelength corresponds to the particle size, the sensitivity depends remarkably on the particle size due to the optical property of the particles; examples of this and its application to immunoassay are presented in the next chapter.

5.3 Size Measurement

When the heat release time from the particles to the medium is sufficiently shorter than the modulation period, the effect of the particles as a heat saver is lost, and the PA signal in the turbid solution becomes the same as that of a true solution as shown in the previous section. Conversely, when the heat release time τ_D cannot be neglected in comparison with the modulation period τ_f, the PA signal is affected by the thermal energy migration as shown in $D^f(\tau)$ of Eq. (5.17) and its phase, signal magnitude and waveform vary from the PA signal in a true solution. In this section, the phase shift of the PA signal due to the dependence of the thermal energy migration on geometrical properties of the particles is applied to size the turbid particles.

When microparticles are small enough and their Grashof number is negligibly small, the heat transfer coefficient becomes κ/d (Jacob, 1957). Therefore, the following relationship for the size measurement is obtained from Eq. (5.13),

$$d^2 = \frac{3\kappa}{\sigma_{m_s} C_{Ps} w_0} \tan\phi_D \qquad (5.20)$$

When the components of the microparticles and the medium are known, a calibration curve for the size measurement is obtained from Eq. (5.20).

(a) Experimental

To verify the proposed sizing method, the dependence of the phase ϕ_D on the radius of the microparticles is measured with polystyrene turbid solutions of different particle radii of 0.4, 0.5, 1.2, 3.2 and 5.2 μm. Turbid solutions with 1 ppm of solid are prepared by stepwise dilutions of standard stock solutions of 10 % solid using distilled and demineralized water filtered through 0.1 μm membrane filters. A portion of each turbid solution is filtered through the 0.1 μm membrane filter, and the particle radii are measured by observation with a scanning electron microscope (SEM).

The experimental equipment and the cell are the same as that used in the former section. The experimental parameters are also the same as those listed in Table 5.1, except for the modulation frequency which is set at 6.5 kHz using an AO modulator.

The background phases ϕ_Q and ϕ_m which originate in propagation of the signal and system response are subtracted, using the procedure of subsection 5.1 (d). The background phase ψ_B is measured with water subjected to the following ultrapurification steps: distillation in a glass apparatus, two demineralizations with a resin ion exchanger, and filteration through an activated carbon filter and a membrane filter. The resistivity of the obtained water is about 18 MΩ/cm, and particulate impurities above 0.1 μm are almost completely removed, hence the PA signal

generated from any impurities is negligibly small in comparison with that of water itself. The phase ψ_m for each polystyrene turbid solution and the background phase ψ_B for the water are measured. The phase ϕ_D for each radius is calculated as $\psi_m - \psi_B$. The results obtained are plotted in Fig. 5.4.

(b) Results and discussion

The theoretical values of the phase shift for the polystyrene microparticles are calculated with Eq. (5.20) using the parameters listed in Table 5.2, and the values are indicated in Fig. 5.4 by the solid line. The experimental results agree well with the theoretical values within the experimental accuracy and the size distributions of each solution. Hence the relationship between the phase shift of PA signals and the radius of the microparticles in liquids, expressed in Eq. (5.20), is confirmed, and the size measurement based on the relationship is verified. However, the slope of the regression line in the graph is smaller than that of the theoretical values. This seems to be due to approximation of the heat transfer coefficient $h = \kappa/d$, in which additional terms with respect to the particle radius d, originating in the Grashof number, are neglected (Ranz, 1952).

The phase measurement accuracy of the present PAS equipment is ± 0.2 deg, hence the lower limit of the size measurement, defined as twice the experimental accuracy, is calculated as d = 0.48 μm using Eq. (5.20). In Fig. 5.4, the experimental values at d = 0.4 and 0.5 μm, including their error bars are overlapped, and closely approach the lower sizing limit. The physical limitation of this sizing method is determined by microscopic energy migration in thermal process, such as nonradiative relaxation. When the macroscopic thermal energy migration time, that is the heat release time of the particle closely approaches the nonradiative

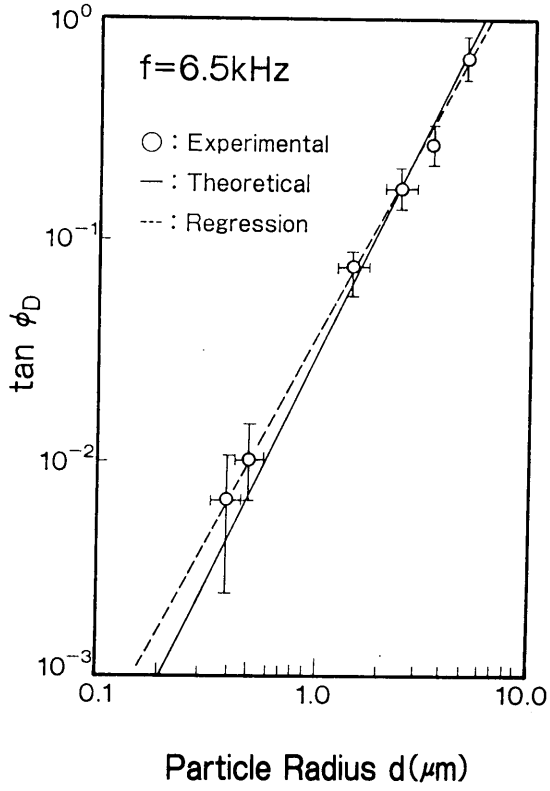

Fig. 5.4
Dependence of the phase shift on the radius of polystyrene microparticles in liquids. The solid line is the theoretical values calculated with Eq. (5.20), and the dashed line is the regression line for the measured values. The experimental parameters are listed in Table 5.1, and the material constants for the calculation are listed in Table 5.2.

Table 5.2. Material constants.

Symbols	Parameter	Value
(Polystyrene)		
C_{Ps}	Specific heat	1.22×10^3 J/kgK
σ_{m_s}	Density σ_{m_s}	1.05×10^3 kg/m^3
(Water)		
κ	Heat conductance	6.3×10^{-1}J/msK
($BaSO_4$)		
C_{Ps}	Specific heat	4.36×10^2 J/kgK
σ_{m_s}	Density	4.49×10^3 kg/m^3

relaxation time of the particle component, the origin of the phase shift cannot be identified. Details of the phase shift due to nonradiative relaxation time are discussed in Chapter VIII, however, this critical phase shift ϕ_c is given as

$$\tan\phi_c = w_0\tau_N \tag{5.21}$$

where τ_N is the nonradiative relaxation time. Therefore, from Eqs. (5.21) and (5.20), the limitation of the present sizing method becomes 10^2 Å for τ_N = 1 ns as an ideal example.

Equation (5.20) shows that the tangent of the phase shift ϕ_D is proportional to the modulation frequency ω_0, as was also verified in the previous section. According to this relationship, the phase shift can be enlarged by using a higher modulation frequency, and the size measurement limit can be lowered. However, a more sensitive PAS system is required for use of higher modulation frequencies than 6.5 kHz, at which the present experiment is carried out. This is because the PA signal magnitude decreases with increased modulation frequency as shown in section 2.4, and the signal magnitude becomes insufficient for phase measurements above the 6.5 kHz modulation frequency region in the present PAS system. The detection, counting and sizing of ultrafine particles smaller than 0.1 μm is performed in Chapter VII using a breakdown acoustic effect.

5.4 Thermal Characterization

As shown in Eq. (5.15), heat release time is characterized by the thermal properties of the microparticles such as specific heat C_{P_s} and heat transfer coefficient h. In particular, Eq. (5.13) shows that h, the coefficient of heat transfer from a microparticle to the medium which is not easily measured with a conventional experimental method, can be obtained from the measurement of frequency characteristics of the phase shift ϕ_D. In this section, the heat transfer coefficient of spherical polystyrene microparticles in water is experimentally obtained from the frequency characteristics of the phase shift based on Eq. (5.13). The measurement procedure is as follows: the frequency characteristic of $\tan\phi_D$ is measured; the gradient Λ of the linear relationship between $\tan\phi_D$ and beam modulation frequency $f\,(=\omega_0/2\pi)$ is obtained from the frequency characteristic; and the heat transfer coefficient is calculated from Eq.(5.13) as

$$h = \frac{2\pi\sigma_{m_s} C_{Ps} d}{3\Lambda} \tag{5.22}$$

For the experimental verification of the proposed thermal characterization, the experimental results of the frequency characteristic of the phase shift obtained in section 5.1 are derived in this section. The experimental results are obtained with polystyrene turbid solution. The shape of the polystyrene particles is confirmed by SEM observation to be spherical, and the center radius of the particle size distribution is 2.5 μm for which the dispersion is ± 0.13 μm.

The experimental results are replotted in Fig. 5.5. The regression line for the experimental values is calculated with a least squares

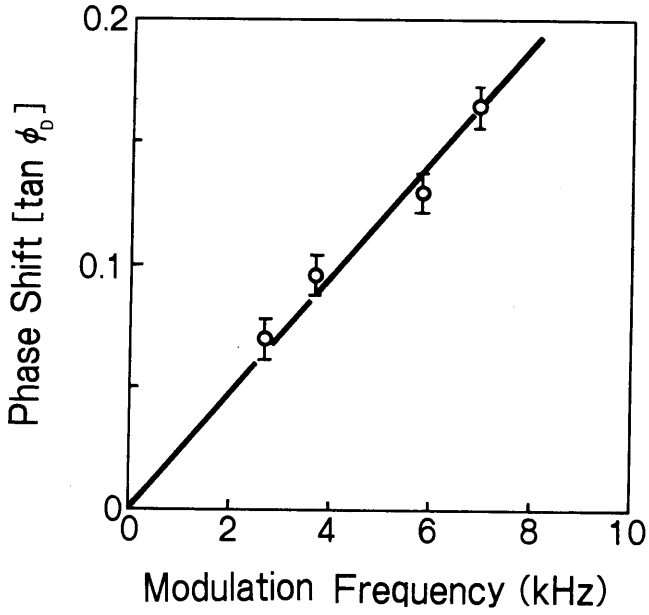

Fig. 5.5
Frequency characteristics of the phase shift.

method, and is shown by the solid line. The experimental values are on the regression line within the measurement error of ± 0.2 deg. The gradient Λ of the regression line is 2.7×10^{-5} s, hence the experimental value for the heat transfer coefficient h_{ex} of the particle to the medium is calculated to be

$$h_{ex} = (2.7 \pm 0.2) \times 10^{1} \ \mathrm{Jcm^{-2}K^{-1}}$$

from Eq. (5.13) considering the dispersion of the particle size. On the other hand, the heat transfer coefficient of the microparticles is described theoretically as $h_{th} = \kappa/d$ for convection heat transfer (Jacob, 1957), and the value of h_{th} is calculated as

$$h_{th} = (2.5 \pm 0.2) \times 10^{1} \ \mathrm{Jcm^{-2}K^{-1}}$$

where the dispersion of d is taken into account. These values h_{ex} and h_{th} closely agree within the error due to the particle size dispersion.

Therefore measurement of the heat transfer coefficient, based on Eq. (5.13), is verified.

In reexamining the experimental results of this chapter, the appropriateness of the present theory for analysis of phase shift is confirmed with the measurements of the linearity between $\tan\phi_D$ and ω_0, size dependence of the phase, and the heat transfer coefficient. Equation (5.13) shows that the phase shift ϕ_D includes information not only about the heat transfer coefficient, but about the specific heat C_{p_s} and density σ_{m_s}. These constants can be measured with the same experimental methods developed in this section. As trace turbid component can be determined by PAS (section 5.2), the various parameters of turbid solutions are characterized by properly selecting a modulation frequency with regard to the heat release time of the microparticles. Therefore, PAS is expected to be a useful tool for study of colloidal and turbid solutions.

5.5 Conclusion

In this chapter, PAS was applied to characterization of turbid solutions. First, the PA signal from microparticles in liquids was theoretically analyzed using the general theory. On the basis of the theoretical findings, using the phase shift of the PA signal due to the heat release time of the particles, a unique sizing and measurement method for thermal constants of the particles such as the heat transfer coefficient were proposed, as well as the ultratrace determination in which the sensitivity was independent of the particle size. The proposed sizing and characterization method was proved experimentaly using polystyrene turbid solutions. First, the phase shifts were measured at the modulation frequency of 6.5 kHz, with polystyrene turbid solutions

having particle radii of 0.4 - 5.2 μm. The experimental results agreed well with the theoretical values. The heat transfer coefficient of polystyrene microparticles (radius; 2.5 μm) was obtained from the gradient of the regression line for $\tan\phi_D$ and ω_0. The experimental value (2.7 ± 0.2) X 10^1 $Jcm^{-2}K^{-1}$ agreed well with the theoretical value of the convection heat transfer coefficient.

CHAPTER VI PHOTOACOUSTIC IMMUNOASSAY

Photoacoustic spectroscopy was seen in Chapter V as a effective measurement method for characterization of turbid solutions. Since samples of wet analysis in medical and biochemical fields often include various particulate components such as blood corpuscles, cells, macromolecule proteins, pathogenic microbes and microorganisms, PA determination is particularly effective for determination and assay of these particulate components, unlike the conventional method of turbidimetry which is not very sensitive and less accurate. As an example of medical application of PAS, photoacoustic immunoassay (PIA), in which the newly obtained sensitivity size dependency is applied, is proposed and verified (Kitamori et al., 1987).

As discussed in section 5.2, Oda et al. (1980) observed that the sensitivity of PAS, i.e. the slope of the calibration curve, was independent of particle size at relatively low modulation frequency. Since the heat release time of microparticles is negligibly shorter than the beam modulation period and the particle does not act as a heat saver, almost all the absorbed optical energy is released to the medium and contributes to PA signal generation as in a true solution. Oda et al. showed that two calibration curves for a precipitated $BaSO_4$ mixture of 6 - 20 μm and 0.5 - 6 μm particles overlapped each other when the 514.5 nm lasing line of an Ar-laser was used for the excitation beam. However, in the present study, a remarkable size dependence of sensitivity is found when the particle size is in a region close to that of the excitation beam wavelength. Reasons which explain both independence and dependence of the sensitivity on size are investigated and reported herein.

The latex agglutination method has been developed to improve the sensitivity of turbidimetric immunological determinations (Singer and Plotz, 1956), and details of this method are introduced in section 6.2. In brief, antigen/antibody is determined in serum through determination of immunoreactant agglutination of latex particles which are coated with antibody/antigen. Then, PIA which determines selectively and at high sensitivity the latex agglutinations, using the identified sensitivity dependency on particle size, is proposed. The principle of PIA is verified by determination of rheumatoid factor (RF) as a sample antigen.

6.1 Size Dependency of Sensitivity

In previous works (Oda et al., 1980; Nomura et al., 1982), PA determinations were performed for turbid solutions in which turbid components were larger than the excitation beam wavelength, and it was shown that the sensitivity was independent of particle size. In this section, PA determinations are done using polystyrene turbid solutions in which particle sizes are close to the excitation beam wavelength. Under these experimental conditions, a remarkable size dependence of sensitivity is found. The physical meanings of the sensitivity characteristics of PA determination are discussed on the basis of thermal and optical properties.

(a) Experimental

All reagents are spectral or biochemical grade. Ultrapurified water is prepared by filteration with reverse osmotic membranes, ion-exchange filters, and membrane filters to remove particulate impurities.

Particulate impurities larger than 0.1 μm are almost completely removed. Water conductivity is about 18 MΩ/cm.

Monodispersed polystyrene latex particles of uniform size (0.10, 0.22, 0.33, 0.50, 0.80, 1.0, 2.0, 3.0, and 5.0 μm, Nissin EM Co., Ltd.) are prepared by stepwise dilution from 0.2 w/w % standard stock solutions. First, the concentration of the samples are roughly diluted to 0.1 - 1.0 ppb, and then, after filtering 100 mL portions of the respective samples, the exact concentration and particle size of each sample are calibrated by counting and observing particles on the filters through a scanning electron microscope (SEM).

A block diagram of the PAS system used in this chapter is shown in Fig. 6.1. The excitation beam is the 488 nm lasing line of the Ar-laser, and the beam power is 1.8 W. The excitation beam is modulated at 181 Hz with a light chopper. The PA cell shown in Fig. 6.2 is a cylindrical direct coupling cell and a flow type so that the sample can be exchanged easily. However, to reduce the noise level, the PA signal is measured when the flow is stopped. The cell is set in a stainless steel case to shield it from electro-magnetic noise sources (section 3.4).

For each particle size, the PA signal magnitude at four concentrations of the polystyrene latex turbid solutions in the range of 0.1 - 1.0 ppb is measured, and calibration curves are obtained as regression lines. The sensitivity of PAS, that is the slope of the calibration curves, is calculated for each particle size.

(b) Results and discussion

The size dependence of sensitivity is shown in Fig. 6.3. The error bars are statistically obtained as the standard deviations for the determination of the particle number densities by SEM observation. The sensitivity depends remarkably on the size between 0.3 - 0.8 μm, but such

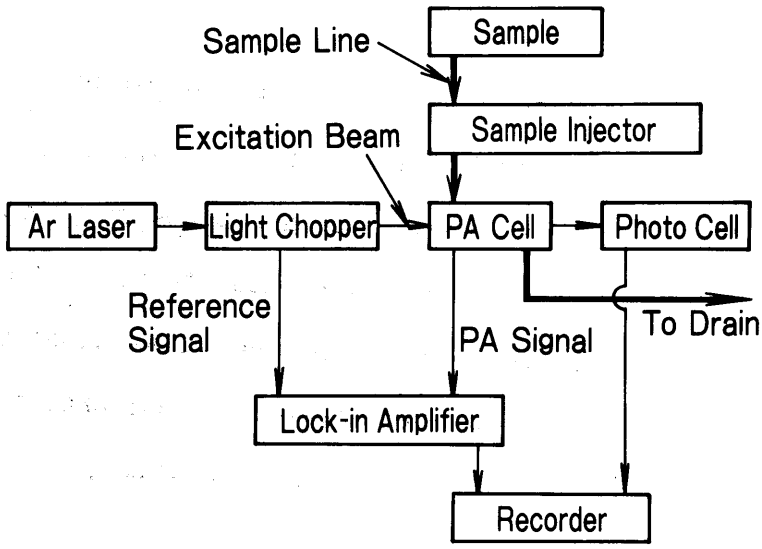

Fig. 6.1 Block diagram of the PAS system for PIA.

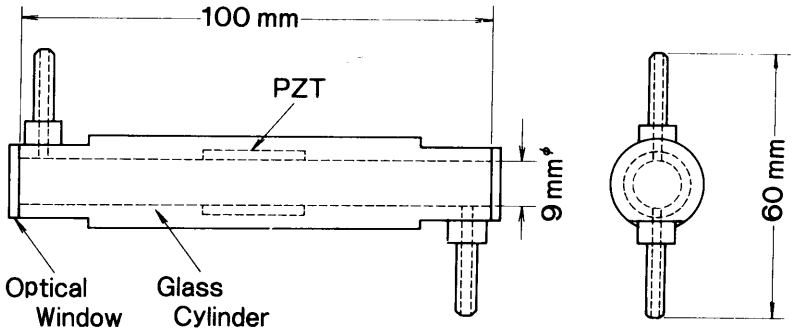

Fig. 6.2 Side and front views of the cylindrical direct coupling PA cell.

behavior is not conspicuous below 0.2 μm or above 1.0 μm. The maximum sensitivity appears at 0.5 μm where the particle size coincides with the excitation beam wavelength.

Under the present conditions, the heat release time τ_D for the polystyrene microparticles of 0.3 - 5.0 μm is calculated to be 10^{-1} - 10^{0} μs from Eq. (5.15), while the modulation period τ_f is 5.5 ms. Hence the value of $D'(\tau)$ becomes $\alpha_s I_0 \eta_D$ as obtained from Eq. (5.17), and the PA signal magnitude and sensitivity are independent of particle size as shown in section 5.2. Therefore, the obtained sensitivity characteristics do not originate in the thermal property of the microparticles, which is the dominant factor in determining the energy migration in the thermal process.

The physical meaning of this size dependence of the sensitivity is not clear at present. However, it seems to be caused by a size dependence of the absorption cross-section of the particles, which is due to dielectric loss accompanied by light scattering. Figure 6.4 shows the size dependence of the PA signal magnitude per one particle, which is obtained by dividing the experimental values in Fig. 6.3 by the particle number in 1 ppb polystyrene turbid solutions of corresponding sizes. The error bars also indicate statistical error as shown in Fig. 6.3. The PA signal magnitude per one particle is proportional to the absorbed optical energy per one particle, that is, the absorption cross-section of the particles. For particle sizes below 0.2 μm in Fig. 6.4, the PA signal per one particle is proportional to the third power of the size. This corresponds to the dependence of the absorption cross-section on the volume of the scattering body, which is described using Rayleigh's approximation for a scattering body small compared to the wavelength (Landau and Lifshitz, 1960). In the particle size region from 0.3 to 0.8 μm, the PA signal magnitude varies and it has a peak at the particle size

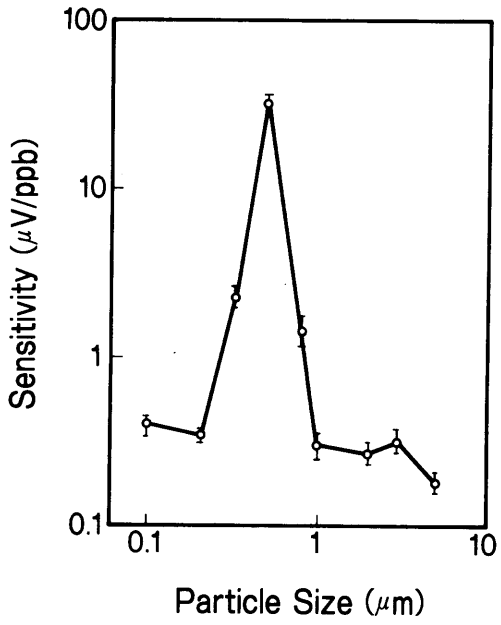

Fig. 6.3
Size dependence of PAS sensitivity. Sensitivity is obtained as the slope of the calibration curves for each size.

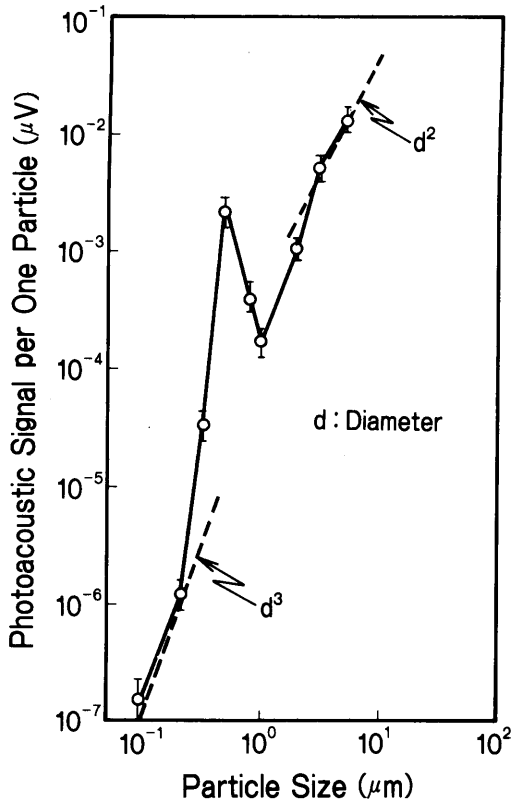

Fig. 6.4
Size dependence of the PA signal magnitude per one particle. The signal magnitude is proportional to the absorbed optical energy, hence the vertical axis is proportional to the absorption cross-section of the particles.

coinciding with the wavelength of the excitation beam. This behavior seems to show a change in absorption cross-section to accompany resonance scattering which appears in the particle size region near the excitation beam wavelength (Van de Hulst, 1957). Beyond 1.0 μm, the PA signal magnitude per one particle asymptotically approaches a quadratic dependence on the particle size. This tendency shows the size dependence of the absorption cross-section to accompany light scattering by a large particle compared to the wavelength of the excitation beam. In this size region the absorption cross-section is proportional to the geometrical cross-section of the scattering body (Van de Hulst, 1957). Therefore, from these characteristics of the PA signal magnitude per one particle, the physical meaning of the size dependence of the sensitivity shown in Fig. 6.3 is considered to originate in the size dependence of the absorption cross-section of the particles.

From the above discussion, the following inference can be drawn. A particulate sample has two types of optical absorption. The first is a photon absorption process based on excitation between electronic energy states. This absorption process is unique for the material, and is identical for both bulk and particulate states. Hence, the quantity of absorbed optical energy is proportional to the quantity of material in the medium, that is, the material concentration, and the absorbance of the turbid solution is independent of size. The second absorption process is the absorption of the excitation beam as an electro-magnetic wave due to dielectric loss accompanied by light scattering. This process is unique for particulate samples. Most of the optical energy absorbed by both processes is converted to thermal energy and it contributes to generation of PA signals. Under the experimental conditions used by Oda et al. (1980), the size of the $BaSO_4$ precipitates was several times larger than the excitation beam wavelength, and optical absorption of the first type

was considered to be dominant. Hence it was stated that sensitivity of PAS for $BaSO_4$ turbid solutions was independent of size. On the other hand, under the present experimental conditions, optical absorption of the second type is dominant, and PAS sensitivity depends remarkably on size.

6.2 Latex Agglutination Method and PIA

The latex agglutination method, one immunoassay method is introduced in this section. Photoacoustic immunoassay is, then, proposed where the PA determination is applied to the latex agglutination method using the obtained sensitivity size dependency for selective and highly sensitive determination of the immunoreactant.

(a) Principle of latex agglutination method

The latex agglutination method was developed to improve the sensitivity of turbidimetric immunological determination (Singer and Plotz, 1956). A schematic illustration of the immunoreaction in the method is shown in Fig. 6.5. Latex microparticles which are coated by an antibody/antigen are added to the sample, and they agglutinate with each other due to an immunoreaction, allowing the antigen/antibody to be determined on the basis of turbidimetric analysis or particle counting of the agglutinations. Because the size distribution of the agglutinations is determined by the conditions of the immunoreaction such as temperature and number density of the latex particles which dominate the collision probability of the latex particles, then concentration of the agglutinations is proportional to the antigen/antibody concentration.

The detection limit of this immunoassay method is two to three orders lower in comparison with the ordinary turbidimetric immunoassay without

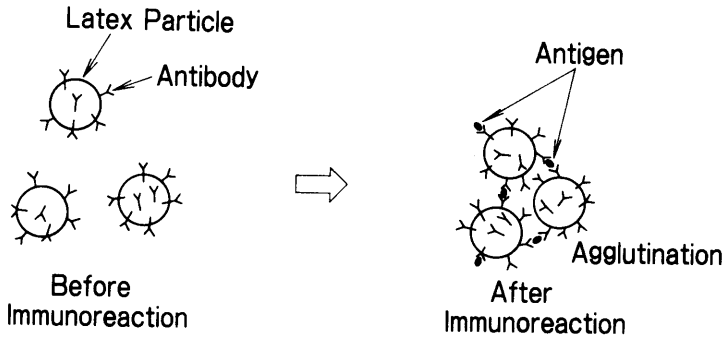

Fig. 6.5 Schematic illustration of immunological reaction in latex agglutination method.

latex microparticles in which precipitates of antigen-antibody reactants are determined (Cambiasso et al., 1977). In general, however, the lower determination limit which is set by the detection limit of the turbidimeter is still one to two orders higher than radio immunoassay (RIA) and enzyme immunoassay (EIA), and is about two orders higher than that needed for determination of some kinds of cancer and tumor marker proteins such as carcinoembryonic antigen (CEA) and hormones which are at sub-ng/mL concentrations (Hirai, 1977; Albertsen, 1983).

(b) Proposal for PIA

The latex agglutination can be determined selectively and ultrasensitively with PAS using the sensitivity dependence on particle size. In this novel method, the size of the latex agglutinations is controlled to lie within the highest sensitivity region of PAS. The agglutinations in the mixture of various particulate components in the samples such as unreacted latex particles, proteins and cells are selectively determined. The reagent latex particles are prepared in a nonsensitive size region.

For example using the size dependence of sensitivity shown in Fig. 6.3, microparticles for which the size coincides with the wavelength of

the excitation beam can be specifically determined with PAS. In the present application of this determination method to immunoassay, latex particle agglutinations of about 0.5 μm, which are in a mixture of unreacted 0.2 μm latex particles and variously sized agglutinations, are selectively determined.

6.3 Determination of Trace RF

To verify the principle of PIA, trace rheumatoid factor (RF) is determined. With the experimental results, the determination limit of PIA is discussed, and the possibility of applicability of PIA to determination of cancer marker antigens is investigated.

(a) Reagents and apparatus

Stock solutions of 21, 42 and 84 U/mL RF are prepared by dissolving freeze-dried RF into ultrapurified water. (The international unit U for RF is defined by WHO, the World Health Organization. This unit is a measure for activity of the immunoreaction, and is not related to weight concentration because the existence ratio for active and nonactive RF is not constant (Anderson et al., 1970). The quantity of RF in serum of a healthy body is about 10 - 14 U/mL.) Denaturated γ-globulin coated polystyrene latex particles and glycine buffered saline, which contains bovine serum albmin and tris-buffer, are made up with the "IATROACE RF reagent I" kit (IATRON). Denaturated γ-globulin is used as an antibody of RF in the present experiment, while it is an antigen in a living body. The size of the latex particles is 0.2 μm.

The PAS system and cell are the same as that used in section 6.1. The excitation wavelength is also 488 nm (about 0.5 μm). A double beam absorption spectrophotometer is used for turbidimetry.

(b) Analytical procedure

After adding 3.5 mL of glycine buffered saline to the RF solutions of 30 μL and a blank solution, they are kept at 37 °C for five min, and a 1 mL portion of 0.03 w/w % polystyrene latex particle reagent is added to each solution. The immunoreaction is sufficiently progressed at the chosen temperature after an additional five min. After the immunoreaction, each solution is diluted by 1/20000, resulting in agglutination turbid solutions corresponding to RF concentration of 10^{-3} U/mL order. The calibration curve of RF is subsequently obtained by PAS.

Turbidity of the agglutination turbid solutions for which RF concentration is of 10^{-1} U/mL order is measured using a double-beam spectrophotometer.

(c) Results and discussion

The calibration curve obtained shows a good linearity for RF concentrations of 1.1×10^{-3}, 2.1×10^{-3} and 4.2×10^{-3} U/mL and the blank as shown in Fig. 6.6. The determination limit of RF, defined as double the standard deviation, is obtained as 9.8×10^{-5} U/mL. The coefficient of the relative standard deviation is 0.6 % at 1.1×10^{-3} U/mL for three determinations, hence the reproducibility is confirmed. On the other hand, the determination limit obtained with turbidimetry is 1.6×10^{-1} U/mL. Therefore, RF can be determined with PIA and the determination limit is at least three orders lower than that of the conventional immunoassay using turbidimetry with the latex agglutination method. From the obtained results, PIA is expected to be roughly one to

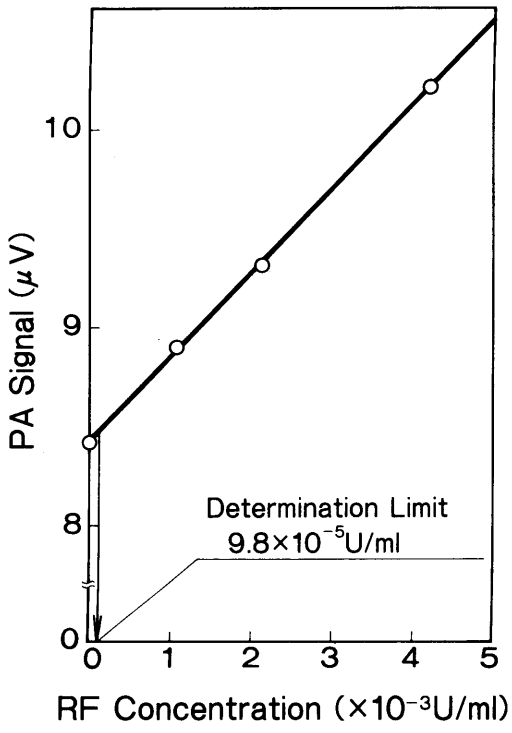

Fig. 6.6
Calibration curve of trace rheumatoid factor (RF).

two orders more sensitive than RIA and EIA (Addison, 1972; Asakawa and Mori, 1984), and it is anticipated as being applicable to determination for trace turmor and cancer marker antigens, such as α-fetoprotein, basic protein, and CEA (Nishi and Hirai, 1973; Ishii, 1978; Gold and Freedman, 1965; Hirai, 1977; Kodama, 1979). In addition, no unsealed radioisotopes are used in PIA, and it is advantageous for medical mass screening.

In this experiment, the possibility of PIA is demonstrated with samples prepared with 20000 dilutions. However, though the lower limit of the determination depends significantly on the background levels in the ultrasensitive determination with PAS as discussed in Chapter Ⅳ, suppression of the background originating in unreacted latex particles is not examined in the present immunoassay procedure, because it is based on a prescription for turbidimetry with a spectrophotometer which is not influenced by the background for its low sensitivity. The background level of 8.4 μV is a relatively large value in comparison with the slope of the calibration curve 0.42 μV/(10^{-3} U/mL), even though 0.42 μV is

distinguishable from the noise level 4 nV of the present PAS system. Therefore, further study for background reduction by optimizing the immunoassay procedure, applying a double-beam method (Sawada and Oda, 1981), developing a selective filteration technique of unreacted particles, etc., will be required before the practical application of PIA to clinical examinations is possible.

6.4 Conclusion

A remarkable size dependency for sensitivity, which was considered to originate in dependence on absorption cross-section, was observed in determinations with photoacoustic spectroscopy (PAS) on 0.1 - 5.0 μm uniform polystyrene latex turbid solutions. A resonant increase in sensitivity appeared at a cross-sectional size coinciding with the excitation beam wavelength. Photoacoustic immunoassay using the size dependency of sensitivity was proposed. In this method, antibody/antigen coated latex particles agglutinated due to an immunoreaction and the size of the agglutinations were controlled to be the same as the excitation wavelength. The aggulutinations in a mixture of unreacted latex particles and biological particulate substances were selectively determined by PAS and the antigen/antibody concentration was obtained. Using a rheumatoid factor and denaturated γ-globulin coated 0.2 μm polystyrene latex particles, the principle behind PIA was proved and a determination limit of 9.8×10^{-5} international unit/mL was obtained. This value was at least three orders better than results obtained by conventional turbidimetry, and the possibility for determination of ultratrace cancer marker antigens was noted.

CHAPTER VII DETECTION AND COUNTING OF ULTRAFINE PARTICLES IN LIQUIDS

As water and liquid reagents used in semiconductor technology and biochemical engineering are highly purified, analytical and detecting methods for ultratrace and ultrafine particulate impurities are desired. For example, the more the semiconductor elements are integrated, the narrower the linewidth of the circuit pattern on them becomes, and even ultrafine particulate matter, smaller than 0.1 μm, can break the insulation between wiring on ultra-large scale integrated circuits (ULSIs). Hence, detection, counting or determination methods of ultrafine particles in liquids are required for purity control of water and liquid reagents used in ULSI production.

The number density of these particulate impurities in ultrapure water is presumed to be 10^1 - 10^2 mL^{-1} or less from results of filter capture and SEM observation, and the corresponding weight concentration is estimated to 10^{-17} g/mL (10^{-5} ppt) - 10^{-14}/mL (10^{-2} ppt) for particle sizes of 0.01 μm - 0.1 μm. This is too dilute for even PA determination for which the determination limit of particulate substances was shown to be 10^0 - 10^1 ppt in Chapters V and VI. Therefore, as this particle number density is in a so-called particle counting region, particle counting by a method such as laser scattering has been tried to detect and count dilute ultrafine particulate impurities. However, the detection limit size for particle counting in liquids using laser scattering which is one of the most sensitive methods is about 0.1 - 0.3 μm, because of the background due to medium Rayleigh scattering, and it cannot be applied to count ultrafine particles in liquids. Then, development of a new method for counting of ultrafine particles in liquid is indispensable for ultrafine technologies such as ULSI production.

As shown in Chapters IV and VI, the lower limit of PA determination was dominated by background absorption of the solvent, and the determination limit was at ppt levels. The corresponding number density of ultrafine particles was more than 10^3 mL^{-1}, and the particle number in the excitation beam was estimated to be more than 10^2 mL^{-1} under the experimental conditions of Chapters III - VI in which the beam radius was 2 mm and its length was 100 mm. Hence the PA signal magnitude per one particle is anticipated to be less than 10^{-4} μV, and it is much smaller than the background levels of 10^0 - 10^1 μV, making detection and counting of ultrafine particles in liquid, one-by-one, impossible with the present measurement conditions. In addition, particle number in the excitation beam for a particle number density of 100 mL^{-1} which is the average value in ultrapure water is 31 particles under those experimental conditions, hence the spatial region in which the PA signal is generated is too wide to generate one signal from one particle. Therefore, the following two conditions are essential to detect and count ultrafine particles individually using PA or related phenomena: first, to generate a signal which has a more intensive magnitude to distinguish it from the background signal; and second, to reduce the spatial region to allow generation of one signal from one particle. The latter condition can be realized easily by using an optical system to focus the excitation beam. However, to achieve the first condition, finding a signal generation mechanism from a phenomenon which occurs for the particle, but not the solvent would be better than refining the present PAS system to recover extremely weak signals from the background.

In the present study, the mechanism of acoustic signal generation from a particle in liquid is found to shift from the PA effect to optical breakdown of the particle as power density of the excitation beam increases. It is also found that only the particle can be broken down by

laser irradiation, because its breakdown threshold is smaller than that of solvent. This breakdown acoustic effect of the particle is applied to ultrafine particle counting in liquids. Laser breakdown spectroscopy has already been studied and analytically applied to solid (Kagawa and Yokoi, 1982), gaseous (Cremers and Radziemsky, 1983) and liquid samples (Cremers et al., 1984). However, though a few studies on the accompanying acoustic emission have been reported (e.g. Bell and Landt, 1967), there was no attempt made to apply it to particle counting.

In this chapter, a novel counting method of ultrafine particles in liquids using the laser breakdown acoustic effect is proposed and verified experimetally using polystyrene ultrafine particles as sample (Kitamori et al., 1988a). Ultradilute and ultrafine particle counting at the particulate level of ultrapure water is demonstrated. From the experimental results, the possibility of size distribution measurements, applying the dependency of signal magnitude on particle size, is discussed.

7.1 Breakdown Acoustic Effect and Principle of Ultrafine Particle Counting

The breakdown acoustic effect is introduced and it is applied to particle counting in this section. A strong acoustic emission is generated from a particle by irradiation of a pulse YAG laser beam, and the principle of the particle counting is verified using 0.085 μm polystyrene ultrafine particles. The characteristics of the breakdown acoustic signal are discussed based on the recorded waveform.

(a) Breakdown acoustic effect and counting principle

Figure 7.1 shows a particle in a focused excitation beam. In the ordinary process of PA signal generation, the particle absorbs optical radiation and generate heat. The heat released from the particle causes a thermoelastic expansion of the medium, with generation of the PA signal as discussed in Chapter V. However, when the power density of the optical radiation in the beam waist is too high and exceeds the threshold of particle breakdown, the particle may become plasma and a strong acoustic emission due to explosive expansion and strong optical absorption of the plasma is expected. The optical breakdown threshold of solids is usually on the 10^{10} W/cm^2 order, hence a pulse laser system can be employed to obtain such an intensive optical power density.

When the breakdown threshold of a particle is smaller than that of solvent, optical breakdown is induced only when the particle exists in the beam waist, hence particles can be counted by detecting the breakdown acoustic signals. As shown in Fig. 7.1, approximately a cylindrical beam waist is formed by focusing the parallel beam due to a diffraction effect, though, more exactly, the beam waist is formed as a hyperboloid. The spot size and the length can be obtained from the theorem of the diffraction limit and Gaussian optics, and the volume V_{op} of the beam waist in the medium of refractive index n is roughly given as follows,

$$V_{op} = \pi\left(1.2\frac{F}{D_{op}}\frac{\lambda}{n}\right)^2\left(\frac{F}{D_{op}}\times 1.2\frac{F}{D_{op}}\frac{\lambda}{n}\times 2\right)$$

$$= 21.8\left(\frac{F}{D_{op}}\right)^4\left(\frac{\lambda}{n}\right)^3, \qquad (7.1)$$

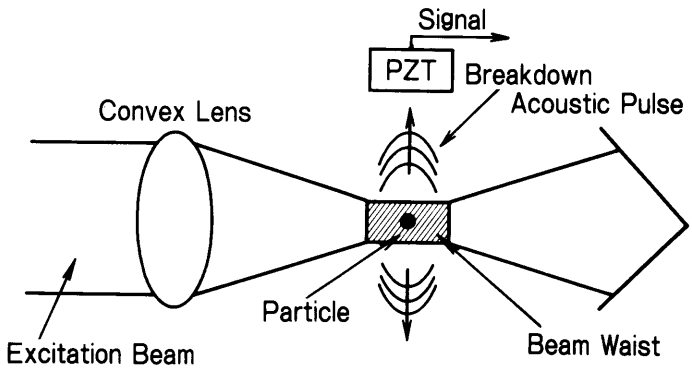

Fig. 7.1 A particle in a focused excitation beam.

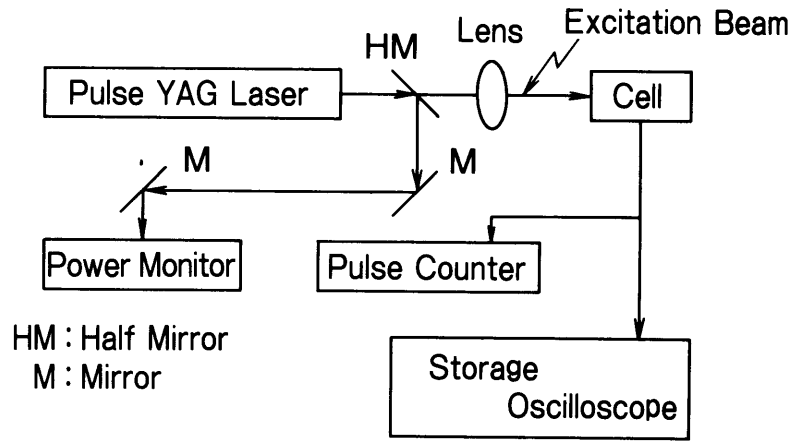

Fig. 7.2 Block diagram of the experimental apparatus.

where D_{op} is the beam diameter and F is the focal length. The expectation number n_e of particles in the beam waist in Fig. 7.1 is given as the product of the number density of the particles N and the volume of the beam waist, hence the expectation number of the breakdown acoustic signal generation, that is, the count expectation C_e is obtained with Eq. (7.1),

$$C_e = n_e F_p \tag{7.2a}$$

$$= N V_{op} f_p t, \tag{7.2b}$$

where F_p and f_p are total shot number of the excitation beam and its repetition ratio, respectively, and t is the measurement period. The number density of the particulate impurities can be obtained from the count number of the breakdown acoustic signal, refering to Eqs. (7.2).

(b) Experimental

To verify the counting principle of this method, a breakdown acoustic signal from a 0.085 μm polystyrene ultrafine particle is generated and measured.

A block diagram of the experimental setup is shown in Fig. 7.2. The beam source is a pulse YAG laser, and the excitation beam is the second harmonics of the 532 nm lasing line of which the beam diameter is 5 mm and pulse dulation is 6 ns. The excitation beam is focused by a convex lens of 50 mm focal length. The cell is a cylindrical PA cell (cf. Fig. 2.6), and its cell radius and length are 16 mm and 60 mm respectively. The breakdown acoustic signal detected in the PA cell is counted by the signal processor, and its waveform is recorded by a storage oscilloscope.

Monodispersed polystyrene latex particles of 0.085 μm uniform size are added to ultrapure water prepared by the procedure shown in section 6.1. Under the present experimental conditions, the volume of the beam

waist is calculated as 1.5×10^{-8} mL from Eq. (7.1). The number density of the particles, at which an expectation of the particle number in the beam waist becomes one per beam shot, is obtained as a reciprocal of the volume, and the value is 6.6×10^{7} mL^{-1} which corresponds to 23 ppb weight concentration. The essential condition for the present experiments is to detect a breakdown acoustic signal from one particle. Then, concentrations of the polystyrene turbid solutions are prepared at 0.5 - 2.5 ppb, because, the expectations of the particle number in beam waist at these concentration are less than about 0.1. Then, there would be little possibility of more than two particles being in the beam waist at the same shot.

First, the concentration dependence of the acoustic pulse counts is measured. The beam power of the excitation beam is set at 0.55 mJ and it is repeated at 10 pps and acoustic pulses are counted for 90 s. Hence 900 excitation beam pulses are shot for one sample. These results are plotted in Fig. 7.3. Next, the waveform of one acoustic pulse is recorded by the storage oscilloscope under the same experimental conditions. The recorded waveform is shown in Fig. 7.4. As discussed in detail latter, the first peak corresponds to the acoustic pulse, and those following are its echoes in the cell, the peak value of P_1 is the pulse height of the acoustic pulse. Then, the dependence of pulse height, that is the signal magnitude, on the power density at the beam waist of the excitation beam is measured, and the results are plotted in Fig. 7.5. The electric field intensity at the beam waist corresponding to the power density is also indicated on the upper horizontal axis of the figure. Finally, the breakdown thresholds of air, water and the ultrafine polystyrene particles in water are measured, and the results are listed in Table 7.1. This experiment is performed in a super clean room of class 100 (100 particles in a cubic foot, that is 5×10^{-3} particles per 1 mL of air).

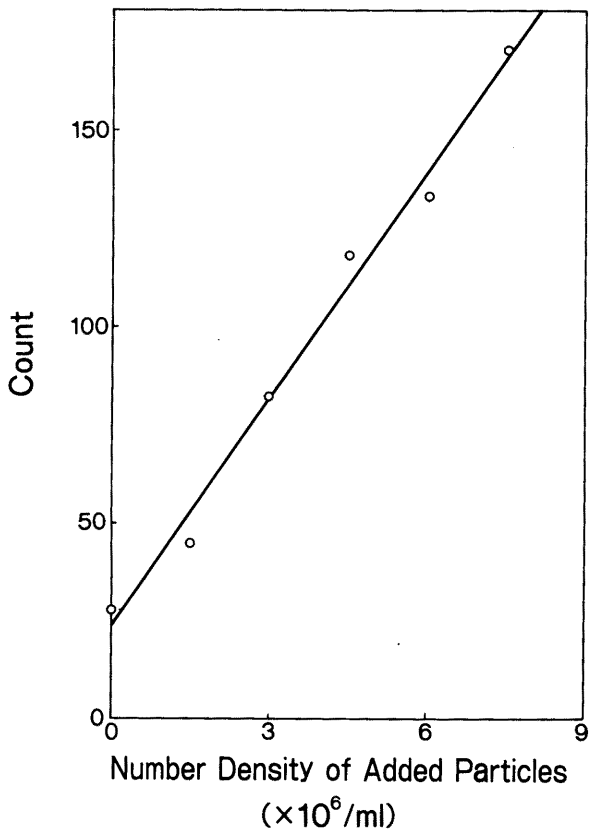

Fig. 7.3
Dependence of the acoustic pulse counts on number density for added 0.085 μm polystyrene ultrafine particles.

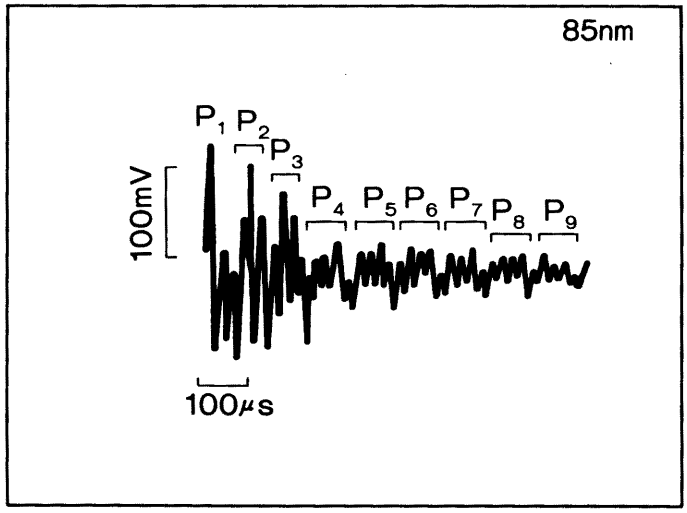

Fig. 7.4 Waveform of the breakdown acoustic signal from one 0.085 μm polystyrene ultrafine particle.

(c) Results and discussion

To verify the present counting principle in which particles are counted individually by detecting a laser breakdown acoustic pulse from one particle, it is essential to confirm that the detected acoustic pulse is indeed induced from one particle. Then, first, the detected acoustic pulses in the present experiment are confirmed to be generated from one polystyrene ultrafine particle added to ultrapure water. The increase in the acoustic pulse counts for 0.5 - 2.5 ppb of polystyrene turbid samples shown in Fig. 7.3 is proportional to the concentration, that is the number density. The increase in the acoustic pulse counts at the number density of 6.3×10^6 mL^{-1} is 98 counts. On the other hand, the theoretical expectation of the counts under the present experimental conditions is calculated with Eq. (7.2b) as 85 counts. The experimental result roughly agrees with the theoretical value corresponding to the particle number expectation in the beam waist of 0.1 particles per one shot of excitation beam. Therefore, from these results, generation and detection of the acoustic pulse for one particle is confirmed.

From the above discussion, the waveform recorded in Fig. 7.4 is the acoustic signal from a 0.085 μm polystyrene particle. Rather broad peaks P_2 - P_9 appear which have fine vibrational peaks on them. The frequency of the peaks P_2 - P_9 is 12.0 kHz, while the fine vibration frequency is 50.0 kHz. On the other hand, cell natural frequencies, obtained from the calculation method in Appendix B, are 15.5 kHz and 55.0 kHz for longitudinal and radial modes of the cell, respectively. Hence the frequencies of the peaks appearing in the waveform of Fig. 7.4 correspond well with the cell natural frequency; the slight difference between them is considered to be due to the effect of the sample inlet and outlet of the cell which deviates from the ideal cylindrical shape. Therefore, the first peak P_1 corresponds to the acoustic pulse and the following peaks P_2

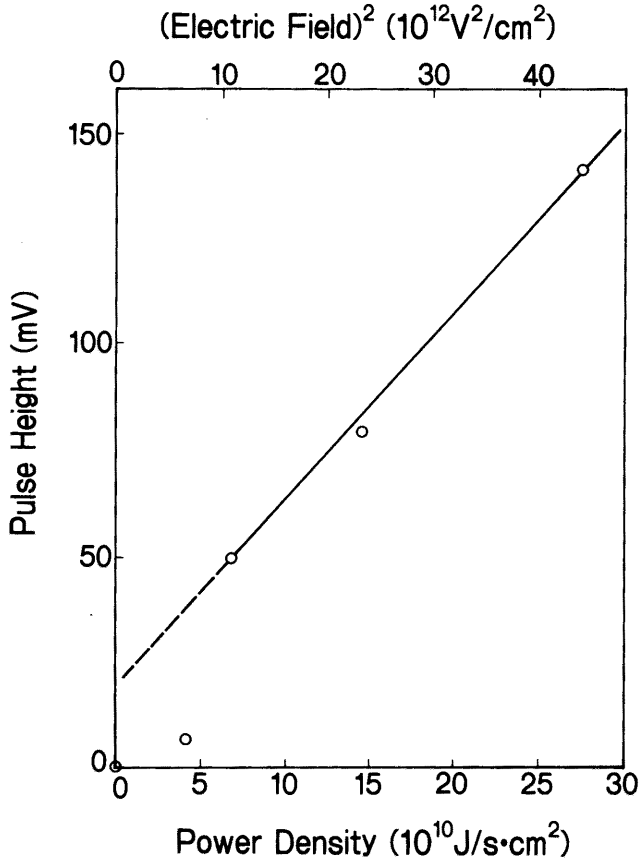

Fig. 7.5 Dependence of breakdown acoustic pulse height on power density of the excitation beam. The size of the polystyrene ultrafine particle is 0.085 μm.

Table 7.1 Breakdown threshold.

Materials	Breakdown threshold
Air	5×10^{12} W/cm^2
Water	3×10^{11} W/cm^2
Polystyrene (0.085 μm)	5×10^{10} W/cm^2

- P_9 are echoes of the acoustic pulse in the cell, hence the peak value of P_1 is the pulse height of the acoustic pulse.

The acoustic pulse height increases with increasing power density of the beam waist as shown in Fig. 7.5. At the power density of 4.4 - 7.0 × 10^{10} W/cm^2, the pulse height increases discontinuously, and it is proportional to the power density beyond that. The electric field intensity E_b of the laser field in the beam waist is given as (Mittleman, 1982),

$$E_b = 19.4\left(\frac{J}{\pi r_b^2 \tau_p}\right)^{\frac{1}{2}} \frac{1}{\varepsilon}$$

$$= 9.1\left(\frac{J}{\tau_p}\right)^{\frac{1}{2}} \frac{D_{op}}{F} \frac{n}{\lambda} \frac{1}{\varepsilon} \qquad (7.3a)$$

$$= 9.1\left(W_J\right)^{\frac{1}{2}} \frac{D_{op}}{F} \frac{n}{\lambda} \frac{1}{\varepsilon}, \qquad (7.3b)$$

where r_b is the spot size of the beam waist and W_J is the power density. Hence, the value of E_b for 4.4 - 7.0 × 10^{10} W/cm^2 of W_J at which the discontinuous increase of the acoustic pulse height appears is calculated as 2.8 - 3.8 × 10^6 V/cm, while the dielectric breakdown threshold of the polystyrene thin layer is reported as 2 - 3 × 10^6 V/cm (Hirakawa et al., 1984). Therefore, as the laser field intensity where the discontinuous increase of the acoustic pulse height appears corresponds well with the dielectric breakdown threshold of the polystyrene ultrafine particles, the discontinuous increase of the pulse height is considered to be due to laser breakdown of the particles. That is, the particle becomes plasma due to laser breakdown, and a strong acoustic pulse is emitted by the

optical absorption of the breakdown plasma and its explosive expansion. The breakdown plasma may be formed very early in the laser irradiation period, and throughout most of the laser irradiation period, laser-plasma interaction is considered to be the dominant interaction. Hence, absorbed optical energy by the plasma is proportional to the power density of the excitation beam pulse, resulting in the acoustic pulse height being proportional to the power density beyond the breakdown threshold as shown in Fig. 7.5.

The measurement of the dependence of the acoustic pulse counts on the particle number density shown in Fig. 7.3 is performed at the beam power of 0.55 mJ, corresponding to the power density of 7.0×10^{10} W/cm^2, which exceeds the breakdown threshold, hence the acoustic pulses detected in this experiment are breakdown acoustic pulses. Therefore, the principle of this novel counting method is verified. Breakdown acoustic signals of 10^1 - 10^2 mV can be easily counted with a good S/N ratio with the present experimental apparatus for which the noise level is restrained below 100 μV_{rms}. Furthermore, from the results of the measurement of breakdown threshold listed in Table 7.1, the air breakdown threshold is higher than those of water and polystyrene particles. Hence the beam power can be selected to induce particle breakdown and not air bubble breakdown, so that miscounting due to air bubbles can be avoided. In the practical use of a particle counter for liquids, fine air bubbles are often dispersed in liquids. This is especially so in ultrapure water due to a drastic pressure variation in the ultrafilteration process. The miscounting due to fine bubbles hinders accurate detection of particulate substances in the laser scattering method. Therefore, the present method using laser breakdown is expected to be a most useful tool for detection of ultrafine particles in liquids from the viewpoint of precise counting as well as the favorable detection limit particle size.

7.2 Counting of Ultrafine Particles in Ultrapure Water

In section 7.1, the principle of the proposed counting method of ultrafine particles in liquid was verified. In the experiment, concentration of the sample was prepared in the trace region of 0.5 - 2.5 ppb which corresponded to particle number density of 1.4 - 7.2 $\times$ 10^6 mL^{-1}. However, this value was rather dense in comparison with the number density of the ultrafine particulate impurities in ultrapure water, that is 10^1 - 10^2 mL^{-1}. In addition, the cell used was a closed type and the applicability of the present method to in-line measurement was not examined. Then, in this section, detection of ultrafine particles in ultradilute amount (10^2 particles/mL (mL^{-1})) by the present method is proved using 0.038 μm polystyrene ultrafine particles. In the experiment, a flow type cell is used and in-line measurements are demonstrated. Finally, dependence of pulse height on particle size is found, and the possibility of size distribution measurements is discussed.

(a) Counting efficiency

As shown in Fig. 7.3, in the previous experiment, the increase of acoustic pulse counts at the particle number density of 6.3 $\times$ 10^6 mL^{-1} was 98 counts for 900 excitation beam shots, and the result roughly agreed with the theoretical expectation given by Eqs. (7.2). From Eq. (7.2a), the expectation of the breakdown acoustic pulses for the particle number density of ultrapure water 10^2 mL^{-1} is estimated to be about 1.4 $\times$ 10^{-3}; this value means that the breakdown acoustic signal may be generated and detected 1.4 times for 9 $\times$ 10^5 shots of the excitation beam. In other words, when the repetition of the excitation beam is 10 pps, the excitation beam is shot at the particles and induces a breakdown acoustic pulse once every 25 hours. Such a count rate is not practical for

particulate impurity monitoring of ultrapure water. Then, in this subsection, proper experimental conditions including optical arrangement, which gives a practical counting rate, are investigated.

The particle counting efficiency η_c is defined as the ratio between the particle number density and counts of the breakdown acoustic signal, and is given as follows from Eq. (7.2b),

$$\eta_c = \frac{C_e}{N} = V_{op} f_p t. \tag{7.4}$$

It is rewritten as the function of optical parameters using Eq. (7.1) as,

$$\eta_c = 21.8\left(\frac{F}{D_{op}}\right)^4 \left(\frac{\lambda}{n}\right)^3 f_p t. \tag{7.5}$$

As is obvious from Eq. (7.4), the volume of the beam waist should be enlarged to increase the counting efficiency for the same beam source and measurement period. On the other hand, the power density W_J in the beam waist is given as

$$W_J = \frac{J}{\pi r_b^2 \tau_p}$$

$$= \frac{J}{\pi\left(1.2\dfrac{F}{D_{op}}\dfrac{\lambda}{n}\right)^2 \tau_p}, \tag{7.6}$$

hence the power density is also written as a function of the optical parameters. Equations (7.5) and (7.6) show that enlargement of the beam

waist to obtain large counting efficiency results in a decrease of the power density there, and the enlargement is restricted by the breakdown threshold power density. Hence, the proper optical arrangement can be determined with the given counting efficiency and the breakdown threshold power density from Eqs. (7.5) and (7.6).

In this experiment, a pulse YAG laser system of 30 mJ output at the second harmonics of 532 nm, pulse width of 10 ns, and repetition ratio of 20 pps is used as a beam source. For practical use, the counting efficiency should exceed about 0.1 for measurement period of 10^2 s, that is the breakdown acoustic signal counts becomes 10^1 for the particle number density of 10^2 mL^{-1}. On the other hand, the optical breakdown threshold of solids is on the order of 10^{10} - 10^{11} W/cm^2. Hence, the proper conditions of this experiment are obtained from the following relationships:

$$\eta_c > 0.1 ,$$

$$W_J > 10^{10} \ \ W/cm^2$$

Using the parameters of the beam source and Eqs. (7.5) and (7.6), the above relationships give the following condition for the optical arrangement,

$$7.4 \times 10^1 < \frac{F}{D_{op}} < 1.3 \times 10^2. \qquad (7.7)$$

The relationship of Eq. (7.7) is plotted in Fig. 7.6, and the applicable region to this experiment is indicated in the figure. From

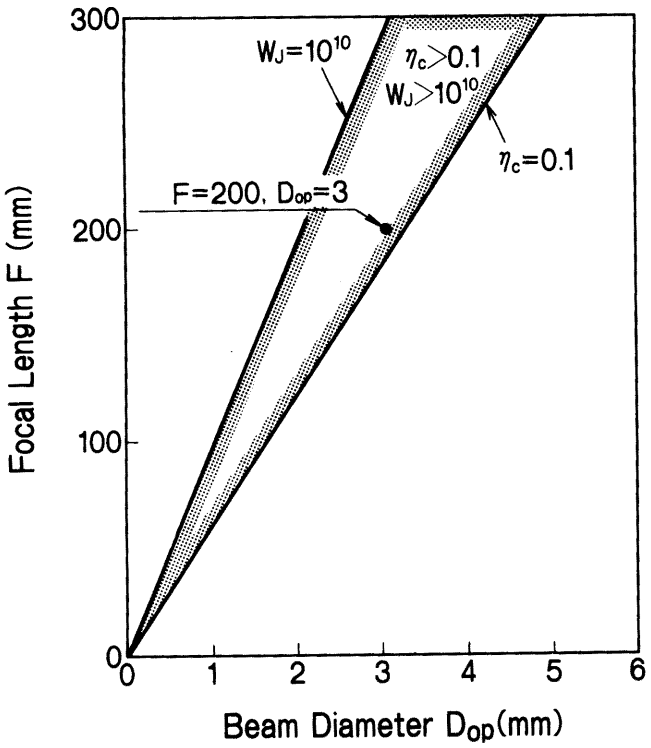

Fig. 7.6
Application region of the parameters for optical arrangement. The parameters used in the subsequent experiment are selected as F = 200 mm and D_{op} = 3 mm.

Table 7.2 Experimental conditions.

Symbol	Parameter	Value
	Excitation beam	
λ	Wavelength	532 nm
J	Power	30 mJ
τ_p	Pulse duration	10 ns
f_p	Repetition ratio	20 pps
	Optics	
F	Focal length	200 mm
D	Beam diameter	3 mm
	Sample	
-	Particle size	0.038 μm

Fig. 7.6, the parameters of the optical arrangement are chosen as 200 mm for the focal length and 3 mm for the beam diameter. Including these optical parameters, the experimental conditions are listed in Table 7.2. The counting efficiency under these conditions becomes 0.13 for 200 s.

(b) Experimental

The experimental setup is shown in Fig. 7.7. The fundamental structure is the same as the previous system in Fig. 7.2. However, the cell is a flow type PA cell shown in Fig. 6.2 to demonstrate in-line measurements, so the cell is set in the sample flow line. The signal processor is improved to allow recording of pulse height distribution as well as counting the acoustic pulses.

In the present experiment, as the samples are prepared in the ultratrace region of sub-ppt levels, sample preparation and measurements are performed with due care to prevent contamination. All experimental equipment is set up in a clean room of class 100, and all work, including sample preparation, is done in the clean room. All glass apparatuses are ultrawashed after the ordinary washing process to remove traces left from acidic washing. In ultrawashing, which is applied to semiconductor wafers to remove particulate impurities, the glass apparatus is dipped in a mixed solution of H_2O_2 and NH_4OH for ten min at 80°C. Particulate substances on the glass surface are removed by oxidation and vigorous bubble generation. With these countermeasures, contamination of the ultratrace samples from atmospheric dust and the experimental apparatus is prevented. Furthermore, the adsorption of the polystyrene ultrafine particles which are hydrophobic on the surface of the glass apparatus is avoided because the glass surface becomes hydrophilic on ultrawashing.

The 0.038 μm polystyrene ultrafine particles are dispersed in ultrapure water, and the water is used as sample. The number densities of

the samples are 300 - 1200 mL^{-1}, and the corresponding weight concentration is on the order of 10^{-2} ppt. The ultratrace samples are prepared by stepwise dilutions. An electron microscope examined turbid solution of 2000 ppm is diluted to 1 ppm by three dilution steps, and it is used as stock solution. More dilute samples are unsuitable as stock solutions because of coagulation due to lack of a surfactant. The samples are prepared by 6 - 7 dilution steps from the stock. In every dilution step, pipetting of less than 1 mL portions is avoided to minimize the dilution error.

First, the dependence of the counts on the number density of the added particles is measured. Each sample is run into the cell through the sample injector connected to the sample flow line as shown in Fig. 7.7, and the breakdown acoustic pulses are counted while the flow is running. After and between measurements, the flow of ultrapure water is not stopped to prevent particulate matter from remaining in the cell and to verify the in-line monitoring. The results are plotted in Fig. 7.8.

Second, the dependence of the pulse height distribution curve on the particle size is measured. The particle sizes of the ultrafine polystyrene particles are 0.038, 0.085, 0.22 and 0.33 μm. The number density of each solution is prepared as about 10^3 mL^{-1} by the same dilution procedure as described in the former experiment. These results are shown in Fig. 7.9.

(d) Results and discussion

From the results in Fig. 7.8, the counts of the breakdown acoustic signals increase in proportional to the number density of the added polystyrene ultrafine particles. Therefore, it is confirmed that polystyrene ultrafine particles of 0.038 μm can be counted at the ultradilute number density of the ultrapure water level. The count at the

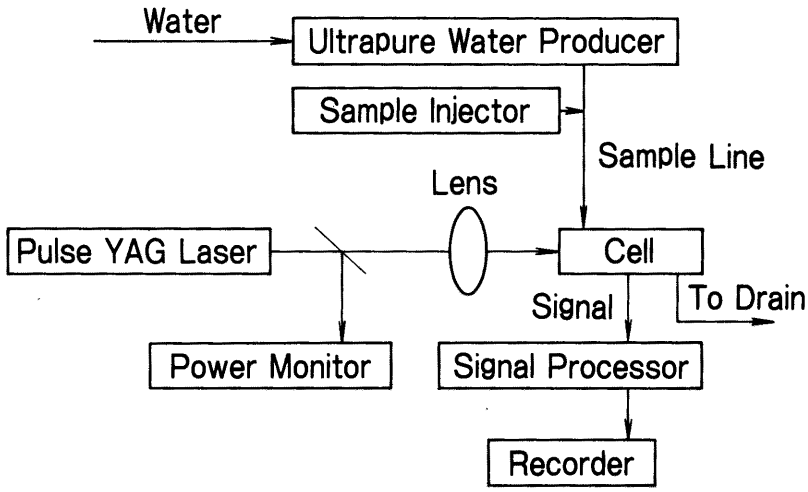

Fig. 7.7 A block diagram of the experimental apparatus for in-line measurements.

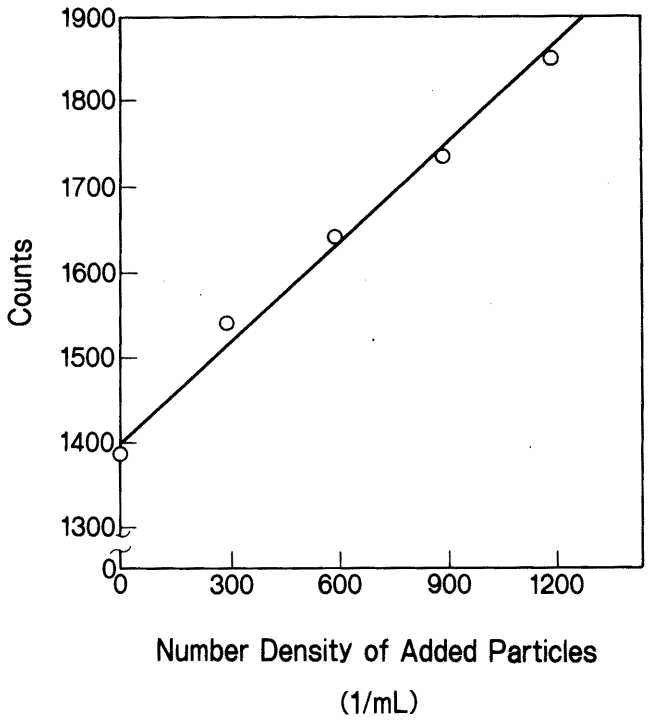

Fig. 7.8
Dependence of the breakdown acoustic pulse counts on the number density of the added 0.038 μm polystyrene ultrafine particles.

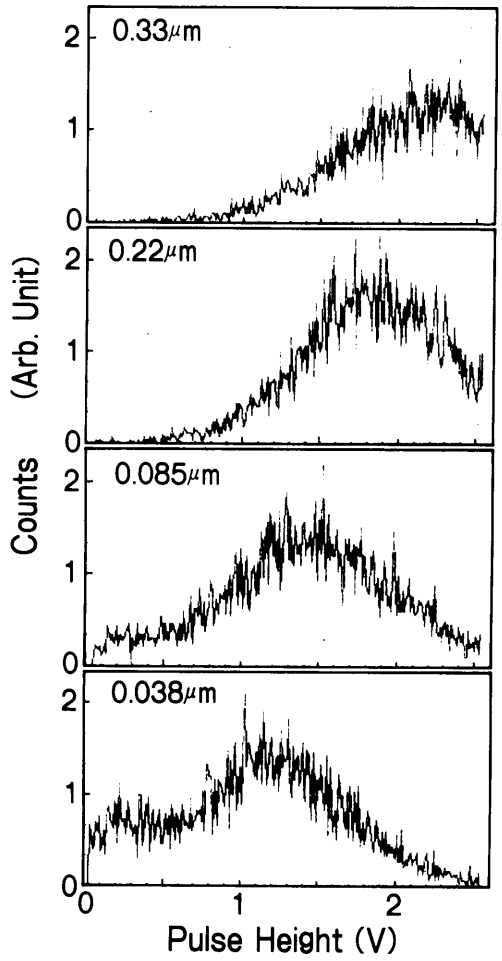

Fig. 7.9
Dependence of the pulse height distribution on the particle size.

blank considered to originate in the ultrafine particulate impurities in the ultrapure water itself, and their number density is estimated as 3.8×10^3 mL^{-1} from the counting efficiency discussed later.

The pulse height of the breakdown acoustic signal from the 0.038 μm polystyrene particle is on the order of 10^0 V as shown in Fig. 7.9, while the streaming noise is about 2 mV. Hence, the 0.038 μm polystyrene particles are counted very accurately while the sample is flowing, and smaller particles can be counted as well. These results shows that the detection limit size of the present method is at least one order smaller than that of the conventional laser scattering method, and it is applicable to in-line monitoring of ultrafine particles in ultrapure water and reagents.

The slope of the caliblation curve in Fig. 7.8 shows the counting efficiency, and it is obtained as 0.36, while the theoretical value is 0.13. The difference between the theoretical and experimental values cannot be explained clearly. However, approximation of the beam waist shape, which has a hyperboloidal plane, as a cylinder and the experimental error due to extremely high dilution in the sample preparation are considered as likely causes. It is difficult to prepare the ultradilute samples exactly that the reproducibility of the slope is not so good (over ±50 %), although the reproducibility of the pulse counts for the samples prepared in the same time is within the statistical error (±10 %) at the added particle number density of 10^2 mL^{-1}.

The pulse height distribution depends on the particle size as shown in Fig. 7.9, and the pulse height corresponding to the peak of the distribution curve is proportional to the particle size. Therefore, it is shown that sizing of the ultrafine particles from the pulse height is possible, so that size distribution can be obtained from measurements of pulse height distribution. However, the pulse height distribution curves spread broadly for monodispersed particles of uniform size, and the size resolution is not sufficient at present. The origin of the broadening is unknown. However, as the pulse height is proportional to the power density of the excitation beam, the spatial distribution of the power density in the beam waist due to its hyperboloidal shape and inhomogenous laser field distribution of the pulse YAG laser are guessed to be main factors. Hence development of a normalising method for the power density at the signal generation point for every breakdown should be considered as a means to sharpen the pulse height distribution curve for uniform size particles.

From the above discussions, the validity and applicability of the present method to in-line monitoring of ultrafine particles in liquids are

confirmed. A more precise evaluation of the beam waist and the signal correction method for improvement of the size resolution should be examined in subsequent studies. Furthermore, spectrochemical analysis of particle components using the breakdown plasma emission spectrum should also be examined. Breakdown acoustic spectroscopy is anticipated to be a useful and effective method for detection and characterization of ultrafine particles in liquids.

7.3 Conclusion

In Chapter VII, the mechanism of acoustic signal generation from microparticles was found to shift from thermal expansion of the medium to optical breakdown of the particles as the power density of the excitation beam increased. Then, a novel counting method of ultrafine particles in liquids using the breakdown acoustic effect was proposed. In the method, ultrafine particles were counted individually by counting the breakdown acoustic pulses generated from them. The detection condition and counting efficiency of the particles were investigated theoretically, and the design condition for counting the ultrafine and ultradilute particulate substances in ultrapure water level was obtained. Using 0.038 μm polystyrene ultrafine particles, particle counting at the number density of ultrapure water level (10^1 - 10^2 mL^{-1}) was demonstrated, and it was shown that the minimum detectable particle size was at least one order smaller than that of the conventional laser scattering method. The validity and applicability to in-line monitoring and size distribution measurement were also confirmed.

CHAPTER VIII CHARACTERIZATION OF NONRADIATIVE RELAXATION PROCESSES

The source term of the PA signal is thermal energy released to a medium. This thermal energy originates in various energy conversions and migration processes such as nonradiative relaxation, photochemical reaction, phase transition and so on, as shown in Fig. 2.1. Hence the PA signal has information about these energy conversions and migration times as well as their quantum yield which is seldom obtained by ordinary spectroscopical methods because of their nonradiative properties. Therefore, PAS has been expected to be an effective spectroscopic method to study these energy conversion and migration processes. Photoacoustic measurements of nonradiative relaxation time using phase shift have been studied in gas phase (Kaya et al., 1974, 1975; Parker and Ritke, 1973) and solid (Merkle and Powell, 1977) samples, and some theoretical approaches for solid samples have been reported (Mandelis et al., 1979; Quimby and Yen, 1980). However, little theoretical or experimental study in liquid samples has been performed, and there is still much left to study for them. One of the reasons for this situation is the lack of theoretical support for development of the methodology. The reported theoretical analyses for frequency characteristics of phase shift due to nonradiative relaxation time (Mandelis et al., 1979; Quinby and Yen, 1980) in solids cannot be applied directly to the liquid phase, since these theories are based on a single relaxation process, though the relaxation in liquid always has plural processes.

It was shown in Chapter II that the theory developed here clearly described the thermal process in which the optical energy is converted to the thermal energy, and the effect of the energy conversion and migration on the PA signal was expressed as the transfer function $D^f(\omega_0)$ which is the

Fourier image of the impulse response $D(t)$ corresponding to the energy conversion and migration. This theoretical description was applied to heat flow from turbid particles as a macroscopic energy migration, and its propriety was confirmed in Chapter V. Then in this chapter, the theory is applied to nonradiative relaxation as a microscopic energy migration in liquids, and the theoretical basis of methodology for measurement of nonradiative relaxation times is proposed.

First, the theoretical method for analyzing the energy migration process using $D^f(\omega_0)$ is applied to an ideal case where the nonradiative relaxation has only one process, and the propriety of the analytic method is examined from the comparison of the results with those obtained by Mandelis et al., (1978). In the next step, the method is applied to a more practical system in which the nonradiative relaxation has plural processes. The physical meaning of the theoretically obtained frequency characteristics of the phase shift is discussed, and the methodological basis for the characterization of the nonradiative relaxation time is proposed.

8.1 Relaxation through Single Process

First of all, the general description of the thermal process $D^f(\omega_0)$ obtained in section 2.2 is applied to a nonradiative relaxation through a single process. This is an ideal system and seldom takes place in liquids. The theoretical results are compared with reported ones which have been obtained from the same simple relaxation system, and the applicability of the present theoretical method is discussed.

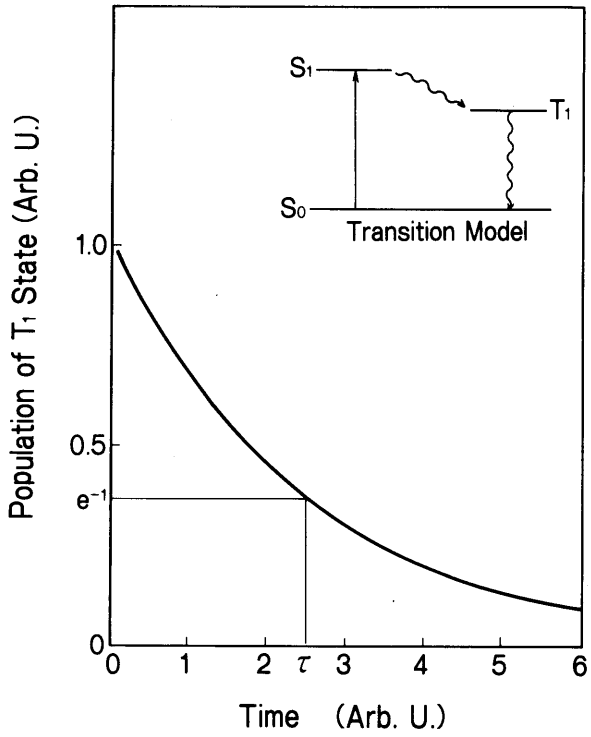

Fig. 8.1
A simple transition model in nonradiative process, and a decay curve of excited T_1 State.

(a) Impulse response and transfer function

As was discussed in section 2.2, the thermal process in PA signal generation can be analyzed by obtaining an impulse response function $D(t)$, and the characteristics of the PA signal are described by its transfer function $D^f(\omega_0)$. In particular, the phase shift of the PA signal due to energy conversion and migration time is obtained as an argument of $D^f(\omega_0)$ as shown in Eq. (2.23). Hence, the impulse response corresponding to a nonradiative relaxation process is obtained herein.

A simple transition model and time dependence of the population in the excited state T_1, that is, the decay curve of T_1, is shown in Fig. 8.1. In the transition model, only nonradiative processes are indicated. The relaxation times of S_1 and T_1^* which is the Frank-Condon state of T_1 are assumed to be short and the energy gap between S_1 and T_1 is assumed to be small. Under these assumptions, the relaxation process contributing to

the PA signal generation is the single process from T_1 to the ground state S_0. The decay curve for this type of relaxation is known to be a single exponential curve which is obtained from rate theory. The heat quantity migrating to the solvent is proportional to the number of molecules in relaxation, hence the time dependence of the thermal energy migration from the excited molecules to the solvent has the same profile as the decay curve. Therefore, as the excitation time from the S_0 to S_1 state is infinitesimal, the impulse response $D(t)$ is just the decay curve itself from the definition of $D(t)$. Hence the impulse response of the single relaxation process is given as

$$D(t) = a I_0 \eta_N \exp(-\frac{t}{\tau_N}). \tag{8.1}$$

where τ_N is the nonradiative relaxation time.

The transfer function $D^f(\omega_0)$ is given as a Fourier image of $D(t)$, and it is obtained from Eq. (8.1) as

$$D^f(\omega_0) = a I_0 \eta_N \frac{-i}{\omega_0 - \frac{i}{\tau_N}}. \tag{8.2}$$

Using Eq. (8.2), information about nonradiation relaxation such as quantum yield η_N and relaxation time τ_N can be obtained from the PA signal. In this study, the relationship between the phase shift of the PA signal and relaxation time τ_N is discussed.

On the other hand, in the theoretical model of heat generation due to transition which was given by Mandelis et al., (1979), the time dependent thermal energy migration to the medium was expressed as

$$\frac{d}{dt}H(\mathbf{r},\ t)=I(\mathbf{r},\ t)-\frac{1}{\tau_N}H(\mathbf{r},\ t). \tag{8.3}$$

This theoretical model considers in the time dependence of the decrease of population in the ground state by optical excitation, and it is a little more realistic than the former simple transition model. Assuming sinusoidal modulation of the excitation beam intensity, Eq. (8.3) is solved and the fluctuating part in the steady state is given as

$$H(\mathbf{r},\ t)=\frac{1}{1+i\omega_0\tau_N}\,\alpha I_0\eta_D M(t)R(\mathbf{r}). \tag{8.4}$$

In comparison with the general solution expressed in Eq. (2.7), the transfer function of this model is obtained formally as

$$D^f(\omega_0)=\frac{1}{1+i\omega_0\tau_N}\,\alpha I_0\eta_D. \tag{8.5}$$

In the next section, phase of the PA signal is obtained for both theoretical models from Eqs. (8.2) and (8.5) and it is compared to confirm the validity of the theoretical method.

(b) Results and discussion on phase shift and relaxation time

The phase of the PA signal due to energy conversion and migration in the thermal process is obtained as the argument of $D^f(\omega_0)$. An example application to macroscopic thermal flow from microparticles in liquids was examined in Chapter V. Now, the phase shift due to nonradiative relaxation time is deduced for both models discussed in the last sub-section.

The phase shift of the PA signal ϕ_D corresponding to the thermal process can be easily obtained as the argument of $D^f(\omega_0)$. For $D^f(\omega_0)$ of Eq. (8.2) obtained in the simple relaxation model, ϕ_D becomes

$$\phi_D = \arg D^f(\omega_0) = \tan^{-1} \frac{-\mathrm{Im}\{D^f(\omega_0)\}}{\mathrm{Re}\{D^f(\omega_0)\}}$$

$$= \tan^{-1} \omega_0 \tau_N. \qquad (8.6)$$

On the other hand, the phase of the PA signal obtained from Eq. (8.5) for the model of Mandelis et al., also takes the same form as Eq. (8.6). Therefore, the result obtained by the present theoretical method corresponds well with that obtained by the theoretical method of Mandelis et al. (1979). Furthermore, Eq. (8.6) also agrees with the relationship which has been widely used to measure radiative relaxation time by emission spectroscopy. The physical meaning of this relationship is that the phase shift of the signal represents the delay angle of the signal output versus excitation input due to the relaxation time.

The phase shift of the PA signal, due to nonradiative relaxation time, is thus obtained formally without returning to the basic wave equations, and the theoretical result of Eq. (8.6) agrees well with the widely used relationships in spectroscopy. Therefore, the propriety and applicability of the theoretical methodology, developed in the present study, to microscopic energy migration in liquids is confirmed. However, as mentioned at the beginning of this section, the basic model is an ideal model for confirmation of the theoretical method. More complicated processes which have plural relaxation processes contributing to PA signal generation are dealt with in the next section.

8.2 Relaxation through Plural Processes

The basic transition model for the obtained result, Eq. (8.3), is too simple for the analysis of actual relaxation phenomena in liquid phase. Generally relaxation in liquids involves many relaxation processes, and collisional processes make the energy migration more complicated. These processes also provide thermal energy to the medium and form the source term of the PA signal. In addition, not only the molecule of interest, but other molecules including solvent ones contribute to signal generation in this ultrasensitive spectroscopy as shown in Chapter IV, hence the nonradiative processes in relaxation outside those of interest also affect the phase shift of PA signals. Conventional theories of PAS do not deal with these complicated systems because the basic wave or elastic equations become more intricate. On the other hand, the linear property of the basic equations of Eqs. (2.1) and (2.2) certifies the additivity of the general solutions; that is in physical terms, the superimposition of the acoustic wave can be expressed by the simple sum of the general solutions. Therefore, the theoretical method developed in the present study is expected to be applicable to complicated relaxation processes.

In this section, the theoretical method using the transfer function $D'(\omega_0)$ is applied to the nonradiative relaxation which has plural processes, and an experimetal methodology for characterization of the nonradiative relaxation in liquids is proposed, based on the theoretical results.

(a) Frequency characteristics of phase shift

A general model of intra and inter molecular transitions is shown in Fig. 8.2. In this model, energy migration due to collisional processes is taken in account as well as internal energy conversions. All these nonradiative relaxations contribute to generation of the PA signal, that

is, the thermal energy originated in each relaxation process becomes the acoustic source term from a microscopic viewpoint. The source term of the PA signal can be understood as the superimposition of the acoustic source terms originating in these relaxation processes, although most of the relaxation times are short enough to be considered as simultaneous.

From the linearity of the basic wave equation of Eq. (2.2), the superimposition of the acoustic wave originated in these relaxation processes can be expressed as a sum of the general solutions of Eq. (2.8) corresponding to each process, and as follows:

$$P^f(\mathbf{r}, \omega_0) = \sum_j \eta\eta_{n,j} D^f_j(\omega_0) M^f(\omega_0) Q^f(\mathbf{r}, \omega_0)$$

$$= \eta \left\{ \sum_j \eta_{N,j} D^f_j(\omega_0) \right\} M^f(\omega_0) Q^f(\mathbf{r}, \omega_0), \tag{8.7}$$

where j means the j-th relaxation process. Therefore, the transfer function of the total system $D^f_{total}(\omega_0)$ is obtained as

$$D^f_{total}(\omega_0) = \sum_j \eta_{N,j} D^f_j(\omega_0). \tag{8.8}$$

On the other hand, in a strict sense, the decay curves of these relaxation processes have a peak as shown in Fig. 8.3, because all excited states but the first one have no population at $t = 0$. Hence, these decay curves have a peak due to a double exponential curve corresponding to increase (from $j-1$ process) and decrease (to $j+1$ process) of the population of the j-th excited state. This type of decay from the excited state is well studied, and the decay curve is expressed by the following rate equation having double exponential terms (e.g. Lamarsh, 1974):

$$\frac{d}{dt} N_j = \lambda_{j-1} N_{j-1} - \lambda_j N_j \tag{8.9}$$

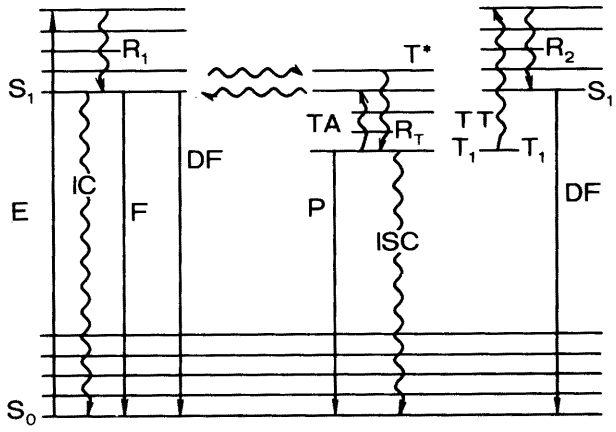

Fig. 8.2 Intra and inter molecular transition model. Nonradiative processes are indicated by wavy lines and the radiative ones are indicated by straight lines. E is optical excitation; R_1, R_2, and R_T, vibrational deexcitation; IC, internal conversion; ISC, inter-system crossing; TA, thermal reactivation; TT, T-T annihilation reactivation; F, fluorescence; DF, delayed fluorescence; and P, phosphorescence.

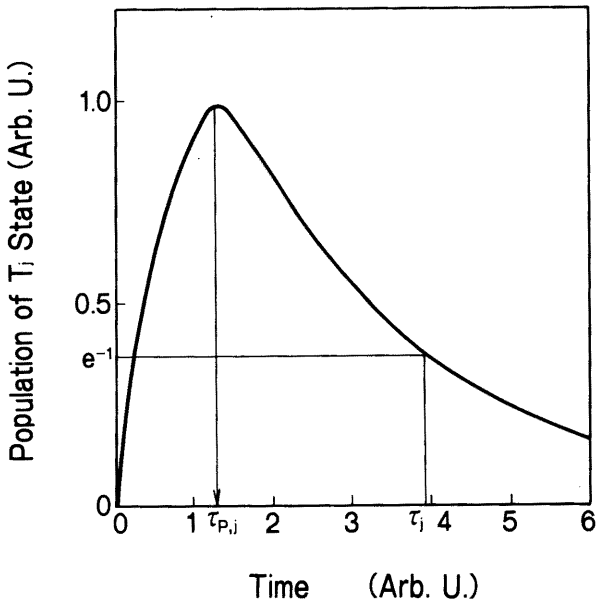

Fig. 8.3
Decay curve of excited T_j state. The time corresponding to the peak is given by Eq. (8.10).

where N_j is the population of the j-th excited state and λ_j is the decay constant of the relaxation process from the j-th state, that is, the j-th relaxation process. Equation (8.9) is easily solved with the initial condition that the population of both excited states is zero at $t = 0$, and the time $\tau_{p,j}$ giving the peak of the decay curve for the j-th relaxation process becomes,

$$\tau_{p,j} = \frac{\tau_j \tau_{j-1}}{\tau_{j-1} - \tau_j} \log \frac{\tau_{j-1}}{\tau_j} \tag{8.10}$$

where τ_j is relaxation time of the j-th process.

As discussed in the former section, the impulse response function corresponds to the decay curve, hence the impulse response function of the j-th relaxation process $D_j(t)$ is given as the time dependent population described by Eq. (8.9), and schematically shown in Fig. 8.3. When the decay curve in the time region close to its peak is roughly approximated with Lorentzian, the impulse response $D_j(t)$ and its transfer function $D^f_j(\omega_0)$ become:

$$D_j(t) = \frac{1}{\pi} \frac{\Delta\tau_{p,j}}{(t-\tau_{p,j})^2 + \Delta\tau^2_{pj}} \alpha I_0 \eta_{N,j} \tag{8.10}$$

$$D^f_j(\omega_0) = \alpha I_0 \eta_{N,j} \frac{1}{\pi} \int_{-\infty}^{\infty} \frac{\Delta\tau_{p,j} e^{-i\omega_0 t}}{(t-\tau_{p,j})^2 + \Delta\tau^2_{p,j}} dt$$

$$= \alpha I_0 \eta_{Nj} \Delta\tau_{p,j} \frac{1}{\pi} e^{-i\omega_0 \tau_{p,j}} \int_{-\infty}^{\infty} \frac{e^{-i\omega_0 t}}{t^2 + \Delta\tau^2_{p,j}} dt$$

$$= \alpha I_0 \eta_{Nj} \Delta\tau_{p,j} \frac{1}{\pi} e^{-i\omega_0 \tau_{p,j}} 2\pi i \,\mathrm{Res}(\tau_{p,j})$$

$$= \alpha I_0 \eta_{N,j} \exp(-i\omega_0 \tau_{p,j} - \Delta\tau_{p,j}\omega_0) \tag{8.11}$$

where Res(x) means the residue of x, and $\Delta\tau_{p,j}$ is the full width at the half maximum of the Lorentzian. Therefore, the transfer function of the total relaxation system is obtained from Eqs. (8.8) and (8.11) as follows,

$$D^f_{total}(\omega_0) = \sum_j \alpha I_0 \eta_{N,j} \exp(-i\tau_{pj} - \Delta\tau_{p,j})\omega_0. \tag{8.12}$$

In the case when the relaxation time of one relaxation process is sufficiently longer than the others as is often observed in relaxation from T_1 level, then the relationship

$$\Delta\tau_{p,j} < \tau_{p,j} \ll \tau_{p,1} \tag{8.13}$$

is valid, and the imaginary part and the real part of Eq. (8.12) are approximated as

$$\mathrm{Im}\{D^f_{total}(\omega_0)\} = -\alpha I_0 \eta_{N,1} \sin\omega_0 \tau_{p,1}, \tag{8.14}$$

$$\mathrm{Re}\{D^f_{total}(\omega_0)\} = \alpha I_0 \eta_{N,1} \cos\omega_0 \tau_{p,1} + \sum_{j\neq 1} \alpha I_0 \eta_{N,j}, \tag{8.15}$$

where $\tau_{p,1}$ is defined as the peak time corresponding to the longest relaxation time. Hence, the phase of the PA signal is obtained as

$$\Phi_D = \tan^{-1} \frac{-\mathrm{Im}\{D^f_{total}(\omega_0)\}}{\mathrm{Re}\{D^f_{total}(\omega_0)\}}$$

$$= \tan^{-1} \frac{\sin\omega_0 \tau_{p,1}}{\cos\omega_0 \tau_{p,1} + \Gamma}, \tag{8.16}$$

$$\Gamma = \frac{1}{\eta_{N,1}} \sum_{j \neq 1} \eta_{N,j} \tag{8.17}$$

The constant Γ means the ratio between the quantum yield of the relaxation process having the longest relaxation time and the total yield of the others. Therefore, the frequency characteristics of phase ϕ_D for the relaxation which is composed of plural relaxation processes is shown by Eq. (8.16).

The results of the numerical calculation of Eq. (8.16) with $\tau_{pj} = 2.1 \times 10^{-4}$ s are plotted in Fig. 8.4.

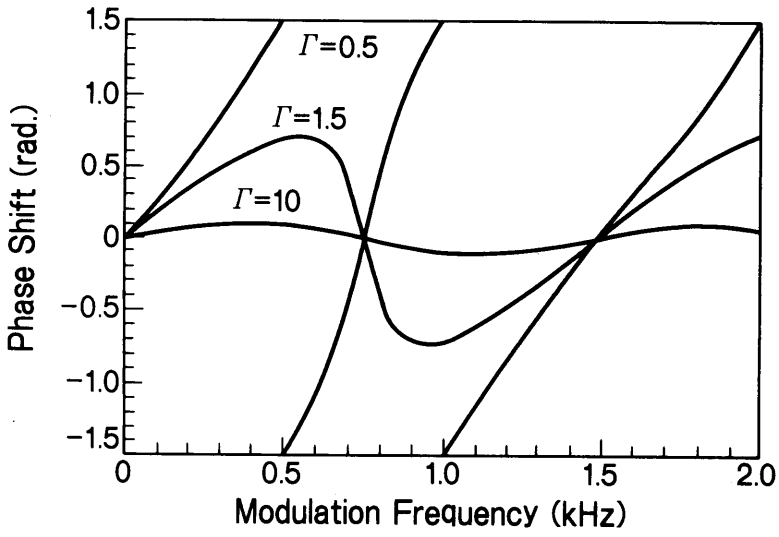

Fig. 8.4 Frequency characteristics of the phase ϕ_D, which correspond to the j-th process in the plural relaxation processes and are calculated from Eqs. (8.16) and (8.17). The conditions giving the phase zero point at which the three curves cross are shown in Eqs. (8.18) and (8.19).

(b) Results and discussion

Using the theoretical results obtained in the last sub-section, the theoretical basis of the methodology for characterization of nonradiative relaxation which is composed of plural relaxation processes is examined here. In the results of the calculation shown in Fig. 8.4, the three curves corresponding to Γ = 0.5, 1.5 and 10 cross at the same point on the phase zero line. The conditions giving this crossing point, named herein as the phase zero point, can be easily obtained from Eq. (8.16), and are as follows,

$$\omega_{0,n}\tau_{p,1}=n\pi \qquad n=1, 2, 3, \tag{8.18}$$

$$\tau_{p,1}=\frac{1}{2f_{0,1}} \tag{8.19}$$

where $\omega_{0,n}$ and $f_{0,n}$ mean the frequencies at n-th phase zero point. Therefore, the peak time of the decay curve which has the longest relaxation time can be obtained from Eq. (8.19) by measuring the modulation frequency at the first phase zero point.

The physical meaning of these phase zero points is interpreted as follows: the generated PA signal is the superimposed acoustic wave of two components which originate from all the fast relaxation processes and from the lowest one. When the delay of the PA signal corresponding to the latter one satisfies the relation of Eq. (8.18), the superimposition of both PA signals becomes synchronous without phase shift, and the phase of the superimposed PA signal corresponds perfectly to one which originates in the fast relaxation processes.

In many cases, the excited triplet state T_1 in Fig. 8.2 has a relatively long relaxation time, hence the decay curve having the longest relaxation time corresponds to the relaxation process from the T_1 state.

As the T_1 state has this long relaxation time, then, in some cases, excited molecules in T_1 transit to other state owing to inter molecular interactions such as thermal reactivation (Parker and Hachard, 1964; Baudin, 1930) and T - T annihilation from collision between excited molecules in T_1 state shown in Fig. 8.2 (Förster and Kasper, 1955). In these reactivation processes, the apparent relaxation time to the T_1 state characterizes these singular transitions. As $\tau_{p,1}$ for the decay curve of the T_1 state can be obtained with the present method, these characteristic apparent relaxation times in the reactivation processes can be estimated from the relationship of Eq. (8.10), when the relaxation time τ_1 is obtained from other spectroscopical methods such as phosphorescence measurement. Therefore, the present methodology is expected to be a unique characterization method for complicated relaxation processes in the condensed phase.

In experiments based on this methodology, it is difficult to obtain the phase zero point because of the background phase ϕ_Q due to propagation of the PA signal. Then, another method to obtain the phase zero point can be proposed from the definition of Γ in Eq. (8.17). As shown in Fig. 8.4, the phase zero points do not change for different values of parameter Γ. Hence, the crossing points of these frequency characteristics curves do not change when the background phase ϕ_Q is added to the phase ϕ_D due to the relaxation time, because the background phase originates in the propagation properties of the PA signal and is not affected by the thermal processes. Ordinarily, the parameter Γ is determined by the quantum efficiency of each relaxation processes, and it does not change for the same molecule under the same conditions, hence the value of Γ cannot be changed for the sample of which component is only one chemical species. However, an apparent value of Γ can be controlled by adding other molecules to the sample. In the case when several components exist in the

same sample, all the components contribute to PA signal generation, moreover, the superimposition of the PA signals from each component is still valid due to the linearity of the wave equation of Eq. (2.2). Therefore, the transfer function of this multi-component system is given as

$$D^f_{total}(\omega_0) = \sum_{i,j} \eta_{N,ij} D^f_{ij}(\omega_0) \tag{8.20}$$

where $\eta_{N,ij}$ and D^f_{ij} are the quantum efficiency and impulse response function for the j-th relaxation process of the i-th component. In order to simplify the theoretical approach, a two component system is considered in here. The first component is assumed to be the molecule of interest, which is noted by $\tau_{N,j}$, $\eta_{N,j}$ and $D^f_j(\omega_0)$ as is discussed with Eqs. (8.8) - (8.19), and the other is an additive for assistance in the measurements and is noted with i = 1 in Eq. (8.20), then $D^f_{total}(\omega_0)$ is written as

$$D^f_{total}(\omega_0) = \sum_j \eta_{N,j} D^f_j(\omega_0) + \sum_j \eta_{N,1j} D^f_{1j}(\omega_0). \tag{8.21}$$

When all the relaxation times in the added molecule are fast, analogous with the process to obtain Eqs. (8.14) and (8.15), the imaginary and real parts of $D^f_{total}(\omega_0)$ are deduced as

$$\mathrm{Im}\{D^f_{total}(\omega_0)\} = -\alpha I_0 \eta_{N,1} \sin\omega_0 \tau_{p,1}$$

$$\mathrm{Re}\{D^f_{total}(w_0)\} = \alpha I_0 \eta_{N,1} \cos\omega_0 \tau_{p,1} + \sum_{j\neq 1} \alpha I_0 \eta_{N,j} + \sum_j \alpha_1 I_0 \eta_{N,1j} \,. \tag{8.22}$$

Hence the phase ϕ_D is expressed by the same form of Eq. (8.16), however the expression of Γ is altered as

$$\Gamma = \frac{1}{\eta_{N,1}}\left(\sum_{j\neq 1}\eta_{N,j} + \frac{\alpha_1}{\alpha}\sum_{j}\eta_{N,1j}\right)$$

$$= \frac{1}{\eta_{N,1}}\left(\sum_{j\neq 1}\eta_{N,j} + \frac{\alpha_1}{\alpha}\right). \qquad (8.23)$$

Therefore, the value of Γ can be controlled by changing the concentration of the added molecule which contributes to the sample absorption coefficient α_1. From the above discussion, two frequency characteristic curves for different Γ values can be obtained by changing the concentrations of the molecule of interest or added one, which correspond to α or α_1, and the crossing point corresponding to the phase zero point can be refined. As a result, characterization of the nonradiative relaxation becomes possible. It is possible to replace the added molecule with solvent molecule, and then, α_1 becomes α_b. In this case, Γ can controlled by changing the concentration of the molecule of interest.

Physical meanings of this method are given as follows: the relative signal magnitude of the PA signals which corresponds to all the fast relaxation processes having no delay from the beam modulation and the slowest relaxation process can be varied by changing the concentration of the added molecule. Therefore, the waveform of the superimposed PA signal corresponding to both processes is changed, and consequently, the frequency characteristics of the phase are also changed. However, when the phase shift of the PA signal corresponding to the delay of the slowest process from the PA signal of the fast one satisfies the relation of Eq. (8.18), both PA signals are superimposed on each other synchronously without apparent phase shift. Therefore, the phase of the PA signal is independent of the magnitude of both PA signal components, because the two components of the PA signal are superimposed on each other on their nodes.

Consequently, the theoretical basis for the methodology of the characterization of nonradiative relaxation processes can be deduced from the general theory developed in Chapter II , and the experimental methodology is also examined theoretically. Photoacoustic spectroscopy is expected to be an effective tool to obtain information which is not provided by ordinary spectroscopical methods.

8.3 Conclusion

In the present chapter, the general theory developed in Chapter II was applied to analyze the relation between the phase of the PA signal and nonradiative relaxation time. The transfer function $D'(\omega_0)$ was shown to correspond to the decay curve of the excited state, and the phase shift of the PA signal due to this microscopic energy migration was obtained formally as the argument of $D'(\omega_0)$. This theoretical method was first applied to an ideal relaxation phenomenon which had only one relaxation process, and the propriety of the present theoretical method was confirmed from comparison of the theoretical result obtained here and in the literature. Secondly, this method was applied to analyze a more complicated system which had plural relaxation processes. The theoretical result showed the existence of the phase zero point in frequency characteristics of the phase, at which the phase became zero independently of the sample concentration and quantum efficiency. The physical meaning of the phase zero point was explained as the synchronous superimposition of the PA signals from fast and slowest relaxation processes without phase shift. The measurement method of the time giving the peak of the decay curve of the excited states and characterization of the relaxation processes using the phase zero points were proposed. Thus, the basis of

an experimental methodology for characterization of nonradiative phenomena which has seldom been realized by conventional emission spectroscopy was theoretically established.

CHAPTER IX CONCLUDING REMARKS

In the present study, the basic theory of PAS for the liquid phase, which has not been well studied, was established. The properties of the PA signal such as signal magnitude and phase, and the characteristics of PAS such as sensitivity and detection limit were clarified by the theory. The theoretical results were applied to development of various analytical chemical and spectroscopic applications. First, based on this generalized theory, an optimization method for PAS instrumentation including an ultrasensitive and wide dynamic PA cell design method was developed. An ultrasensitive PAS system was realized which enabled determination of ultratrace substances in sub-ppt levels. In addition, such novel application methods as characterization of turbid solutions were proposed on the basis of the general theory, and they were successfully carried out. As a further development of the theoretical and experimental methodology, novel methods for ultrasensitive immunoassay, and ultrafine particle counting were proposed and demonstrated experimentally, and a characterization method for nonradiative relaxation phenomena was theoretically examined. The theoretical and experimental results obtained in the present study are briefly summarized as follows.

In Chapter II, the PA effect was described with a generalized linear transform equation and wave equation of thermally forced motion which represented the energy conversion process from optical energy to thermal energy (thermal process) and acoustic signal generation and propagation (acoustic process), respectively. This coupling equation was solved using linear response theory and Green's functions. The theoretical results showed that the thermal process was described mathematically by the transfer function $D^f(\omega_0)$ which was a Fourier image of impulse response

function $D(t)$ for energy conversion, and the acoustic process was expressed by $Q(\mathbf{r},t)$ which was a convolution between the source profile and the propagator given as the Green's functions. The properties of the PA signal related to the thermal process, which included energy conversion and migration such as nonradiative relaxation and thermal diffusion, could be analyzed from $D'(\omega_0)$, and were applied to the analytical chemistry and spectroscopic applications in later chapters. On the other hand, the acoustic properties of the PA signal could be analyzed with $Q(\mathbf{r},t)$, and they were used for instrumentation. The signal detection and recovery method in PAS was also discussed based on the theory, and the physical meanings of the detected PA signals were clarified. The methodological difference between CW, pulse and correlation PAS was discussed theoretically, and it was shown that these methods were substatially identical. Finally, the propriety of the general theory was confirmed by comparisons between theoretical and measured results of frequency characteristics of PA signals.

In Chapter Ⅲ, instrumentation of the PAS system was discussed from analyzing $Q(\mathbf{r},t)$. First, dependence of the PA signal magnitude on geometrical conditions of a cylindrical direct coupling cell was analyzed, and the theoretical result was experimentally confirmed. In this theoretical and experimental study, the dominant factor which determined the acoustic source profile was clarified to be the thermal lens effect, not thermal diffusion which is the dominant factor in solid and gaseous PAS. From the results of the signal magnitude analysis, the optimal design method for an ultrasensitive and wide dynamic range PA cell was deduced, and appropriate conditions of beam modulation and phase sensitive detection were obtained. With this optimization method, an ultrasensitive PAS system was designed. From the results of the system efficiency test, the sensitivity was improved more than one order in comparison with the

ordinary PAS system, and the lower detection limit of the absorption coefficient reached 10^{-8} cm^{-1}, hence the availability of the present design method was verified.

In Chapter Ⅳ, the developed ultrasensitivity of PAS was applied to ultratrace determination. First, the theory of PA determination was developed on the basis of the general theory. The characteristics of sensitivity, dynamic range, and determination limit were clarified theoretically, and it was shown that the determination limit closely reached the basic limit of colorimetric determinations, which was dominated by solvent absorbancy. In the experimental verification of the ultratrace PA determination theory, cobalt in aqueous solution was extracted into *m*-xylene solvent using nitroso-naphthol reagent, and sub-ppt level determinations were demonstrated. The importance of background reduction and stabilization was pointed out for this ultrasensitive colorimetric determination.

In Chapter Ⅴ, PAS was applied to characterization of turbid solutions. First, the PA signal from microparticles in liquids was theoretically analyzed using the general theory. On the basis of the theoretical findings, using the phase shift of the PA signal due to the heat release time of the particles, a unique sizing and measurement method for thermal constants of the particles such as the heat transfer coefficient were proposed, as well as the ultratrace determination in which the sensitivity was independent of the particle size. The proposed sizing and characterization method was proved experimentaly using polystyrene turbid solutions.

In Chapter Ⅵ, a remarkable size dependency of sensitivity in PA determination of turbid solutions was found, though no size dependency was noted earlier. A resonant increase in the sensitivity appeared only when the particle size corresponded to the excitation beam wavelength, and its

physical meaning was guessed to be resonant dielectric loss in the particles, which was accompanied by resonant light scattering, from the obtained size dependency of the absorption cross-section. The sensitivity characteristics found were applied to the latex agglutination immunological determination method, and PIA was proposed. In PIA, the latex particles which were coated by antibody/antigen and added to sample serum were controlled to agglutinate through a immunological reaction to the size corresponding to the excitation beam wavelength, and antigen/antibody was determined from the PA determination of the latex agglutinations for which concentration was proportional to the antigen/antibody concentration. From the sensitivity characteristics of PAS, the latex agglutination could be determined ultrasensitively and selectively from other particulate impurities of biological substances or unreacted latex particles, making ultrasensitive determination of antigen/antibody possible. The principle of the proposed PIA was verified by the determination of trace rheumatoid factor as sample antigen. The lower determination limit was shown to be at least two to three orders lower than that of the conventional method using turbidimetry, and the possibility for determination of ultratrace cancer marker antigens was noted.

In Chapter VII, the mechanism of acoustic signal generation from microparticles was found to shift from thermal expansion of the medium to optical breakdown of the particles as the power density of the excitation beam increased. Then, a novel detection method of ultrafine particles in liquids using the breakdown acoustic effect was proposed. In the present method, ultrafine particles were counted individually by counting the breakdown acoustic pulses generated from them. The detection condition and counting efficiency of the particles were investigated theoretically, and the design condition for counting the ultrafine and ultradilute particulate substances in ultrapure water level was obtained. Using 0.038 μm

polystyrene ultrafine particles, particle counting at the number density of ultrapure water level (10^1 - 10^2 mL^{-1}) was demonstrated, and it was shown that the minimum detectable particle size was at least one order smaller than that of the conventional laser scattering method. The validity and applicability to in-line monitoring and size distribution measurement were also confirmed.

In Chapter VIII, the general theory developed in Chapter II was applied to analyze the relation between the phase of the PA signal and nonradiative relaxation time. The transfer function $D'(\omega_0)$ was shown to correspond to the decay curve of the excited state, and the phase shift of the PA signal due to this microscopic energy migration was obtained formally as the argument of $D'(\omega_0)$. This theoretical method was first applied to an ideal relaxation phenomena which had only one relaxation proces, and the propriety of the present theoretical method was confirmed from comparison of the theoretical result obtained here and in the literature. Secondly, this method was applied to analyze a more complicated system which had plural relaxation processes. The theoretical result showed the existence of the phase zero point in frequency characteristics of the phase, at which the phase became zero independently of the sample concentration and quantum efficiency. The physical meaning of the phase zero point was explained as the synchronous superimposition of the PA signals from the fast and slowest relaxation processes without phase shift. The measurement method of the time giving the peak of the decay curve of the excited states and characterization of the relaxation processes using the phase zero points were proposed. Thus, the basis of an experimental methodology for characterization of nonradiative phenomena which has seldom been realized by conventional emission spectroscopy was theoretically established.

From the theoretical and experimental results developed in the present study, various unique applications were shown and demonstrated as in

addition to ultrasensitive measurements. This multi functional property of PAS developed here is expected to be applied in various fields of basic research and applied engineering. For extensive practical application of PAS, some subjects remain, such as size and cost of the PAS system which are mainly due to the beam source. However, these problem are expected to be worked out by applying a semiconductor laser as a beam source. In fact, the second step in development of PAS, aiming at practical applications has began in the author's laboratory, following on the present basic research of PAS. Therefore, the present study is expected to form the basis for instrumentation and analytical chemistry and spectroscopic applications leading to commercial level development.

Some interesting problems in basic research on PAS have been pointed out in this work. For example, clarification of the physical meanings of the resonant increase of sensitivity found in Chapter VI can possibly provide new knowledge about laser-microparticle interactions. Furthermore, together with acoustic measurements of the laser breakdown shown in Chapter VII, the spectrochemical analysis of ultrafine particles using breakdown plasma spectra should revolutionize analytical methods dealing with these particles. Using its multifunctional properties, PAS should be able to give unique information. For example, as shown in Chapters V and VIII, PAS can determine the quantity of the absorbed optical energy by particulate samples, and also can characterize microscopic energy migration times. Hence, simultaneous measurement of PA signal magnitude and phase of particulate semiconductor photocatalyzers should give information about the quantity of absorbed optical energy and its migration processes including photochemical reactions, which are seldom obtained by ordinary spectrophotometric measurements. Thus, the theoretical and experimental methodology developed in the present study is also expected to promote more basic research.

ACKNOWLEDGEMENTS

The author expresses his sincere and hearty appreciation to Prof. Yohichi Gohshi and Prof. Tsuguo Sawada of the University of Tokyo for their continual guidance and stimulating supervision throughout the present study, for their useful advice and enlightening criticism on the methods of the research, and for their careful reading of the manuscript. The author is also deeply grateful to Prof. Yoshimasa Nihei, Prof. Akira Fujishima and Prof. Kohichi Kitazawa for their usuful discussions and advices.

The author also wishes to express his sincere appreciation to Dr. Norihiko Ozaki, Dr. Kazumichi Suzuki, Dr. Masaharu Sakagami, and Dr. Shunsuke Uchida of Energy Research Laboratory, Hitachi, Ltd., and Mr. Masaaki Fujii of Hitachi Nuclear Engineering Co., Ltd. for their useful discussions, guidance and encouragement.

The author is deeply grateful to Dr. Kenji Motojima for his enlightening guidance on analytical chemistry, and also Dr. Takashi Okazaki for his valuable discussion on the theoretical parts.

The author would like to express hearty thanks to Dr. Kaoru Taniguchi, and Dr. Shuji Yamada, of Hitachi, Ltd., Dr. Akira Doi, and Dr. Hideo Yusa of Energy Research Laboratory, Hitachi, Ltd., for guidance and encouragement throughout this work.

The author is deeply indebted to all his colleagues in the Department of Industrial Chemistry, University of Tokyo, and his associates in the laser spectroscopy research group in Energy Research Laboratory, Hitachi, Ltd. for their expertise and cooperation in realizing the experimental parts of the present study.

The author greatly thanks Dr. Carol Kikuchi for her comments on the English of this thesis. Finally, thanks are also due to the author's wife Hatsumi Kitamori for her sacrificing support throughout the present study.

APPENDICES

Appendix A: Normalizing of Distribution Functions

As the functions $R(\mathbf{r})$ and $M(t)$ mean the spatial and time distribution functions of the excitation beam, they must be normalized. The spatial distribution $R(\mathbf{r})$ is normalized as

$$\int_{\mathbf{r}} k_1 R(\mathbf{r})\, d\mathbf{r} = 1 \qquad \text{(A.1)}$$

and the time distribution $M(t)$ satisfies

$$\int_0^{t_0} k_2 M(t)\, dt = k t_0 I_0, \qquad \text{(A.2)}$$

where t_0 is the measurement time, and k_1, k_2, and k are proportionality constants. The relation of Eq (A.2) means that the total optical energy given to the system is proportional to the output energy of the beam source.

The normalizing methods of Eqs. (A.1) and (A.2) are applied to the Gaussian beam profile and rectangular modulation in section 2.5. For the Gaussian beam, Eq. (A.1) becomes

$$\int_0^{2\pi} \int_0^{\infty} k_1 e^{-(2r^2\gamma^2 / r_0^2)}\, r\, dr\, d\theta = 1 \qquad \text{(A.3)}$$

hence the normalizing factor k_1 is obtained as

$$k_1 = \frac{4r^2}{r_0^2} \qquad \text{(A.4)}$$

On the other hand, the integral of the rectangular modulation function written by Heaviside functions of Eq. (2.26) is equal to the area of the rectangular pulses shown in Fig. A.1, hence Eq. (A.2) becomes

$$k_2 f t_0 = k t_0 I_0,$$

and the normalizing factor k_2 is obtained as

$$k_2 = \frac{k}{f} I_0 \qquad \text{(A.5)}$$

Equation (A.5) means that the photon number in one rectangular pulse is inversely proportional to the modulation frequency, because the power of the beam source is constant.

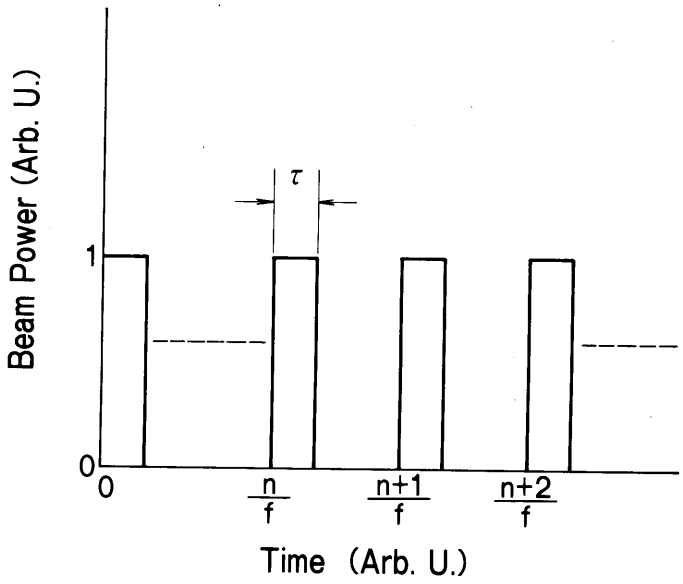

Fig. A.1
A rectangular modulation function which is expressed by a sum of the Heaviside functions of Eq. (2.26).

Appendix B: Theoretical Calculation of PA Cell Natural Frequency

To identify whether P_1, P_2 and P_5 in Fig. 2.5 (b) are resonance peaks, the natural frequencies of the PA cell are theoretically calculated. The possible natural frequency modes of a water-filled cylinder are the longitudinal mode, radial mode, bending mode and torsional mode. The corresponding natural frequency f_{jk} and eigen value λ_{jk} are expressed as the following formulas (Blevins, 1979). For the longitudinal mode:

$$f_{ik} = \frac{\lambda_{ik}}{2\pi L}\left(\frac{\kappa_e}{\rho_m}\right)^{1/2}, \tag{B.1}$$

$$\tau_{jk} = k\pi, \qquad \begin{matrix} k = 1,2,3 \cdots \\ j = 0 \end{matrix}$$

for the other modes

$$f_{jk} = \frac{\lambda_{jk}}{2\pi b}\left(\frac{\kappa_e}{\rho_m(1-\sigma_p^2)}\right)^{1/2}, \tag{B.2}$$

$$\lambda_{jk} = \frac{k^2\pi^2(1-\sigma_p^2)^{1/2}b}{\sqrt{2L^2}} \qquad \text{(bending mode)} \tag{B.3}$$

$$\lambda_{jk} = 1 \qquad \text{(radial mode)} \tag{B.4}$$

$$\lambda_{jk} = \frac{k(1-\sigma_p)^{1/2}}{\sqrt{2L}} \qquad \text{(torsional mode),} \tag{B.5}$$

where κ_e is a modulus of elasticity; σ_p, Poisson's ratio; ρ_m, mass density of the cell materials; L, cell length; j, the number of the circumferential wave in the mode shape; and k, the number of the longitudinal half-wave in

the mode shape. Water and cell material constants are listed in Table A.1. The longitudinal, radial and bending vibrations are accompanied by corresponding motions of the water, but the torsional vibration is not. Therefore the eigen values λ_{jk} of the former three modes should be calculated with the volume averaged material constants of the PZT, glass and water which are components of the entire cell body, while the eigen value of the torsional mode must be calculated with volume averages of the PZT and glass material constants.

Table A.1. Material constants of the PA cell components and water.

Symbol	Material constant	Value
κ_e	Modulus of elasticity	
	PZT	6.0×10^{11} dyn cm^{-2}
	glass	3.5×10^{11} dyn cm^{-2}
	water	2.6×10^{10} dyn cm^{-2}
ρ_p	Poisson's ratio	
	PZT	0.3
	glass	0.2
σ_m	Mass density	
	PZT	7.7 g cm^{-3}
	glass	2.2 g cm^{-3}
	water	1.0 g cm^{-3}

REFERENCES

Adams, M. T., and Kirkbright, G. F. (1977). *Analyst* (London) **102**, 678.

Addison, G. M. (1972). *J. Clin. Pathol.* 39, 326.

Albertsen, P. C., and Chang, T. S. K. (1983). *J. Clin. Immunoassay* **6**, 51.

Almond, H. (1953). *Anal. Chem.* **25**, 166.

Anderson, S. G., Bentzon, M. W., Houba, V., and Krag, P. (1970). *Bull. W.H.O.* **42**, 311.

Aoki, T., Yamada, C., and Katayama, M. (1970). *Jpn. J. Appl. Phys.* **9**, 1249.

Asakawa, H., and Mori, W. (1984). *J. Jpn. Soc. Clin. Pathol.* **32** (Suppl.), 347.

Atalar, A. (1980). *Appl. Opt.* **19**, 3204

Barret, J. J., and Berry, M. J. (1979). *Appl. Phys. Lett.* **34**, 144.

Baudin, S. (1930). *J. Chem. Phys.* **27**, 285.

Bell, A. G. (1880). *Am. J. Sci.* **20**, 305.

Bell, C. E., and Landt, J. A. (1967). *Appl. Phys. Lett.* **10**, 46.

Blevins, R. D. (1979). "Formulas for Natural Frequency and Mode Shape" Van Nostrand-Reinhold, New York, pp. 183-303.

Boccara, A. C., Fournier, D., and Badoz, J. (1980). *Appl. Phys. Lett.* **36**, 130.

Boyland, E. (1946). *Analyst* (London) **71**, 230.

Cahen, D., Malkin, S. and Lerner, E. I. (1978). *FEBS Lett.* **91**, 339.

Cargill, C. S. (1980). *Nature* **286**, 691.

Cambiaso, C. L., Leek, A. E., and De Steenwinkel, F. (1977). *J. Immunol. Methods.* **18**, 33.

Chen, P. Y., and Shirk, J. S. (1984). *Anal. Chem.* **56**, 80.

Cox, D. M. (1978). *Opt. Commun.* **24**, 336.

Cremers, D. A., and Radziemski, L. J. (1983). *Anal. Chem.* **55**, 1252.

Cremers, D. A., Radziemski, L. J., and Loree, T. R. (1984). *Appl. Spectrosc.* **38**, 721.

Fang, H. L., and Swofford, R. L. (1983). "Ultra Sensitive Laser Spectroscopy" Academic Press, New York. pp. 175-232.

Fournier, D., Buccara, A. C., Amer, N. M., and Gerlach, R. (1980). *Appl. Phys. Lett.* 37, 519.

Förster, T., and Kasper, K. (1955). *Z. Electrochem.* 59, 977.

Gold, P., and Freedman, S. O. (1965). *J. Exp. Med.* 121, 439.

Harshbarger, W. R., and Robin, M. B. (1973). *Acc. Chem. Res.* 6, 329.

Hirai, H. (1977). *Cancer Res.* 37, 2267.

Hirakawa, H. (Ed.) (1984). "Chronological Science Table (Ed. Tokyo Astronomical Observatory)", Maruzen, Tokyo, p. 525.

Ishii, M.(1978). *Scand. J. Immunol.* 8 (Suppl. 8), 611.

Jackson, W. B., and Amer, N. M. (1980). *J. Appl. Phys.* 51, 3343.

Jackson, W. B., Amer, N. M., Boccara, A. C., and Fournier, D. (1981). *Appl. Opt.* 20, 1333.

Jacob, M., (1957). "Heat Transfer", John Wiley, New York.

Kagawa, K., and Yokoi, S. (1982). *Spectrochem. Acta B* 37, 789.

Kaya, K., Chatelain, C. L., and Robin, M. B. (1975). *J. Am. Chem. Soc.* 97, 2153.

Kaya, K., Harshbarger. W. R., and Robin, M. B. (1974). *J. Chem. Phys.* 59, 3713.

Kirkbright, G. F., Miller, M., and Spillane, E. M. (1984). *Anal. Chem.* 56, 2043.

Kitamori, T., Fujii, M., Sawada, T., and Gohshi, Y. (1983). *J. Phys.* (Paris) 44, C6-209

Kitamori, T., Fujii, M., Sawada, T., and Gohshi, Y. (1984). *J. Appl. Phys.* 55, 4005.

Kitamori, T., Fujii, M., Sawada, T., and Gohshi, Y. (1985a). *J. Appl. Phys.* 58, 268.

Kitamori, T., Fujii, M., Sawada, T., and Gohshi, Y. (1985b). *J. Appl. Phys.* 58, 1456.

Kitamori, T., Fujii, M., Sawada, T., and Gohshi, Y. (1985c). *Jpn. J. Appl. Phys.* 24, (Suppl. 24-1), 210.

Kitamori, T., Fujii, M., Sawada, T., and Gohshi, Y. (1985d). *J. Spectrosc. Soc. Jpn.* **34**, 359.

Kitamori, T., Suzuki, K., Sawada, T., and Gohshi, Y. (1986a). *Anal. Chem.* **58**, 2275.

Kitamori, T., Suzuki, K., Sawada, T., and Gohshi, Y. (1986b). *J. Spectrosc. Soc. Jpn.* **35**, 478.

Kitamori, T., Suzuki, K., Sawada, T., and Gohshi, Y. (1986c). *The Hitachi, Sci. Inst. News* **29**, 10.

Kitamori, T., Suzuki, K., Sawada, T., and Gohshi, Y. (1987). *Anal. Chem.* **59**, 2519.

Kitamori, T., Suzuki, K., Yokose, K., Sawada, T., Harada, A., and Gohshi, Y. (1988a). "Optical Sciences, Vol. 58", Springer-Verlag, Heidelberg, p. 150.

Kitamori, T., Suzuki, K., Sawada, T., and Gohshi, Y. (1988b). "Optical Sciences, Vol. 58", Springer-Verlag, Heidelberg, p. 561.

Kitamori, T., Yokose, K., Suzuki, K., Sawada, T., and Gohshi, Y. (1988c). *Jpn. J. Appl. Phys.* **27**, L983

Kitamori, T., Suzuki, K., Sawada, T., and Gohshi, Y. (1988d). *J. Chem. Phys.*, submitted.

Kitamori, T., and Sawada, T. (1982). *J. Appl. Phys.* **21**, L285.

Kitamori, T., and Sawada, T. (1988). "Physical Acoustics, Vol. 18", Academic, New York, pp. 347-401.

Kitamura, M., Ibe, E., Uchida, S., Honda, T., Rormeo, T., and Cowan, R. L., (1985). *Nucl. Sci. Eng.* **89**, 61.

Kodama, T. (1979). *Cancer* **44**, 661.

Kohanzadeh, Y., Winnerley, J. R., and Carrol, M. M. (1975). *J. Acoust. Soc. Am.* **57**, 67.

Kreuzer, L. B. (1971). *J. Appl. Phys.* **42**, 2934.

Kreuzer, L. B., Kenyon, N. D., and Patel, C. K. N. (1972). *Science* **177**, 347.

Lahmann, W., Ludewig, H., Welling, H. (1977). *Anal. Chem.* **49**, 549.

Lamarsh, J. R. (1974). "Introduction to Nuclear Reactor Theory", Addison-Wesley, Boston, Chapter 1.

Landau, L. D., and Lifshitz, E. M. (1960). "Electrodynamics of Continuous Media (Sykes, J. B. and Bell, J. S. Translators)", Pergamon, New York, p. 303.

Liu, G. (1982). *Appl. Opt.* **21**, 955.

Low, M. J. D. and Parodi, G. A. (1978). *Spectrosc. Lett.* **11**, 581.

Luft, K. F. (1943). *Z. Tech. Phys.* **24**, 97.

Mandelis, A., Teng, Y. C., and Royce, B. S. H. (1979). *J. Appl. Rhys.* **50**, 7138.

Marinero, E. E., and Stuke, M. (1979). *Opt. Commun.* **30**, 349.

Matsuda, H., Fujishima, A., and Honda, K. (1980). *Bull. Chem. Soc. Jpn.* **53**, 1542.

McDonald, F. A., and Wetsel Jr., G. C. (1978). *J. Appl. Phys.* **49**, 2313.

Merkle, L. D., and Powell, R. C. (1977). *Chem. Phys. Lett.* **45**, 177.

Mittleman, M. H. (1982). "Introduction to the Theory of Laser-Atom Interactions", Plenum Press, New York, p. 19.

Monchalin, J. P., Bertland, L., and Rousset, G. (1984). *J. Appl. Phys.* **56**, 190.

Morse, P. M., and Ingard, K. U. (1968). "Theoretical Acoustics", McGraw Hill, New York, p. 319.

Motojima, K. (1985). *Private Communication.*

Murphy, J. C., and Aamodt, L. C. (1980). *J. Appl. Phys.* **51**, 4580.

Needleman, M. (1966). *Anal. Chem.* **38**, 915.

Nishi, S., and Hirai, H. (1973). *Gann Monogr. Cancer Res.* **14**, 79.

Nomura, N., Oda, S., and Sawada, T. (1982). *J. Photoacoust.* **1**, 128.

Oda, S., and Sawada, T. (1981). *Anal. Chem.* **53**, 471.

Oda, S., Sawada, T., and Kamada, H. (1978). *Anal. Chem.* **50**, 865.

Oda, S., Sawada, T., Moriguchi, T., and Kamada, H. (1980). *Anal. Chem.* **52**, 650.

Onoe, M., Tierfpen H. F., and Meitzler, A. H. (1963). *J. Acoust. Soc. Am.* **35**, 36.

Opsal, J., Rosencwaig, A., and Willenborg, D. L. (1983). *Appl. Opt.* **22**, 3169.

Pao, Y. H. (Ed) (1977). "Optacoustic Spectroscopy and Detection", Academic Press, New York.

Parker, C. A., and Hachard, C. G. (1964). *Trans. Faraday Soc.* **59**, 284.

Parker, J. G. and Ritke, D. N. (1973). *J. Chem. Phys.* **59**, 3713.

Patel, C. K. N. (1978). *Science* **202**, 157.

Patel, C. K. N., and Tam, A. C. (1979). *Nature* **280**, 302.

Patel, C. K. N., and Tam, A. C. (1981). *Rev. Mod. Phys.* **53**, 517.

Quimby, R. S., and Yen, W. M. (1980). *J. Appl. Phys.* **51**, 4895.

Ranz, W. E. (1952). *Chem. Engng. Progr.* **48**, 141.

Röntgen, W. C. (1881). *Phil. Mag.* **11**, 308.

Rosencwaig, A. (1973a). *Opt. Commun.* **7**, 305.

Rosencwaig, A. (1973b). *Science* **181**, 657.

Rosencwaig, A. (1975a). *Phys. Today* **28**, 23.

Rosencwaig, A. (1975b). *Anal. Chem.* **47**, 592A.

Rosencwaig, A. and Pines, E. (1977). *Biochim. Biophys. Acta* **493**, 10.

Rosencwaig, A. (1980a). "Photoacoustics and Photoacoustic Spectroscopy", (Chemical Analysis), Vol. 57, John Wiley, New York.

Rosencwaig, A. (1980b). *J. Appl. Phys.* **51**, 2210.

Rosencwaig, A., and Gersho, A. (1976). *J. Appl. Phys.* **47**, 64.

Rosencwaig, A., and Hall, S. S. (1975). *Anal. Chem.* **47**, 548.

Sawada, T. (Ed.) (1982). "Photoacoustic Spectroscopy and Its Applications (in Japanese)", Gakkai Shuppan Center, Tokyo.

Sawada, T. and Oda, S. (1981). *Anal. Chem.* **53**, 539.

Sawada, T., Oda, S., and Kamada, H. (1978). *Proc. Jpn. Acad.* **54B**, 184.

Sawada, T., Oda, S., Shimizu, H., and Kamada, H. (1979). *Anal. Chem.* **51**, 688.

Sawada, T., Shimizu, H. and Oda, S. (1981). *Jpn. J. Appl. Phys.* **20**, L5.

Singer, J. M. and Plotz, C. M. (1956). *Am. J. Med.* **21**, 888.

Sugitani, Y., Uejima, A., and Kato, K. (1982). *J. Photoacoust.* **1**, 217.

Swofford, R. L., and Morrell, J. A. (1978). *J. Appl. Phys.* **49**, 3667.

Tam, A. C. (1986). *Rev. Mod. Phys.* **58**, 381.

Twarowski, A. J., and Kliger, D. S. (1977). *Chem. Phys.* **20**, 253.

Tyndall, J. (1881). *Proc. R. Soc. Lond.* **31**, 307.

Uejima, A., Sugitani, Y., and Nagashima, K. (1985). *Anal. Sci.* **1**, 5.

Van de Hulst, H. C. (1957). "Light Scattering by Small Particles", John Wiley, New York, p. 110 and p. 267.

Viengerov, M. L. (1938). *Dokl. Akad. Nauk. SSSR* **19**, 687.

Voigtman, E., Jorgensen, A., and Winfordner, J. (1981). *Anal. Chem.* **53**, 1442.

Voigtman, E., and Winfordner, J. (1982). *Anal. Chem.* **54**, 1834.

Wasa, K., Tsubouchi, K., and Mikoshiba, N. (1980). *Jpn. J. Appl. Phys.* **19**, L475.

Wong, Y. H., Thomas, R. L. and Hawkins, G. F. (1978). *Appl. Phys. Lett.* **32**, 538.

Yamada, S., Hino, A., and Ogawa, J. (1984). *Anal. Chim. Acta.* **156**, 273.

LIST OF PUBLICATIONS

1) Kitamori, T., and Sawada, T.
Theoretical Analysis of Frequency Characteristics of Photoacoustic Signals in Liquids, *Jpn. J. Appl. Phys.* **21**, L285 (1982).

2) Kitamori, T., Fujii, M., Sawada, T., and Gohshi, Y.
Theoretical Aspects of Photoacoustic Signal Detection with a Direct Coupling Cell for Liquids, *J. Phys.* (Paris) **44**, C6-209 (1983).

3) Kitamori, T., Fujii, M., Sawada, T., and Gohshi, Y.
Frequency Characteristics of Photoacoustic Signals Generated in Liquids, *J. Appl. Phys.* **55**, 4005 (1984).

4) Kitamori, T., Fujii, M., Sawada, T., and Gohshi, Y.
Optimal Geometrical Conditions of Photoacoustic Signal Detection with a Cylindrical Direct Coupling Cell for Liquids, *J. Appl. Phys.* **58**, 268 (1985).

5) Kitamori, T., Fujii, M., Sawada, T., and Gohshi, Y.
Phase Shift of Photoacoustic Signals from Microparticles in Liquids, *J. Appl. Phys.* **58**, 1456 (1985).

6) Kitamori, T., Fujii, M., Sawada, T., and Gohshi, Y.
Linear Response Theory in Photoacoustic Spectroscopy and Characterization of Turbid Particles, *Jpn. J. Appl. Phys.* **24**, Suppl.

1, 210 (1985).

7) Kitamori, T., Fujii, M., Sawada, T., and Gohshi, Y.
An Ultrasensitive Photoacoustic Spectrophotometer for Liquids, *J. Spectrosc. Soc. Jpn.* **34**, 359 (1985).

8) Kitamori, T., Suzuki, K., Sawada, T., Gohshi, Y., and Motojima, K.
Determination of Sub-Part-Per-Trillion Amounts of Cobalt by Extraction and Photoacoustic Spectroscopy, *Anal. Chem.* **58**, 2275 (1986).

9) Kitamori, T., Suzuki, K., Sawada, T., and Gohshi, Y.
Size Measurement of Microparticles in Liquids Using Photoacoustic Spectroscopy, *J. Spectrosc. Soc. Jpn.* **35**, 478 (1986).

10) Kitamori, T., Suzuki, K., Sawada, T., and Gohshi, Y.
Photoacoustic Immunoassay Using Sensitivity Size Dependency in Determination of Turbid Solutions, *Anal. Chem.* **59**, 2519 (1987).

11) Kitamori, T., Suzuki, K., Sawada, T., and Gohshi, Y.
Basic Study of Photoacoustic Immunoassay and Determination of Trace Rheumatoid Factor, "Optical Sciences, Vol. 58". Springer Verlag, Heidelberg, 561. (1988).

12) Kitamori, T., Suzuki, K., Yokose, K., Sawada, T., Harada, A., and Gohshi, Y.
Detection of Ultrafine Particles in Liquids Using Breakdown Acoustic Effect, "Optical Sciences Vol. 58", Springer Verlag, Heidelberg, 150 (1988).

13) Kitamori, T., Yokose, K., Suzuki, K., Sawada, T., and Gohshi, Y. Laser Breakdown Acoustic Effect of Ultrafine Particle in Liquids and Its Application to Particle Counting, *Jpn. J. Appl. Phys.* 27, L983 (1988).

14) Kitamori, T., Yokose, K., Suzuki, K., Sawada, T., and Gohshi, Y. Detection and Counting of Ultrafine Particles in Ultrapure Water by Laser Breakdown Acoustic Spectroscopy, *Jpn. J. Appl. Phys.*, (1988) submitted.

15) Kitamori, T., Suzuki, K., Sawada, T., and Gohshi, Y. Theoretical Approach to Characterization of Nonradiative Relaxation Processes in Liquids with Photoacoustic Spectroscopy, *J. Chem. Phys.*, (1988) submitted.

Review Articles

16) Sawada, T., and Kitamori, T. Analytical Applications of Photoacoustic Spectroscopy to Condensed Phase, "Physical Acoustics, Vol. 18", Academic Press, New York, pp. 347-401.(1988).

17) Sawada, T., and Kitamori, T. Detection of Ultrafine Particles in Ultrapure Water by Laser-Induced Breakdown Acoustic Effect (Invited paper), *IEEE Transaction*, (1989) in press.

18) Kitamori, T.

Revolution and Future of Ultratrace Analysis - Progress of Ultrasensitive Photoacoustic Spectrometry - (in Japanese), *Chemistry and Chemical Industry (Kagaku To Kogyo)* **42**, (1989) in press.

19) Kitamori, T., Suzuki, K., Sawada, T., and Gohshi, Y.

Ultrasensitive Colorimetry Using Photoacoustic Spectroscopy (in Japanese), *The Hitachi, Sci. Inst. News* **29**, 10 (1986).

20) Sawada, T., and Kitamori, T.

Analysis of Fine and Ultrafine Particles in Liquids by Photoacoustic Spectroscopy (in Japanese), *Surface (Hyoumen)* **26**, 738 (1988).

21) Sawada, T., and Kitamori, T.

Photoacoustic Immunoassay - A New Method for Ultrasensitive Immunoassay - (in Japanese), *Bio Medica* **4**, 41 (1989).

22) Sawada, T., and Kitamori, T.

Immunological Sensor Using Photoacoustic Effect (in Japanese), *Sensor Technology* **9**, 75 (1989).

23) Kitamori, T., and Sawada, T.

Immunoassay Using Photoacoustic Spectrometry (in Japanese), *Medical Technology* **17**, (1989) in press.

24) Kitamori, T., and Sawada, T.

Photoacoustic Immunoassay (in Japanese), *The Jpn. J. of Clin. Med. (Nihon Rinsho)* **47**, (1989) in press.

Patents

25) Kitamori, T., Fujii, M., and Sawada, T.
Photoacoustic Analyzer, U.S. Patent 4,557,137 (1985).

26) Kitamori, T., Suzuki, T., and Sawada, T.
Apparatus and Method for Analyzing Particles in a Medium, U.S. Patent 4,722,602 (1988)

27) Kitamori, T., Uchida, S., Kawasaki, S., and Kondo, M.
Method for Analyzing Impurities in Liquid and Apparatus Therefor, U.S. Patent 4,738,536 (1988)